# NORM FASTENERS
# AR-GE MERKEZİ YAYINLARI

*R&D CENTER PUBLICATIONS*


## 2025

VOLUME 11

NORM
FASTENERS

**NORM FASTENERS**

AR-GE MERKEZİ YAYINLARI

*R&D CENTER PUBLICATIONS*

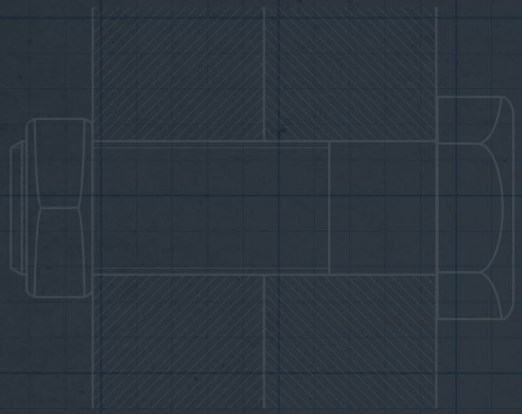



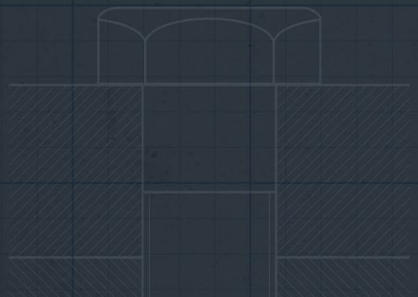

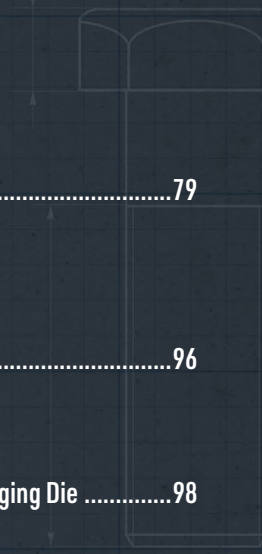

# ÖN SÖZ

## Umut İnce
**Norm Fasteners Ar-Ge Direktörü**

Norm Holding olarak sürdürülebilir gelecek vizyonumuz doğrultusunda; küresel teknolojik eğilimleri yakından takip ederek, dijitalleşme, ileri malzeme teknolojileri ve yenilikçi ürün geliştirme alanlarında Ar-Ge ve inovasyon yatırımlarımıza stratejik bir bakış açısıyla yön vermekteyiz. Bu yaklaşımımızla, sektörümüzdeki dönüşüme öncülük etmeyi ve geleceğin rekabetçi dinamiklerine yön veren bir yapı oluşturmayı hedefliyoruz. Değerli iş ortaklarımızla birlikte, uzun vadeli ve sürdürülebilir değer yaratma misyonumuzu kararlılıkla sürdürmekteyiz.

Güçlü akademik altyapıya sahip uzman Ar-Ge kadromuz ve stratejik iş birliklerimiz sayesinde; müşteri beklentilerini aşan, yüksek katma değerli ve yenilikçi çözümler geliştirmenin yanı sıra, dijital mühendislik, veri odaklı ürün geliştirme ve sürdürülebilir tasarım alanlarında ulusal ve uluslararası ölçekte öncü çalışmalar gerçekleştirmekteyiz. Tüm faaliyetlerimizde; teknik mükemmeliyet, sistematik yaklaşım ve sürekli gelişim anlayışıyla hareket ederek, teknolojik ilerlemeye katkı sağlamayı ve sektörümüzde kalıcı değer üretmeyi kurumsal bir sorumluluk olarak görüyoruz.

2025 yılı içerisinde hayata geçirdiğimiz çalışmaların çıktılarını sizlerle paylaşmaktan büyük bir memnuniyet ve gurur duyuyoruz. Bu kitapçık aracılığıyla, ortak hedeflerimiz doğrultusunda yürüttüğümüz Ar-Ge faaliyetlerinin somut kazanımlarını siz değerli iş ortaklarımızın bilgisine sunarken; inovasyon, sürdürülebilirlik ve teknoloji odağında geleceğe birlikte yön verme kararlılığımızı bir kez daha vurguluyoruz.



# FOREWORD

## Umut İnce
**Norm Fasteners R&D Director**

At Norm Holding, in line with our vision for a sustainable future, we closely monitor global technological trends and strategically direct our R&D and innovation investments towards digitalization, advanced material technologies, and innovative product development. Through this approach, we aim to lead the transformation of our industry and shape the competitive dynamics of the future. Together with our valued business partners, we remain firmly committed to our mission of creating long-term and sustainable value.

Leveraging our expert R&D team with strong academic foundations and our strategic collaborations, we not only develop high value-added and innovative solutions that exceed customer expectations, but also carry out pioneering work at both national and international levels in areas such as digital engineering, data-driven product development, and sustainable design. Across all our activities, we act with a focus on technical excellence, a systematic approach, and continuous improvement, and we consider contributing to technological advancement and delivering lasting value to our industry as a fundamental corporate responsibility.

We are proud and pleased to share the outcomes of our work carried out in 2025. Through this booklet, we present the tangible achievements of our R&D activities aligned with our common objectives, while reaffirming our commitment to shaping the future together with our esteemed business partners, with a strong focus on innovation, sustainability, and technology.

# EFFECT OF BORIDING ON WEAR AND FATIGUE LIFE OF WC-CO DIE INSERTS IN COLD FORMING

*Kübra ÖZTÜRK GÜLER*
*Bahadır UYULGAN*
*Burak HIZLI*
*Umut İNCE*

Engineering Failure Analysis

# EFFECT OF BORIDING ON WEAR AND FATIGUE LIFE OF WC-CO DIE INSERTS IN COLD FORMING

**Kübra ÖZTÜRK GÜLER[1,2,3,a*], Bahadır UYULGAN[1,b], Burak HIZLI[3],c and Umut İNCE[3,d]**

[1]Department of Metallurgical and Materials Engineering, Dokuz Eylul University, İzmir, Turkey
[2]The Graduate School of Natural and Applied Sciences, Department of Metallurgical and Materials Engineering, Dokuz Eylul 35390 Izmir, Turkey
[3]R&D Center, Norm İzmir Cıvata San. ve Tic. A.Ş., AOSB, İzmir, Turkey
[a]kubra.ozturk@normfasteners.com, [b]bahadir.uyulgan@deu.edu.tr,
[c]burak.hizli@normfasteners.com, [d]umut.ince@normfasteners.com

Cold forging is a key manufacturing process in fastener production, utilizing multi-stage die systems to plastically deform materials under high compressive stresses. In cold forming operations such as extrusion, reduction, and head forming, WC-Co materials are widely employed in die applications, selected based on the specific requirements of the process. These die materials used in cold forming must exhibit high wear resistance and fatigue strength due to the substantial forming forces that generate significant stresses within the dies. Boriding, a surface treatment method, is applied to enhance these mechanical properties. This study investigates the effects of pack-boriding treatment on the fatigue life and wear properties of WC-Co material containing 19% Co, which are used as die inserts in cold forging die systems. Three sets of samples were pack-borided using EKABOR-2 boron powder at 1000°C, 950°C, and 900°C for 4 hours under each temperature condition to accomplish this process. Following the pack-boriding process, pin-on-plate wear tests were conducted under both non-lubricated and lubricated conditions to evaluate the wear performance of the samples. Three-point bending fatigue tests were performed to assess the fatigue behavior of the borided samples. After the fatigue test, Goodman-Haigh diagrams were obtained from the experimental results to be utilized in predictive die-life calculations. X-ray diffraction (XRD) analysis confirmed the formation of CoB, $Co_2B$, $WB_2$ and $W_2CoB_2$ phases in the borided layer. Results indicate that increasing boriding temperature significantly improves wear resistance and surface hardness, with the highest microhardness (4104 $HV_{0.1}$) and the lowest wear track width (183 µm non-lubricated, 70.76 µm lubricated) measured at 1000°C. However, the thick and brittle boride layer induced stress concentrations, negatively affecting the material's fatigue performance. According to the Goodman-Haigh diagrams, the highest fatigue life after boriding was measured as 5,000,000 cycles at 950°C, while the lowest was 135,356 cycles at 450 MPa after boriding at 1000°C. Although the increased hardness of the $WB_2$ phase at 1000°C enhanced wear resistance, the formation of a brittle boride layer led to stress concentrations, facilitating crack initiation and reducing die life. This indicates that while higher boriding temperatures improve surface hardness, they also increase brittleness, negatively impacting the material's fatigue performance.

**Keyword:** Pack Boriding, Fatigue life, Wear, WC-Co, Cold forming

## 1. Introduction

Cemented carbide materials belong to a class of composite materials produced through powder metallurgy, consisting of hard metal, refractory, and binder metal phases. Due to their exceptional hardness, wear, and corrosion resistance, these materials are widely utilized in the metal forming industry, particularly in cold forming applications [1]. WC-Co-based materials are metal-matrix ceramic composites composed of a WC hard phase, which provides hardness and wear resistance, and a Co binder phase, which enhances toughness and strength [2]. These materials are classified based on their grain sizes according to the ISO 4499-2:2020 standard, ensuring that they acquire mechanical properties suitable for specific applications [3].

Cold forming is a manufacturing process in which metals are plastically deformed below their recrystallization temperature. The dies used in this process are critical engineering components that define the geometric precision of the final product. These dies typically consist of a fixed die and a movable punch, where the workpiece is subjected to high compressive forces to achieve its final shape. During cold forming, the primary failure mechanisms in dies include (i) plastic deformation, (ii) wear, and (iii) fatigue, all of which are caused by high mechanical loads and intense friction conditions [4, 5]. Excessive wear and fatigue damage significantly reduce die life, decreasing production efficiency and increasing process costs. The selection of suitable WC-Co materials for various cold forming processes plays a critical role in enhancing die performance and extending service life. In high-friction processes such as extrusion and reduction processes, fine-grained WC particles or low Co binder content materials are preferred to enhance wear resistance[5, 6]. Conversely, in process that require high compressive strength, such as upsetting process, larger WC grain sizes and higher Co binder content (≥15%) are used to increase toughness and improve resistance to fatigue and fracture [6,7,8]. However, repeated exposure to high friction and loading accelerates microcrack formation, leading to early material failure. Enhancing the surface hardness, wear resistance, and mechanical stability of WC-Co cemented carbides requires the implementation of advanced surface engineering techniques. In particular, thermochemical diffusion treatments, especially boriding, have proven effective in improving the tribological performance of WC-Co materials. The formation of hard boride phases through boriding can significantly improve wear mechanisms, extending service life under extreme forming conditions. Boriding is a thermochemical surface hardening process that enhances mechanical properties by inducing the diffusion of boron atoms into the material surface at elevated temperatures [9, 10]. This process is performed at controlled temperatures ranging between 840°C and 1050°C for a specified duration, typically between one and ten hours [9,11]. The small atomic radius and high mobility of boron enable its diffusion into the material surface, where it reacts with substrate atoms to form a hard boride layer [10]. Furthermore, this process creates a diffusion zone with distinct microstructural characteristics, improving wear resistance, surface hardness, and fatigue strength, ultimately extending the service life of the material in demanding applications. The effects of boriding on WC-Co-based materials have been extensively investigated in the literature, with studies focusing on different material compositions, processing parameters, and mechanical performance outcomes. Regarding boriding methods and process parameters, Guobiao et al. examined YG11 (WC–11 wt.% Co) cemented carbides subjected to solid-state boriding at 950°C for 5 hours, analyzing the influence of boriding agent components. Their findings indicated that $KBF_4$ and $B_4C$ react at high temperatures, facilitating boron diffusion into the Co phase, leading to a 30% increase in wear resistance [11]. Similarly, Köksal et al. applied boriding to ISO P25 WC-Co cutting inserts using a molten salt bath at 900, 1000, and 1100°C for 1, 2, and 4 hours, reporting the formation of $W_2B_5$, CoB, $W_2CoB_2$, and WCoB phases with borided layer thicknesses ranging from 7 to 15 µm. In terms of microstructural and mechanical property modifications [12], Dearnley et al. deposited $CrB_2$, $Mo_2B_5$, and WB coatings on WC-Co cutting tools via unbalanced magnetron sputtering and found that $CrB_2$ exhibited the highest hardness (~2764 HV), while WB coatings provided superior adhesion and structural integrity [13]. Concerning hardness and wear resistance improvements, Usta et al. investigated the borided of pure tungsten, reporting a compact boride layer formation with a surface hardness of 2500 HV and a substrate hardness of 445 HV [14]. Herrera et al. studied WC-Co-based hardmetal inserts borided at 900°C for 4 hours, noting an increase in hardness from 1492 HV to 2000 HV and a boride layer thickness of approximately 28 µm [15]. Regarding potential drawbacks of boriding, Aydogmus observed that while boriding improved wear resistance in WC-Co drill bits, it reduced impact strength [16]. Oruc reported that ISO P25 WC-Co cutting tools borided at 1000°C for 2 hours exhibited a maximum microhardness of 3600 $HV_{0.1}$ at a depth of 5-8 µm, whereas at 1100°C, WC particles degraded, leading to structural instability [17]. Coureaux et al. investigated M12, M23, and H14 cemented carbides borided at 1000°C for 4 hours and found that cobalt content and grain size significantly influenced the boride layer thickness and microstructure [18].

Literature reviews indicate that boriding has primarily been applied to WC-Co materials in cutting tools [12, 13, 14, 18 ] and tool inserts [11, 17]. However, despite its widespread use in steels and other alloyed materials, the application of boriding in cold forming dies remains underexplored and limited in industrial practice. Die life has always been a crucial research area in the cold forming industry, as these tools are subjected to extreme operating conditions and exhibit complex damage mechanisms. Considering the severe operating conditions of cold forming dies and the complex failure mechanisms associated with cemented carbides, developing innovative strategies to enhance die longevity is of

paramount importance. In this context, this study aims to investigate the effects of boriding as a surface engineering technique on WC-Co cemented carbide die inserts used in cold forming dies. Specifically, it evaluates the feasibility of boriding in WC-Co-based cold forming dies and examines its influence on mechanical and tribological properties. This study systematically investigates the influence of pack-boriding on the mechanical and tribological performance of WC-Co cemented carbides containing 19% Co, commonly utilized in cold forging dies. Specimens were subjected to boriding at 900°C, 950°C, and 1000°C for 4 hours to evaluate the effects of temperature on wear resistance, surface hardness, and fatigue behavior. The experimental evaluation involved pin-on-plate wear tests under both lubricated and non-lubricated conditions to assess tribological behavior, as well as three-point bending fatigue tests to examine the material's resistance to cyclic loading. Additionally, scanning electron microscopy (SEM) was employed to analyze fracture surfaces, revealing that higher boriding temperatures led to stress concentrations and crack initiation. X-ray diffraction (XRD) confirmed the formation of boride phases, which contributed to increased hardness but also influenced mechanical stability.

## 2. Experimental Procedure

### *2.1 Preperation of Samples*

The GB40 material with 19% Co content was comparatively examined in this study in terms of wear resistance and fatigue life. The reference materials were provided by Boehlerit GmbH & Co.KG. The chemical composition and mechanical properties of the GB40 sample are presented in Table 1 [19]. For the experimental studies, the samples were prepared in accordance with the ISO 3337:2009 TYPE B standard, with dimensions in the 20x6.5x5.25 mm [20]. All test samples were sintered using WC powder and a Co binder with the aid of special dies, and subsequently subjected to HIP (Hot Isostatic Pressing) to prepare the test specimens without any additional machining.

**Table 1.** Chemical and Mechanical Properties of GB40 Material [19].

| Grade | Chemical Composition [wt. %] | | | Density [g/cm3] | Hardness HV 30 [MPa] | Compressive Strength [MPa] | Transverse Rupture Strength [MPa] | Fracture Toughness [$MNm^{-3/2}$] | Elastic Modulus [GPa] | Thermal Expansion Coefficient [$10^{-6}$ / K] |
|---|---|---|---|---|---|---|---|---|---|---|
| | WC | Co | Other | | | | | | | |
| **GB40** | Balanced | 19 | <0.2 | 13.60 | 950 | 4000 | 2800 | ≥ 24 | 530 | 6 |

The surface roughness of the samples was improved prior to the boriding process to minimize frictional effects that can reduce die life in cold forming processes. After receiving the samples, the surface preparation procedures were initiated to achieve conditions similar to those of forming dies. The surfaces of the test specimens were ground and polished using a Metkon Forcipol 102 grinding and polishing machine in combination with a Metkon Forcimat 102 automatic head. For the grinding process, Akasel Piatto 220+ diamond grinding discs were employed under a load of 40 N, at a rotational speed of 500 rpm, for 5 minutes. This step was followed by polishing with Akasel Allegran 3 fine diamond polishing discs under the same conditions for 8 minutes. Water was used exclusively during grinding, while polishing was performed with a 6-micron diamond suspension. Following the boriding process, the samples were subjected to polishing treatments to simulate the typical operational conditions encountered by the dies. Subsequently, surface roughness measurements were performed for each boriding temperature condition using a Mitutoyo SJ 210 portable surface roughness tester. The surface roughness values were determined as the average of five measurements, expressed in terms of the Ra parameter indicating the surface roughness levels of the samples.

### *2.2 Boriding Process*

The pack boriding process was carried out at temperatures of 900°C, 950°C, and 1000°C for a duration of 4 hours using alumina crucibles. Ekabor 2® was utilized as the boron source, and its chemical composition is presented in Table 2.



Before placing the samples into the alumina crucibles, a layer of Ekabor 2® powder with a height of 20 mm was added at the bottom of the crucibles. The samples were then positioned inside the crucibles, after which Ekabor 2® powder was added again, completely covering the samples on all sides. Finally, as shown in Figure 1(a), a layer of "Ekrit (Deoxidizer)" powder was applied to the upper surfaces of the samples, and the alumina ceramic crucibles were sealed with their lids. The Ekrit powder used consists of pure iron and oxide-absorbing compounds. During the boriding process, this powder prevents the formation of oxides, ensuring a cleaner and more homogeneous boron coating on the material surface. Additionally, it limits the contact of oxygen with the material surface, thereby enhancing the efficiency of the boriding process and preventing the accumulation of undesirable oxides on the surface. The samples were subsequently placed in a PROTHERM heat treatment furnace, as shown in Figure 1(b), located in the Heat Treatment Laboratory of Dokuz Eylül University's Metallurgical and Materials Engineering Department. The boriding process was carried out at different temperatures for 4 hours in the furnace, where the samples were placed as part of the experimental procedure.

**Table 2.** Chemical composition of Boron source powder.

| Bor Powder Source | Chemical Composition |
|---|---|
| Ekabor 2® | $B_4C$-SiC-$KBF_4$ |

(a) (b)

**Fig.1.** (a) The position of the samples in the alumina-ceramic crucible after the addition of Ekrit powder, (b) The positioning of the samples inside the furnace.

### *2.3 Wear Tests*

The wear behavior of GB40 materials after boriding was investigated using the test setup shown in Figure 2. The wear tests were conducted at the Tribology Laboratory of Dokuz Eylül University using a pin-on-plate wear testing apparatus. The tests were performed according to ASTM G99-17, "Test Method for Wear Testing with a Pin-on-Disk Apparatus" standard [21]. The tests were carried out under a 10 N load with a 10 mm stroke. WC-Co balls were used as the abra-

sive counter material to simulate the wear interaction between the test samples and the opposing material. In order to simulate reel production conditions, the tests were conducted in both lubricated and non-lubricated environments. In the lubricated environment, industrial boron oil, which is typically used during production, was applied as the lubricant.

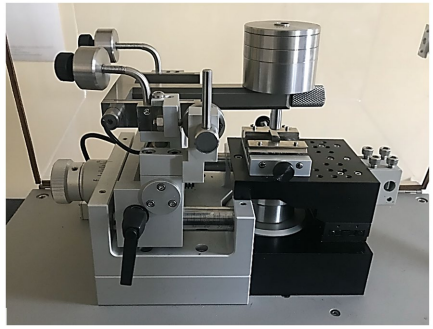

**Fig.2.** Wear Test Setup.

### *2.4 Fatigue Tests*

Fatigue life tests were carried out on prismatic test samples using a three-point bending test apparatus adapted to Zwick Roell Amsler 250 FP 5100 high-frequency fatigue testing machine Test samples and fatigue testing stage are illustrated in Fig. 3a and Fig. 3b, respectively. Stress amplitudes in fatigue tests were determined as 400 MPa, and 450MPa in order to observe the fatigue behavior in a wide range of loading conditions. Stress ratios (R) were determined using minimum stress $\sigma_{min}$(MPa) and maximum stress $\sigma_{max}$ (MPa) values in a cycle as given in Eq. 1. Mean stresses σm (MPa) and stress amplitudes σa (MPa) were sequentially calculated by the formulas in Eq. 2 and Eq. 3 as given below.

$$R = \frac{\sigma_{min}}{\sigma_{max}} \quad (1)$$

$$\sigma_m = \frac{\sigma_{max} + \sigma_{min}}{2} \quad (2)$$

$$\sigma_a = \frac{\sigma_{max} - \sigma_{min}}{2} \quad (3)$$

Maximum and minimum loads in fatigue tests were calculated for corresponding maximum and minimum stress values based on stress ratios of R=0.1 and R=0.2 by using Eq. 4 which is given in ISO 3327:2009 as;

$$R_{bm} = \frac{3kFl}{2bh^2} \quad (4)$$

where $R_{bm}$ is transverse rupture strength in MPa, $F$ is the force applied to the test piece in N, $k$ is the correction factor to compensate for the chamfer, $l$ is the distance between supports (mm), b is the width of test piece perpendicular to its height (mm), and h is the height of test piece parallel to the direction of application of the test force (mm), respectively. $k$ value was taken as 1, as described in the standard for test samples having chamfer of 0,15 to 0,2 mm [20].



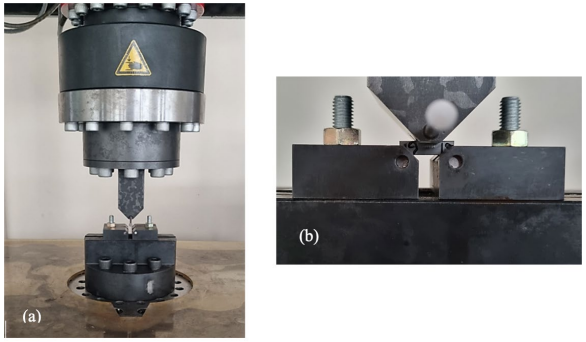


**Fig.3. (a)** Dimensions of prismatic samples used in the testing stage and **(b)** testing fixtures used in fatigue tests and sample positioning.

After the boriding heat treatment, the samples were subjected to three-point bending fatigue tests. The static and dynamic forces, along with the maximum, minimum, and average stress values, are presented in Table 3. A fatigue limit of 5,000,000 cycles was accepted for the fatigue tests. The average fatigue performance for each set was determined by taking the mean of the three consistent test results. Based on the experimental data, Goodman-Haigh diagrams were generated to predict the die life for each boriding condition.

**Table 3.** Fatigue test parameters and corresponding static and dynamic loads.

| Stress Ratio [R] | Stress Amplitude, σa [MPa] | Min. Stress, $\sigma_{min}$ [MPa] | Max. Stress, $\sigma_{max}$ [MPa] | Mean Stress, σm [MPa] | Static Load [kN] | Dynamic Load [kN] |
|---|---|---|---|---|---|---|
| 0,1<br>0.1 | 400<br>450 | 88,8<br>99,9 | 888,8<br>999,9 | 488,8<br>549,9 | -2,92<br>-3,28 | 2,39<br>2,68 |

### *2.5 Characterization of Boride Layers*

The microstructure of samples subjected to boriding is investigated by cutting the sample through the center and measuring the boride layer thickness. The sample is then mounted in bakelite, and its surface is prepared for grinding by polishing it for 2 minutes with Akasel Piatto 220+ diamond grinding paper. For the GB40 material, the etching solution is prepared by mixing 10 ml of hydrochloric acid and 10 ml of hydrogen peroxide (30%). The etching process is performed by immersion for 2 minutes. Following the boriding process, the morphology of the boride layer was examined using optical microscope analysis with a Nikon ECLIPSE ME 600 optical microscope located in the Metallography Laboratory of the Department of Metallurgical and Materials Engineering at Dokuz Eylül University, Faculty of Engineering. The etching process is performed by immersion for 2 minutes. After the boriding processes of the samples, XRD analyses were conducted to investigate the effects of boriding and the phases of the boride layers formed on the surface of the samples. XRD analyses of the samples were carried out using a Rigaku brand X-ray diffractometer (XRD) at Dokuz Eylül University. Measurements were taken between 2θ angles of 15° and 90° with a wavelength of θλ =1.79021 Å. Hardness measurements of the boride layer were performed on cross-sections of the samples obtained after the boriding process. These measurements were conducted using a Vickers hardness tester to determine the hardness variation from the surface to the core. The measurements were carried out under conditions requiring high precision, with a load of $HV_{0.1}$, and the hardness profile of the boride layer, progressing from the surface to the inner regions, was analyzed in detail. After the completion of the fatigue tests, the fracture surfaces of the samples were carefully analyzed. This analysis was

conducted to reveal in detail the changes induced in the microstructure of the samples by the boriding heat treatment. The examination was performed using a Quanta-FEG 250 model scanning electron microscope (SEM) with advanced imaging capabilities, available at the Central Laboratory of İzmir Institute of Technology. Through this microscope, the morphological and microstructural characteristics of the fracture surfaces were observed at high resolution, and the structural effects of the boriding process were thoroughly investigated.

## 3.Results

### *3.1 Characterization of Boride Layers*

The boriding process was carried out at temperatures of 900, 950, and 1000°C for 4 hours. Following the boriding process, the morphology of the boride layer was examined using optical microscope analysis, and the thickness of the boride layer was measured at five different points. The boride layer thickness of the sample borided at 900°C is shown in Figure 4. Based on this analysis, the average boride layer thickness of the sample borided at 900°C was measured to be 62 µm. The boride layer thickness of the sample processed at 950°C is shown in Figure 5, with the thickness measured at 148 µm. According to the results of the process conducted at 1000°C, the boride layer thickness is shown in Figure 6, where the thickness was measured to be 155 µm. The analysis indicates that the boride layer thickness of the WC-Co samples increased with rising temperature.

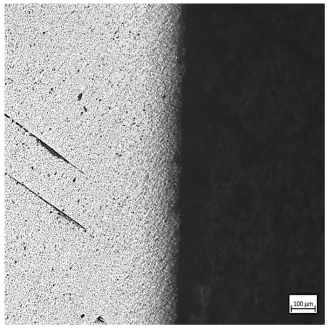

**Fig.4.** The results of the boriding process at 900°C.

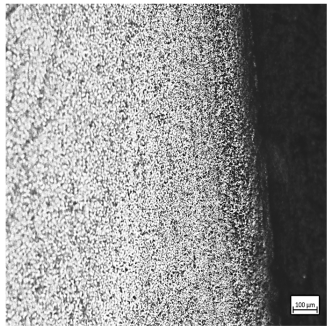

**Fig.5.** The results of the boriding process at 950°C.



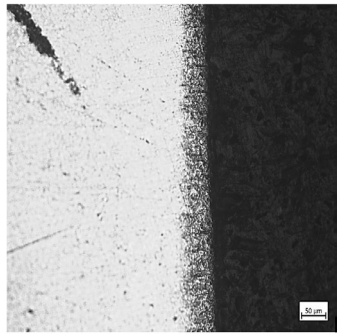

**Fig.6.** The results of the boriding process at 1000°C.

The growth of the boride layer follows a diffusion-controlled mechanism, which can be modeled using Einstein's diffusion equation. In this study, the kinetics of boride layer growth were analyzed using diffusion equations and the Arrhenius relationship. Based on the given temperatures and boride layer thicknesses, the boride layer growth rate constant (K) was calculated, and the activation energy (Q) along with the pre-exponential factor ($K_0$) were determined. These findings align with previous studies, which indicate that boride layer growth in borided materials is primarily governed by temperature-dependent diffusion mechanisms [22].

$$x^2 = Kt \tag{5}$$

where x is the boride layer thickness (µm), K is the temperature-dependent growth rate constant (µm²/s), and t is the boriding time (s). The temperature dependence of K follows the Arrhenius equation:

$$K = K_0 \exp\left(-\frac{Q}{RT}\right) \tag{6}$$

The layer growth rate constant (K), expressed in m²/s, represents the rate at which the boride layer forms during the boriding process. The pre-exponential factor ($K_0$), also in m²/s, is a material-specific parameter accounting for the frequency of successful diffusion events. The activation energy (Q), in J/mol, denotes the minimum energy required for the diffusion process. The universal gas constant (R), with a value of 8.314 J/(mol·K), is used in the Arrhenius equation to relate the growth rate to temperature. Finally, the absolute temperature (T), in Kelvin (K), plays a critical role in determining the kinetics of boride layer formation, as higher temperatures accelerate diffusion and enhance layer growth. The calculated K values and temperatures were used to determine ln(K) and 1/T values, which are presented in Table 4. A clear linear relationship was observed in the Arrhenius plot ln(K) vs. 1/T, shown in Figure 7, which yielded an activation energy of 496.5 kJ/mol for the boriding process. The equation of the best-fit line, determined using the least squares method, is:

$$\ln(K) = -59706.T^{-1} + 10.47 \tag{7}$$

The high coefficient of determination ($R^2$ = 0.98) confirms the strong linearity and reliability of the Arrhenius fit to the experimental data. In Equation (7), the slope of the linear regression line (−59706) corresponds to the term −Q/R in the linearized form of the Arrhenius equation as given in Equation (6). This value suggests that boride layer formation in WC-Co cemented carbide follows a diffusion-controlled mechanism, where increasing temperature significantly enhances boron diffusion and, consequently, boride layer thickness. The experimental results show that as the boriding temperature increases, the diffusion rate also rises, resulting in a progressive increase in the thickness of the boride layer. Among the tested conditions, the highest diffusion rate and the most substantial boride layer formation were observed at 1000°C, confirming the direct correlation between temperature, diffusion kinetics, and boride layer growth.

**Table 4.** Diffusion Kinetics Parameters for Borided WC-Co Specimens.

| Temperature (°C) | Temperature (K) | 1/T ($K^{-1}$) | K ( $m^2/s$) | ln(K) | Boriding thickness (µm) |
|---|---|---|---|---|---|
| **900** | 1173 | $8.52x10^{-4}$ | $2.67x10^{-16}$ | -36.06 | 62 |
| **950** | 1223 | $8.18x10^{-4}$ | $1.52x10^{-15}$ | -34.03 | 148 |
| **1000** | 1273 | $7.85x10^{-4}$ | $1.67x10^{-15}$ | -33.93 | 155 |

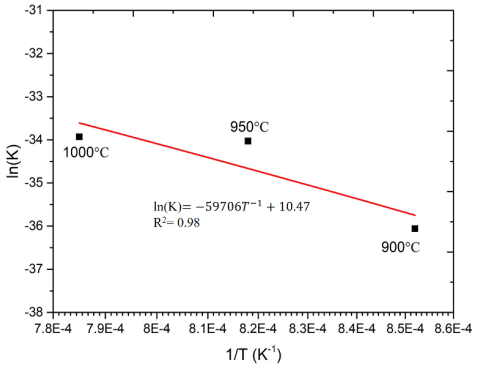


**Fig.7.** Arrhenius Plot: Temperature dependence of the boride layer growth rate constant (ln(K) vs. 1/T)

### *3.1.1 XRD*

The XRD patterns presented in Figure 8 clearly reveal the characteristic peaks of the WC and Co phases in the untreated sample. Following the boriding process, the formation of $W_2CoB_2$, CoB, and $Co_2B$ phases was observed at 900°C, while the increase in temperature to 950°C and 1000°C resulted in the pronounced emergence of the $WB_2$ Phase [23]. Notably, the formation of the $WB_2$ phase at 1000°C exhibits a strong correlation between the observed diffraction peaks and the reference data from the database, confirming its presence with high accuracy. These findings demonstrate that the boriding temperature directly influences the phase composition of the sample [23, 24]. The boriding process facilitates the formation of CoB and WCoB phases through chemical reactions between Co and B atoms, significantly enhancing the material's hardness and wear resistance. Increasing the temperature facilitates the formation of the $WB_2$ phase, further improving the material's mechanical properties, particularly its hardness and toughness [24]. The rise in boriding temperature induces noticeable phase transformations and structural changes in the X-ray diffraction (XRD) patterns.



The increase in boriding temperature caused distinct phase transformations and structural modifications in the X-ray diffraction (XRD) patterns. In the spectrum of the untreated sample, sharp and intense peaks corresponding to WC and Co phases are observed. However, as the boriding temperature increases, a significant reduction in the intensity of these peaks occurs. This phenomenon is attributed to the diffusion of boron atoms into the Co matrix, leading to the formation of new boride phases ($W_2CoB_2$, CoB, $WB_2$, and $Co_2B$) and the partial dissolution of the WC phase. The boriding process conducted at 1000°C resulted in the highest boride phase content, indicating an accelerated boron diffusion kinetics at elevated temperatures. Regarding peak broadening, boride phases formed at lower temperatures (900°C) exhibited relatively narrow peaks. However, as the temperature increased, peak broadening and shifts were observed due to variations in crystal size and internal stresses. High temperatures accelerate atomic diffusion processes, increasing micro-stresses and consequently leading to broader diffraction peaks. Additionally, the more intense formation of $WB_2$ and $Co_2B$ phases at 1000°C suggests that higher temperatures significantly enhance the boriding kinetics. While lower temperatures (900°C and 950°C) resulted in relatively lower amounts of boride phases, the formation of a more stable and well-developed boride layer at 1000°C was evident.

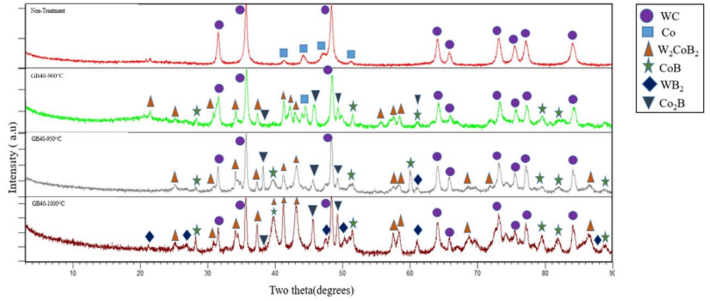


**Fig. 8.** XRD analyses after the boriding process.

The hardness measurements taken at 10 µm intervals from the surface to the core in the boridedsamples, revealed that the highest hardness value, 4104 $HV_{0.1}$, was recorded at the borided region at 1000°C, while the lowest hardness value of 3064 $HV_{0.1}$ was observed in the sample borided at 900°C as shown in Figure 9. As measurements progressed from the surface to the core, these values began to decrease as the boride layer thinned. Compared to the untreatment sample, the hardness value achieved through boriding increased approximately 3.93 times at the surface. The microhardness values, ranging from 3000 to 4500 $HV_{0.1}$, are typically associated with the formation of multi-phase boride compounds on the surface of borided materials [25].

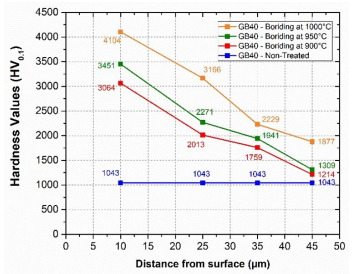


**Fig. 9.** Hardness values measured from the surface of the samples.

### *3.2 Wear Test Results*

Pin-on-plate wear tests were performed after the 4-hour boriding process to evaluate the wear behavior of the borided samples, revealing significant differences in wear performance between non-lubricated and lubricated conditions. For the untreated GB40 sample, wear track measurements were conducted using an optical microscope at 20X magnification. Under non-lubricated conditions, the wear track width was measured as 468,86 µm (Figure 10(a)), whereas in lubricated conditions, it was notably reduced to 316.12 µm (Figure 10(b)). Wear tests under non-lubricated and lubricated conditions were conducted on borided samples processed at different temperatures for 4 h. At 900°C, the wear track width under non-lubricated conditions was measured as 234.31 µm (Figure 11(a)), while lubricated conditions reduced this width significantly to 171.67 µm (Figure 11(b)). For samples borided at 950°C, the wear track width decreased markedly to 228.20µm under non-lubricated conditions (Figure 12(a)) and 118.07 µm under lubricated conditions (Figure 12(b)). At 1000°C, the wear track widths were further reduced, measuring 183.03 µm under non-lubricated conditions (Figure 13(a)) and 70.76 µm in lubricated conditions (Figure 13(b)). These results demonstrate a clear improvement in wear resistance with increasing boriding temperature, particularly under lubricated conditions. The wear track widths were measured to be narrower under lubricated conditions than under non-lubricated conditions. The primary reason for this result is that lubricated conditions reduce frictional resistance during wear. This improvement can be attributed to the reduction in friction forces and the protective role of the lubricant film. Lubrication significantly reduces wear and material loss by minimizing direct contact between surfaces. It has been observed that the lubricated environment provides a robust protective barrier, reducing the wear rate of the boride layer and extending the material's service life.

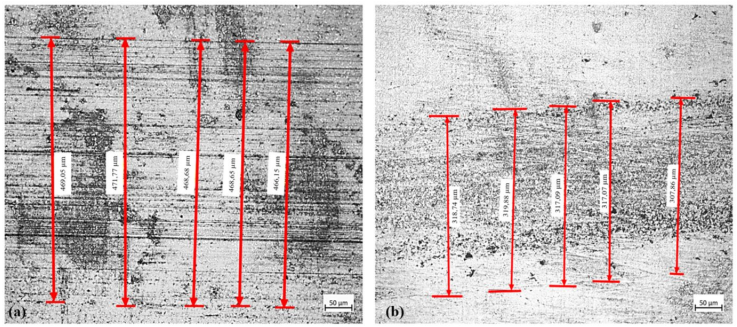


**Fig.10.** Wear track widths measured on the surface of the untreated GB40 sample (a) non-lubricant (b) lubricated.

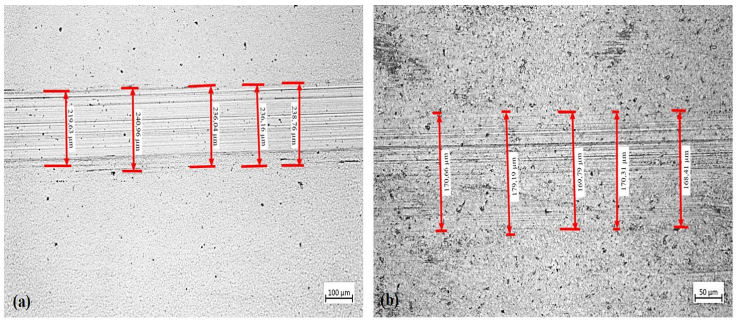


**Fig.11.** Wear track widths measured on the surface on the surface of the sample borided at 900 °C for 4hour sample (a) non-lubricant (b) lubricated.



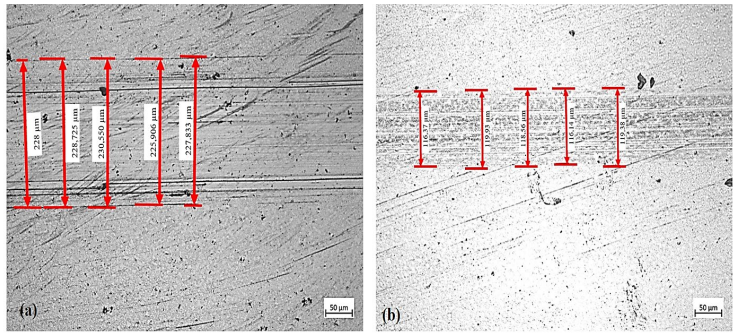


**Fig.12.** Wear track widths measured on the surface on the surface of the sample borided at 950 °C for 4hour sample (a) non-lubricant (b) lubricated.

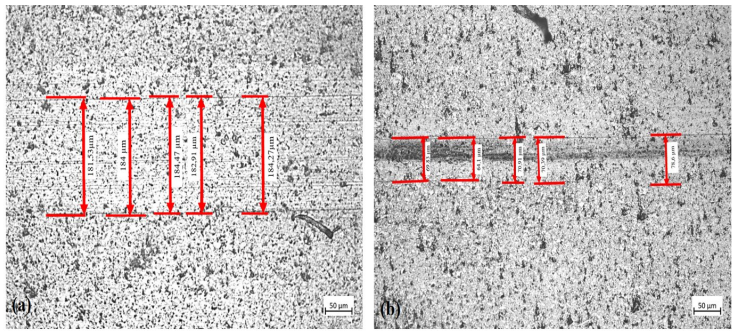


**Fig.13.** Wear track widths measured on the surface on the surface of the sample borided at 1000 °C for 4hour sample (a) non-lubricant (b) lubricated.

The data in the table were obtained by averaging five measurements and rounded to the nearest whole number. The bar chart in Figure 14 illustrates the comparative test results of wear tests conducted under non-lubricated and lubricated conditions. It shows the wear track widths of the untreated sample and the samples treated at 900°C, 950°C, and 1000°C, respectively. These data enable the analysis of the effects of different heat treatment temperatures and environmental conditions on the wear behavior of the samples. The figure 15 shows the variation of the coefficient of friction (µm) as a function of sliding time for borided WC-Co samples processed at different temperatures (900°C, 950°C, and 1000°C) under both non-lubricated and lubricated conditions. The results indicate that friction behavior is significantly influenced by both boriding temperature and lubrication. Under non-lubricated conditions, the highest friction coefficient is observed in the 900°C borided.

sample, reaching approximately 0.28 µ, followed by the 950°C sample in, which stabilizes around 0.17 µ. In contrast, the 1000°C borided sample exhibits the lowest friction coefficient under non-lubricated conditions, remaining below 0.10 µ. This trend suggests that increasing the boriding temperature enhances the formation of wear-resistant boride phases ($CoB$, $Co_2B$, $WB_2$), reducing adhesion and improving sliding performance. Lubricated conditions significantly reduce the friction coefficient for all samples compared to their non-lubricated counterparts. The 1000°C borided sample demonstrates the lowest friction coefficient under lubrication, maintaining values below 0.05 µ throughout the test. The 950°C and 900°C lubricated samples also show considerable reductions in friction, but their values remain slightly higher

than that of the 1000°C sample. This suggests that higher boriding temperatures promote the formation of a denser and smoother boride layer, which enhances lubrication efficiency and reduces surface wear.

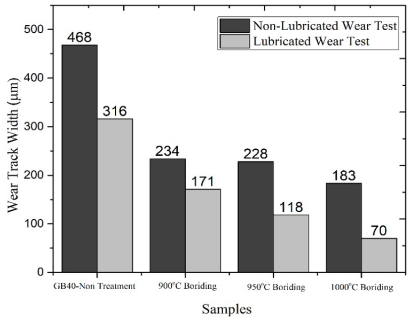


**Fig.14.** Bar chart of the comparative test results of wear tests conducted under non-lubricated and lubricated conditions.

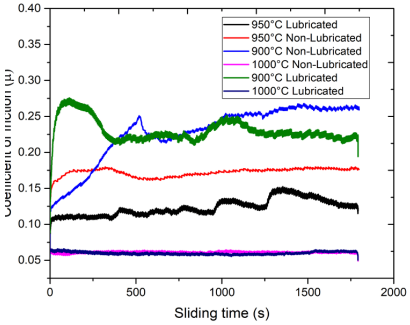


**Fig.15.** Effect of boriding temperature and lubrication conditions on the coefficient of friction of borided WC-Co samples.

### *3.3 Surface Roughness Results*

The results obtained from the friction test are presented in Figure 16 below. These data were measured before the wear test. It was observed that there was a significant increase in surface roughness with increasing boriding temperature. This increase is attributed to the structural properties of the boride layer formed during the boriding process. At higher temperatures, the diffusion of boron atoms into the material surface occurs more intensely, leading to the formation of a thicker and harder boride layer. This layer induces microstructural changes on the surface, resulting in an increase in roughness. According to this graph, the Ra values of the samples are as follows: the Ra value of the untreated sample 0.015 µm; the Ra values of the samples with boriding processes are 0.059 µm at 900°C, 0.114 µm at 950°C, and 0.146 µm at 1000°C.



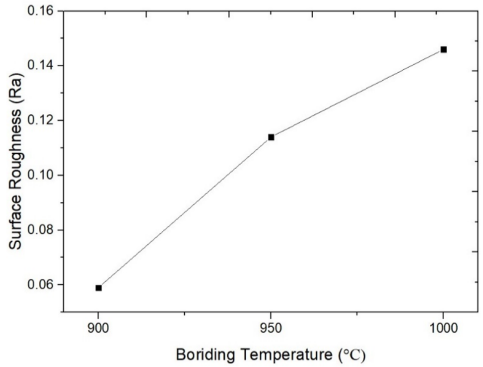


**Fig. 16.** Comparison of surface roughness values at different temperatures resulting from the boriding process.

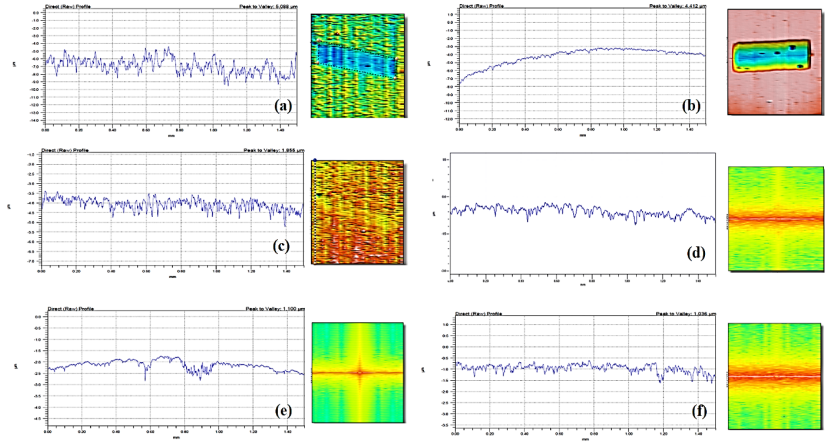


**Fig.17.** Surface Roughness Evaluation of Borided WC-Co: Non-lubricated vs. Lubricated Conditions at Different Temperatures **a)** 900°C-non lubricated, **b)** 900°C lubricated, **c)** 950°C non-lubricated, **d)** 950°C lubricated, **e)** 1000°C non-lubricated, **f)** 1000°C lubricated.

According to profilometer measurements, the surface morphology and wear mechanisms of the borided WC-Co samples exhibited significant differences depending on the applied temperature and lubrication conditions. Borided samples at 900°C exhibited the most irregular wear patterns compared to other temperatures, as shown in Figure 17(a). Under lubricated test conditions, as depicted in Figure 17(b), the surface was significantly rougher, with pronounced irregular wear tracks forming under mechanical loads. The peak-to-valley difference at 900°C under non-lubricated conditions was recorded as 5.088 µm, indicating that the boride layer formed at lower boriding temperatures resulted in non-uniform wear. Although lubrication at 900°C reduced the peak-to-valley difference to 4.412 µm, the mechanical performance of these samples remained inferior compared to those borided at higher temperatures. The wear resistance exhibited a notable improvement upon reaching 950°C. Under non-lubricated test conditions, as shown in Figure 17(c), the peak-to-valley difference was measured at 1.865 µm, with noticeable surface roughness and deformation. However, when lubrication was applied, the peak-to-valley difference significantly decreased to 1.038 µm, demonstrating that

lubrication effectively reduced friction and contributed to a more controlled wear process, as seen in Figure 17(d). Borided samples at 1000°C exhibited the smoothest surfaces and the highest wear resistance. Even under non-lubricated test conditions, as shown in Figure 17(e), the surface remained relatively uniform, with wear being localized to specific areas. The peak-to-valley difference in these samples was 1.100 µm under non-lubricated conditions, further reducing to 1.036 µm under lubrication, as presented in Figure 17(f). The homogeneous wear pattern observed under lubricated conditions suggests that the denser boride layer formed at 1000°C enhanced wear resistance and surface stability. Upon thorough analysis, Profilometer analyses demonstrated that lubrication enhanced wear performance across all boriding temperatures. This improvement was particularly evident at elevated boriding temperatures. The lowest surface roughness and the most uniform wear morphology were obtained in samples borided at 1000 °C under lubricated conditions. In contrast, the samples borided at 900 °C exhibited the highest surface roughness and non-uniform wear patterns. These findings confirm that both boriding temperature and lubrication are critical parameters in improving wear resistance and surface quality in WC-Co materials.

### *3.4 Fatigue Test Results: Goodman-Haigh Diagram*

In WC-Co composites, binder/carbide interfaces and carbide/carbide grain boundaries are typically present. Therefore, the microstructure is generally regarded as a continuous metallic binder phase surrounding discrete carbide particles [20]. In Figure 18(a), the cross-sectional morphology of the sample borided at 900 °C is shown, having been captured in secondary electron (SE) mode, while in Figure 18(b), the corresponding image acquired in backscattered electron (BSE) mode is presented, where compositional contrast between the matrix and boride phases is revealed. The boride layer formed on the surface as a result of the boriding process can be clearly distinguished through microscopic examinations. This layer, with a thickness of approximately 62 µm, contributes significantly to the enhancement of surface hardness and wear resistance. Under the boride layer, a diffusion zone is present, where boron atoms penetrate the base material. This diffusion zone forms a transition area between the surface and the base material, further enhancing the structural integrity and performance of the layer. Goodman–Haigh diagrams, obtained from the results of three-point bending tests, were applied to investigate the fatigue behavior of the WC-Co material following the boriding process. According to the Goodman–Haigh diagram results at 900 °C, as shown in Figure 19, the fatigue life of the borided samples under cyclic loading (R = 0.1) was determined, particularly at stress levels of 450 MPa and 400 MPa. The average fatigue life at 400 MPa was measured as 3.449.647 cycles, whereas this value decreased to 1.670.112 cycles when the applied stress was increased to 450 MPa. As shown in Figure 19, the fatigue life of the borided samples is reduced by approximately 50% under higher loading conditions. The hardness value of the GB40 sample measured before the boriding process was 1043 $HV_{0.1}$, whereas a maximum value of 3064 $HV_{0.1}$ was recorded after the boriding treatment at 900 °C. The formation of hard boride phases such as $W_2CoB$, CoB, and $Co_2B$ contributed to improved wear resistance, while reducing the material's resistance to fatigue.

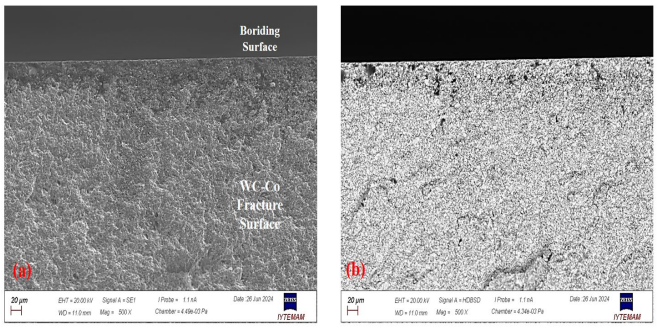


**Fig. 18.** Cross-sectional view of the sample borided at 900°C: (a) 500X SE, (b) 500X BSE, layer thickness 62 microns.

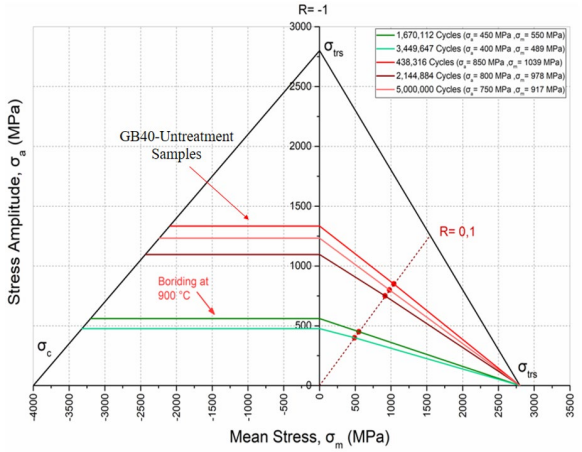


**Fig. 19.** Goodman-Haigh diagram of the sample resulting from the boriding process at 900°C.

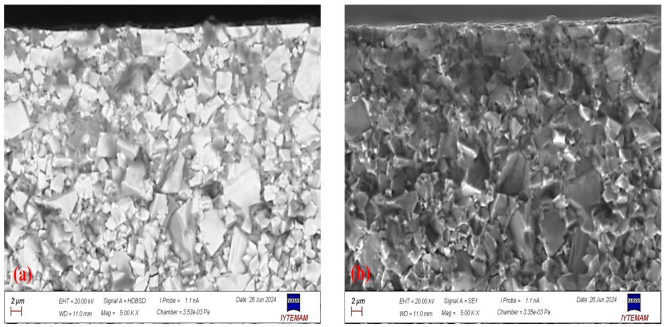


**Fig. 20.** SEM examination of the surface after the three-point bending test of WC-Co and the boride layer at 900°C for 4 hours: (a) BSE, (b) SE.

Figure 20(a) shows the SEM-BSE image of a distinct area of WC phase fracture. Figure 20(b) displays the fracture surfaces of WC particles in the SE analysis examined in SEM. Intragranular fractures are observed in WC particles, both parallel to the fracture surface and at an angle to it. Independent of the WC grain fracture surfaces, brittle fracture surfaces are also detected in the cobalt phase. The formation of these brittle fracture surfaces may be due to the stress accumulation between WC particles and the $W_2CoB$, CoB and $Co_2B$ structures present on the surface.

Following the increase in temperature to 950 °C, the boride layer is not observed to exhibit a clear transition zone on the fracture surface, as shown in Figure 21(a) and 21(b). In Figure 21(a), the SEM image captured in secondary electron (SE) mode is presented, while in Figure 21(b), the image captured in backscattered electron (BSE) mode is shown. In Figure 22, the graph of the three-point bending test conducted under same loading conditions (400 and 450 MPa) after the boriding process at 950 °C is illustrated. This test condition resulted in a more significant improvement in die life compared to other boriding conditions. The fatigue life, measured as 5.000.000 cycles at 400 MPa, was reduced to 1.525.507 cycles at 450 MPa with the increase in applied force. The improvement observed at 400 MPa can be attributed

to two main factors. First, the boride layer thickness obtained from the boriding process at 950 °C is considered to provide an optimal layer geometry on the surface of the WC-Co material, contributing to enhanced fatigue performance. This layer improves wear resistance by increasing surface hardness and minimizes the tendency for crack formation. The optimal thickness eliminates the detrimental effects associated with the boride layer being either too thin or excessively thick [14]. At 950 °C, as the boride layer is examined in both BSE and SE modes in the SEM images provided in Figure 23(a) and (b), it is observed that the WC particles predominantly exhibit brittle intragranular fracture surfaces oriented parallel to the overall fracture surface, as shown in Figure 23(a). Furthermore, the cobalt phase located between the WC grains is observed to transfer stress from each grain toward the center of the phase, where two distinct fracture surfaces converge, resulting in the formation of a cavity or hollow, as illustrated in Figure 23(b) [26].

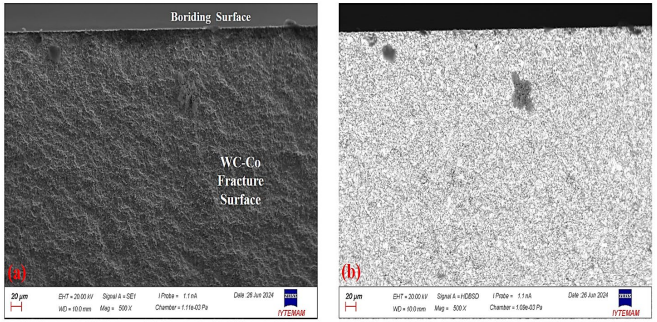


**Fig.21.** Cross sectional of the sample 950°C boriding at: (a) 500X SE (b) 500X BSE layer thickness 148 micron.

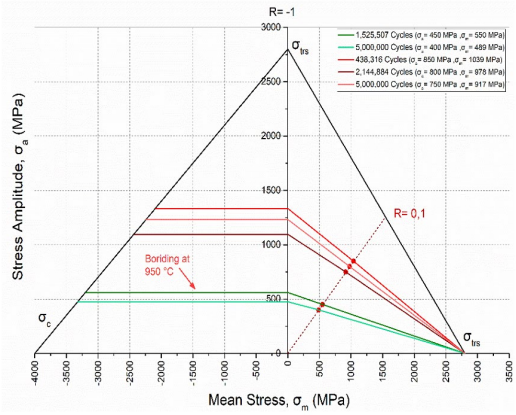


**Fig.22.** Goodman-Haigh diagram of the sample resulting from the boriding process at 950°C.



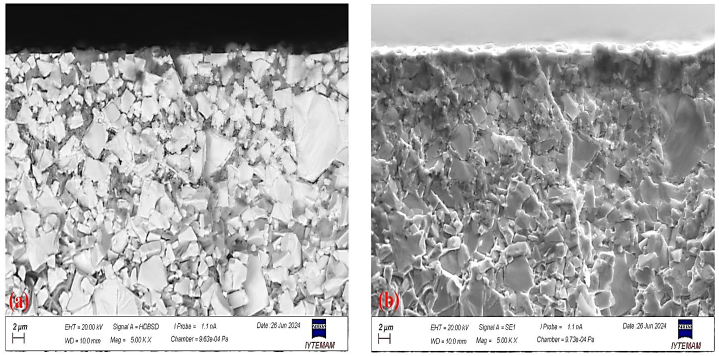


**Fig. 23.** SEM examination of the fracture surface of the sample borided at 950°C after the fatigue test: (a) BSE, (b) SE.

Three-point fatigue tests conducted at 400 MPa and 450 MPa were used to evaluate the effect of boriding at 1000 °C, as illustrated in Figure 24. Under these test conditions, a decrease in die life was observed when compared to other boriding conditions. The die life, measured as 984.075 cycles at 400 MPa, was reduced to 135.356 cycles at 450 MPa with the increase in applied force. In the boriding process, where the temperature was varied while the duration remained constant, a linear relationship was observed between the boriding temperature and the depth of the boride layer at different temperatures. In Figure 25(a), the fracture surface after the three-point bending test is shown, having been examined in SEM using backscattered electron (BSE) imaging. The growth rate of the WB layer was found to induce stress accumulation at the WB/W interface [14]. As the boriding temperature increased, the hardness of the $WB_2$ phase in the boride layer contributed to improved wear resistance compared to other samples at 1000 °C. However, the increased brittleness of the $WB_2$ phase may have facilitated crack initiation at the surface. This brittle boride layer is likely to shorten the fracture life of the borided material [27]. Additionally, the increased thickness of the boron layer at higher temperatures was found to negatively affect the fracture toughness, thereby reducing the material's resistance to crack propagation [27]. This phenomenon was observed at 950 °C, but not at 900 °C. New phase formation around the WC grains was observed at 1000 °C, as shown in Figure 25(a). Moreover, at higher boriding temperatures, surface roughness was found to increase. A rougher surface can create zones of stress concentration, which promote crack initiation and reduce the overall fatigue life of the material. In Figure 25(a), an edge region featuring curved lines is visible, appearing as if covered by a melted and re-solidified layer, where the sharp edges of the WC grains have disappeared. This layer represents an intermediate phase rich in tungsten (W), formed as a result of diffusion from the cobalt matrix surrounding the WC grains, which also influences the surface coloration. Additionally, small white spots were observed on the cobalt fracture surface in both (a) BSE and (b) SE modes. These small indentations and protrusions on the cobalt fracture surface are indicative of a second phase precipitated within the cobalt matrix as a result of diffusion. As demonstrated in the figure, the high hardness of the boride layer can cause stress accumulation at the material's surface. These stresses can lead to the propagation of cracks from the surface into the material. Furthermore, weak interfacial bonding between the boride layer and the WC-Co matrix may also promote crack propagation from the surface into the interior, as shown in Figure 25(b).

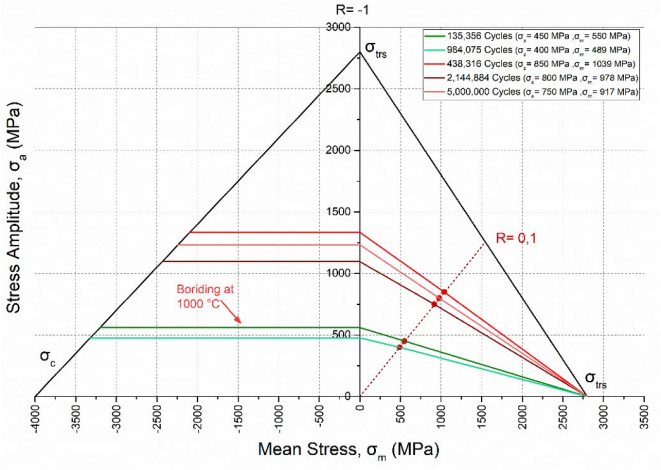


**Fig. 24.** Goodman-Haigh diagram of the sample resulting from the boriding process at 1000°C.

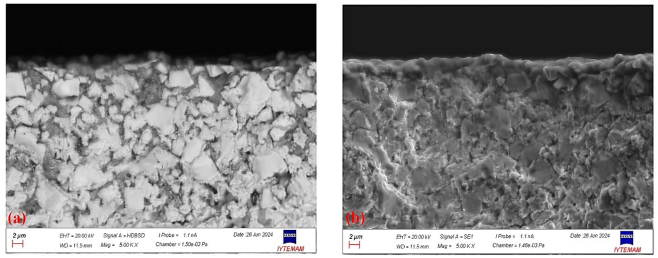


**Fig. 25.** Cross sectional of the sample 1000°C boriding at: (a) 500X BSE; (b)500X SE.

## 4. Conclusions

This work aims to investigate the surface properties of WC-Co materials, used as die inserts in cold forging applications, through boriding at three different temperatures for a duration of 4 hours. The study focuses on a detailed evaluation of hardness, wear resistance, microstructural characteristics, and fatigue performance. The main findings of this study are outlined below:

• The formation of the boride layer in WC-Co cemented carbides follows a diffusion-controlled mechanism, in which increasing temperature enhances boron diffusion and promotes layer growth. Arrhenius analysis confirmed a linear relationship between ln(K) and 1/T, yielding an activation energy of 496.5 kJ/mol. The experimental results revealed that the highest diffusion rate was observed at 1000 °C, where the growth rate constant (K) reached $1.67 \times 10^{-15}$ $m^2/s$, while the lowest was recorded at 900 °C with a value of $2.67 \times 10^{-16}$ $m^2/s$, demonstrating the significant influence of temperature on boride layer kinetics.

• XRD analysis revealed that boriding at 900 °C led to the formation of $W_2CoB_2$, CoB and $Co_2B$ phases. An increase in temperature to 950 °C resulted in the additional appearance of $WB_2$, indicating progressive phase transformations. At 1000 °C, the dominant formation of $WB_2$ and $Co_2B$ indicated an increase in boron diffusion kinetics, elevated micro-stresses and the development of a more stable and well-defined boride layer.

• The Ra values of the samples before wear testing were measured as follows: 0.015 µm for the untreated sample, and 0.059 µm, 0.114 µm, and 0.146 µm for the borided samples at 900 °C, 950 °C, and 1000 °C, respectively.

• Profilometer measurements indicated that higher boriding temperatures and the presence of lubrication significantly improved surface quality and wear resistance. The samples borided at 1000 °C exhibited the lowest surface roughness and the most homogeneous wear under lubricated conditions. In contrast, the samples borided at 900 °C showed the highest surface roughness and non-uniform wear, confirming that both temperature and lubrication are critical parameters for optimizing wear performance.

• The wear track width was found to decrease with increasing boriding temperature, reaching 183.03 µm under non-lubricated conditions and 70.76 µm under lubricated conditions at 1000 °C. In comparison, values of 234.31 µm (non-lubricated) and 171.67 µm (lubricated) were measured at 900 °C. In parallel, the highest microhardness value of 4104 $HV_{0.1}$ was obtained at 1000 °C, whereas the lowest value of 3064 $HV_{0.1}$ was recorded at 900 °C, indicating a direct correlation between boriding temperature, surface hardness, and wear resistance.

• The boriding process at 900 °C was found to negatively affect the fatigue performance of WC-Co composites, as obtained from the Goodman–Haigh diagram results, where a significant reduction in fatigue life was observed under cyclic loading conditions. At 400 MPa, the average fatigue life was recorded as 3.449.647 cycles, whereas an increase in stress to 450 MPa resulted in a decrease to 1.670.112 cycles. These results indicate that although boriding improves wear resistance, it also promotes brittle behavior and contributes to reduced fatigue strength.

• The optimum fatigue performance was obtained at 950 °C, at which the boride layer exhibited an optimized thickness that ensured an effective balance between crack resistance and brittleness. Under cyclic loading, the fatigue life reached 5.000.000 cycles at 400 MPa and decreased to 1.525.507 cycles at 450 MPa, indicating that the boriding treatment at 950 °C resulted in optimal improvement in fatigue resistance.

• The boriding process at 1000 °C resulted in an increased boride layer thickness and the formation of the $WB_2$ phase, which improved wear resistance but substantially reduced fatigue life due to increased brittleness and stress concentration at the WB/WC interface, thereby facilitating early-stage crack initiation. At this highest boriding temperature, the fatigue life was reduced to 984.075 cycles at 400 MPa and 135.356 cycles at 450 MPa, indicating the negative contribution of excessive boride layer growth to the degradation of crack growth resistance.

• The thickness of the boride layer increased with rising boriding temperature, leading to stress concentrations at the surface and negatively affecting the material's fatigue strength. The formation of a brittle boride layer facilitated crack initiation and propagation, resulting in a reduction in the fracture life of the borided samples. Therefore, in addition to improvements in surface hardness and wear resistance, the embrittlement induced by boriding must be carefully considered due to its negative effect on fatigue performance.

• Significant structural changes were observed during the boriding process, particularly in materials with complex microstructures such as WC particles and the Co matrix. The change in the interactions between WC particles and the surrounding matrix was found to compromise the microstructural integrity of the material and negatively affect its fracture resistance.

• Future research will focus on validating the performance of borided WC-Co die materials in industrial cold forming processes. Specifically, long-term wear resistance, fatigue behavior, and service life of borided dies will be systema-

tically evaluated under practical manufacturing conditions. In addition, hybrid surface treatments and post-boriding modifications will be investigated to reduce boride layer brittleness and improve material toughness. Optimization of boriding parameters and identification of the most suitable processing conditions for various industrial applications will also be explored to maximize material performance. These efforts aim to enhance the industrial applicability of boriding and provide a comprehensive understanding of its effects on WC-Co cold forming dies.

## References


1 H.M. Ortner, P.Ettmayer, H. Kolaska, I.Smid, The history of the technological progress of hardmetals, International Journal of Refractory Metals and Hard Materials, 49 (2015) 3-8. https://doi.org/10.1016/j.ijrmhm.2014.04.016

2 García, J., Collado Ciprés, V., Blomqvist, A., & Kaplan, B. (2019). Cemented carbide microstructures: A review. International Journal of Refractory Metals and Hard Materials, 80, 40-68. https://doi.org/10.1016/j.ijrmhm.2018.12.004

3 Chang, S.-H., & Chen, S.-L. (2014). Characterization and properties of sintered WC–Co and WC–Ni–Fe hard metal alloys. Journal of Alloys and Compounds, 585, 407-413. https://doi.org/10.1016/j.jallcom.2013.09.188y

4 K. Wagner, A. Putz, and U. Engel, "Improvement of tool life in cold forging by locally optimized surfaces," Journal of Materials Processing Technology, vol. 177, no. 1-3, pp. 206-209, 2006.

5 ISO 4419-2:2020. (2020). Hardmetals – Metallographic determination of microstructure – Part 2: Measurement of WC grain size. International Organization for Standardization.

6 Wittmann, B., Schubert, W.-D., & Lux, B. (2002). WC grain growth and grain growth inhibition in nickel and iron binder hardmetals. International Journal of Refractory Metals and Hard Materials, 20(1), 51-60. https://doi.org/10.1016/S0263-4368(01)00070-1

7 J.García, V.C. Ciprés, A. Blomqvist, B. Kaplan, Cemented carbide microstructures: a review, International Journal of Refractory Metals and Hard Materials, 80 (2019) 40-68. https://doi.org/10.1016/j.ijrmhm.2018.12.004

8 Konyashin, I. (2023). Approaching the 100th anniversary of the hardmetal invention: From first WC-Co samples towards modern advanced hardmetal grades. International Journal of Refractory Metals and Hard Materials, 111, 106113. https://doi.org/10.1016/j.ijrmhm.2023.106113

9 Öztürk, K. (2021). Plastik kalıp çeliklerinin korozyona karşı korunmasında kutu borlama işleminin etkileri (Yüksek lisans tezi, Dokuz Eylül Üniversitesi Fen Bilimleri Enstitüsü, İzmir).

10 Kara, R., Colak, F., & Kayali, Y. (2015). Investigation of wear and adhesion behaviors of borided steels. Transactions of the Indian Institute of Metals, 69(6). https://doi.org/10.1007/s12666-015-0698-2

11 Lin, G., Zhang, Z., Qiu, Z., Luo, X., Wang, J., & Zhao, F. (2013). Boronizing mechanism of cemented carbides and their wear resistance. International Journal of Refractory Metals and Hard Materials, 41, 351-355. https://doi.org/10.1016/j.ijrmhm.2013.05.008

12 Köksal, S. (2009). The characterization of WC-Co based materials boronized within molten salt bath. Solid State Phenomena, 144, 261-266. https://doi.org/10.4028/www.scientific.net/SSP.144.261

13 Dearnley, P. A., Schellewald, M., & Dahm, K. L. (2005). Characterisation and wear response of metal-boride coated WC–Co. Wear, 259(7-12), 861–869. https://doi.org/10.1016/j.wear.2005.01.031

14 Usta, M., Ozbek, I., Ipek, M., Bindal, C., & Ucisik, A. H. (2005). The characterization of borided pure tungsten. Surface and Coatings Technology, 194(2–3), 330–334. https://doi.org/10.1016/j.surfcoat.2004.06.042





15 Márquez-Herrera, A., Bermúdez-Rodríguez, G., Hernandez-Rodríguez, E., & Zapata-Torres, M. (2016). Boride coating on the surface of WC–Co-based cemented carbide. International Journal of Materials Research, 107(6), 1–3. https://doi.org/10.3139/146.111387.

16 Aydoğmuş, T. (t.y.). Tungsten karbür kesici takımların borlanması ve karakterizasyonu (Doktora Tezi, Eskişehir Osmangazi Üniversitesi, Fen Bilimleri Enstitüsü, Fizik Anabilim Dalı, Katıhal Fiziği Bilim Dalı). Eskişehir.

17 Oruç, Ö. (2010). The characterization and wear behaviour of WC-Co based materials boronized within molten salt bath. [Master's thesis, Sakarya University]. Sakarya University Institute of Science, Department of Mechanical Education.

18 Coureaux, D., Sagaro Zamora, R., Calzadilla R., J., & Llanes, L. (2015). Influencia de la microestructura en el comportamiento tribológico de carburos cementados (WC-Co) borados. Ingeniare Revista Chilena de Ingeniería, 23(2), 259–268. https://doi.org/10.4067/S0718-33052015000200010

19 https://www.boehlerit.com/fileadmin/user_upload/PDF/Hartmetall_Carbide.pdf. Böhlerit. (n.d.). Hartmetall Carbide: Material Properties and Applications. Retrieved January 9, 2025, from https://www.boehlerit.com/fileadmin/user_upload/PDF/Hartmetall_Carbide.pdf

20 Hardmetals - Determination of transverse rupture strength, ISO 3327:2009 (2009)

21 ASTM International. (2017). ASTM G99-17: Standard test method for wear testing with a pin-on-disk apparatus. In Annual book of ASTM standards (Vol. 03.02, pp. 1–6). West Conshohocken, PA: ASTM International. https://doi.org/10.1520/G0099-17

22 Özdemir, O., Omar, M. A., Usta, M., Zeytin, S., Bindal, C., & Ucisik, A. H. (2009). An investigation on boriding kinetics of AISI 316 stainless steel. Vacuum, 83(2), 175–179. https://doi.org/10.1016/j.vacuum.2008.03.026

23 Zahariev, Z. T., & Marinov, M. I. (1993). Superhard boride layer deposition on a carbide-cobalt hard alloy. Journal of Alloys and Compounds, 201(1–2), 1–3. https://doi.org/10.1016/0925-8388(93)90852-E

24 Zakhariev, Z., Petrov, K., & Christov, M. (1981). Preparation and some properties of boride diffusion layers on hard WC-TiC-Co alloys. Journal of the Less Common Metals, 82, 57–62. https://doi.org/10.1016/0022-5088(81)90197-1

25 Bartolucci, S., & Schlössin, H. H. (1966). Plastic deformation preceding fracture in tungsten carbide-cobalt alloys. Acta Metallurgica, 14(3), 317–324. https://doi.org/10.1016/0001-6160(66)90092-7

26 Källström, M., Oden, M., & Larsson, A. (2010). Phase stability and mechanical properties of tungsten borides from first principles calculations. Physical Chemistry Chemical Physics, 12(40), 13158-13165. https://doi.org/10.1039/c004122j).

27 Üçisik, A. H., & Bindal, C. (1997). Fracture toughness of boride formed on low-alloy steels. Surface and Coatings Technology, 94–95, 561–565. https://doi.org/10.1016/S0257-8972(97)00466-0


# ANALYTICAL PREDICTION AND EXPERIMENTAL VALIDATION OF BOLT SELF-LOOSENING UNDER VIBRATION

*Can İÇMEZ*
*Umut İNCE*
*Samed ENSER*

The European Journal of Research and Development

# ANALYTICAL PREDICTION AND EXPERIMENTAL VALIDATION OF BOLT SELF-LOOSENING UNDER VIBRATION

**Can İÇMEZ[1*], Umut İNCE[2], Samed ENSER[3]**

[1]Norm Fasteners, Orcid ID: https://orcid.org/0000-0002-9124-0100, e-mail: can.icmez@normfasteners.com
[2]Norm Fasteners, Orcid ID: https://orcid.org/0000-0002-3118-3060, e-mail: umut.ince@normfasteners.com
[3]Norm Fasteners (Present: Mehmet Akif Ersoy University) Orcid ID: https://orcid.org/0000-0002-6232-5498, e-mail: samedenser@mehmetakif.edu.tr
* Correspondence: can.icmez@normfasteners.com; Tel.: (optional; include country code)

**Reference:** (will be filled by editorial office)

## Abstract

The self-loosening of bolted joints under vibrational loading remains a persistent challenge in many engineering applications, especially in the automotive industry, where safety and reliability are of paramount importance. Predicting self-loosening behavior is challenging because numerous parameters influence joint performance, as well as the limitations of conventional experimental testing. This study presents a novel analytical model for predicting bolt and nut loosening behavior under transverse vibration. The model extends existing approaches by incorporating additional parameters such as displacement, clamping force, and under-head friction torque. To enhance usability, the model was implemented in an MS Excel–based calculator with macro functions, enabling engineers to perform loosening analyses under varying conditions. The model adapts and extends existing approaches from the literature by incorporating an energy equilibrium approach, which calculates bolt rotation by balancing the torsional strain energy accumulated during vibration with the kinetic energy released once the applied torque exceeds the critical threshold. The analytical predictions were validated through Junker vibration tests, showing strong agreement with experimental data. The proposed model and tool provide a practical and accessible method for predicting loosening, thereby enabling the design of safer and more reliable fasteners while strengthening industrial competitiveness.

**Keywords:** Self-loosening, Fasteners, Vibration, Junker test, Analytical modeling

## 1. Introduction

Bolted joints are widely employed in the automotive, aerospace, energy, and civil sectors due to their simplicity and ease of disassembly. However, their reliability is often compromised by self-loosening under vibration, which can lead to preload loss, failures, and safety risks [1]. Among excitation mechanisms, transverse vibration is recognized as the primary cause of self-loosening. Junker's pioneering work [2], which later became standardized as DIN 65151, demonstrated that cyclic lateral displacement promotes slip at the under-head bearing surface and thread interfaces, causing progressive rotation and loss of clamp force. Subsequent investigations showed that loosening can initiate even under micro-slip conditions, where small relative motions accumulate rotation with each vibration cycle [3].

Further studies combined experimental and computational approaches to better capture the mechanics of loosening. Dinger and Friedrich [4] demonstrated that local slip zones under the bolt head and in the threads govern the onset of loosening, identifying critical displacement thresholds below 1 mm. These findings highlighted the importance of preload level, hole clearance, and friction coefficients in predicting loosening behavior.

Additionally, İnce and Güden [5] investigated the self-loosening behavior of bolted joints under cyclic transverse loading experimentally and numerically. Their study showed that existing analytical models could not fully predict the critical transverse displacement, achieving around 58 % accuracy. By introducing finite element–based parameters such as reaction moment and stiffness ratio, critical transverse displacement prediction accuracy improved to approximately 73 %, emphasizing the need for more comprehensive modeling approaches.

Analytical modeling has provided further insights into this problem. Nassar and Housari [6] presented a three-dimensional mathematical model to evaluate the effect of thread and under-head friction coefficients on loosening, implemented in MATLAB and validated experimentally. The results confirmed the central role of friction conditions in governing clamp force decay. Building on this, Nassar and Yang [7] developed an advanced formulation incorporating integral expressions for under-head torque, bolt bending effects, and critical slip forces. The model showed a strong correlation with measured torque–rotation curves, improving predictive accuracy.

More recently, Sun et al. [8] introduced a quantitative evaluation model that simplifies the problem to a single axis and defines two design criteria: an angular-acceleration criterion for loosening onset and a critical transverse load criterion. Their study compared bolts with spherical under-head geometries against standard bolts, both analytically and experimentally, demonstrating enhanced resistance to loosening and illustrating the potential of geometry optimization. Despite these advances, two limitations remain. First, most existing models require specialized software (e.g., MATLAB or finite element packages), which limits accessibility for engineers in practical design environments. Second, adaptability across various parameters, such as coatings, geometries, preload, and assembly conditions, remains limited without extensive re-derivation or numerical simulations.

To address these gaps, this work develops a parameter-adaptive analytical model for predicting bolt and nut loosening rates under transverse vibration. Unlike previous models, the formulation is implemented in an MS Excel–based calculator with macro functions, enabling engineers and technicians to perform loosening analyses across a variety of conditions without advanced coding or simulation tools. In addition, the proposed method introduces an energy equilibrium approach to determine the rotational motion of the bolt. In this approach, the torsional strain energy stored in the bolt during vibration is balanced against the kinetic energy released once the applied torque exceeds the critical torque threshold, allowing the angular displacement and loosening rate to be calculated analytically.

The model is validated through a series of Junker vibration tests, demonstrating strong agreement between analytical predictions and experimental data. The results confirm that the proposed approach accurately captures loosening behavior under different friction coefficients, preload levels, and head geometries. By reducing the need for extensive physical testing, the model shortens product development cycles, decreases testing costs, and promotes more sustainable design by lowering energy and resource consumption. Ultimately, this tool provides a practical pathway for designing safer and more reliable bolted joints while enhancing competitiveness in industries where fastener integrity is critical.

## 2. Materials and Methods

### *2.1. Loosening Mechanism of a Bolt*

The clamping force generated by the tightening torque maintains the integrity of the bolted joint. However, when the joint is exposed to a transverse load that exceeds the frictional resistance created by this clamping force, relative motion begins to occur between the threads and at the interface under the bolt head.

Figure 1 illustrates the motion of the bolt when the upper plate moves in the x-direction. Figure 1(1) shows the initial location of bolt and the plates. As the plate is displaced, it moves together with the bolt until reaching a critical slip point ($\delta_{crit}$) (2). Beyond this point, the bolt begins to slide over the surface of the plate. The sliding continues until the plate reaches its maximum lateral displacement ($\delta^*$) (3). The loosening of the bolt takes place between the critical slip point and the maximum displacement position.

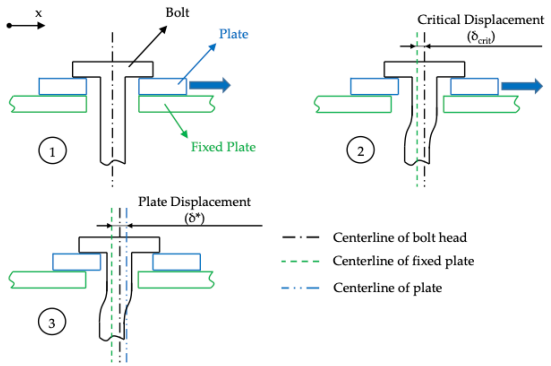


**Figure 1.** Transverse Displacement Behavior of the Bolt During Plate Motion in the x-direction

Figure 2 presents the time-dependent displacement of the plate. In Zone 1, the initial motion occurs as the plate moves from the zero position to its maximum position. Zones 2 and 3 represent the motion of the plate between successive maximum positions.

In this research, the loosening behavior of bolted joints under vibration was examined using the Junker test method, which is the most common approach for evaluating self-loosening performance. Originally developed by Gerhard Junker in 1969 [2], this method applies a controlled cyclic transverse displacement to a preloaded bolted joint while maintaining a constant clamping force. The test simulates real service conditions where bolts are exposed to vibration and lateral movement, such as in automotive or machinery applications. During the test, relative slip occurs between the bearing surface and the threads, causing a gradual reduction in the clamping force. The change in preload is continuously measured throughout the vibration cycles, allowing the loosening behavior to be monitored in real time. The typical result is a clamping-force-versus-cycle curve that shows an initial rapid decrease followed by a steady-state region, indicating the joint's resistance to loosening. Because it provides consistent and comparable results, the Junker test is widely used for evaluation and comparison of the anti-loosening performance of different fastener designs, coatings, and tightening conditions.

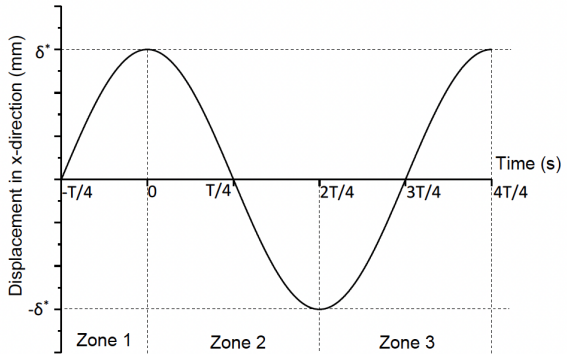


**Figure 2.** Time-Dependent Displacement of Plate in x-direction



### *2.2. Analytical Method for Calculation of Loosening Rate*

During the bolt's complete cyclic displacement, shear friction forces acting on the bolt under-head and threads play an important role in the bolt's loosening behaviour. These forces are formulated by Nassar and Yang 2009 [7] along the x-direction as bearing friction shear force Fbs and thread friction shear force $F_{ts}$.

$$F_{bs} = \frac{3EI_1}{k \times L^3}\,\delta \sin(\omega\, t) \qquad 1)$$

$$k = 1 - \left( \frac{3\lambda_b L}{4\lambda_b L + \frac{16EI_1 r_o}{\pi\left(r_o^4 - r_i^4\right)}} \right) \qquad 2)$$

$$F_{ts} = F_{bs} \times \left[ 1 + \frac{\tan\alpha\, L}{\frac{r_{min}(\tau^4-1)}{2(\tau^3-1)} + \frac{1}{3}r_{maj} + 0{,}2725 \times P} \times \frac{\frac{8EI_1 r_o}{\pi\left(r_o^4 - r_i^4\right)} + \lambda L}{\frac{8EI_1 r_o}{\pi\left(r_o^4 - r_i^4\right)} + 2\lambda L} \right] \qquad 3)$$

In this formulation, k represents the bending factor, E denotes Young's modulus of elasticity, and I1 corresponds to the cross-sectional axial moment of inertia. The geometric parameters L, P, and $\alpha$ define the effective bolt length, thread pitch, and half of the thread profile angle, respectively. The contact dimensions under the bolt head are given by the outer radius $r_o$ and inner radius $r_i$. Furthermore, $\delta$ indicates the transverse displacement of the plate, while $\omega$stands for the angular velocity of the cyclic excitation. Finally, $\lambda_b$ is the constant for under-head bending stiffness, and $\tau$ represents the ratio of the major thread radius (rmaj) to the minor thread radius ($r_{min}$) ($\tau = r_{maj}/r_{min}$.).
These forces create torque, which stops the bolt's rotational movement.

$$T_{bs} = F_{bs} \times r_{be} \qquad 4)$$

$$T_{ts} = F_{ts} \times r_{te} \qquad 5)$$

Where $r_{be}$ is the effective bearing radius and $r_{te}$ is the effective thread radius.

If no loosening occurs during cyclic vibration, the frictional forces acting on the bolt are initially zero and increase sinusoidally as the transverse displacement grows, reaching their maximum amplitude at the point of maximum lateral movement. In this stage, the bolt and clamped parts move together without any relative slip, and the joint remains stable. However, once the applied transverse force exceeds the frictional resistance generated by the clamping load, a critical condition is reached. At this critical point, relative motion begins between the contacting surfaces, initiating the loosening process. Nassar and Yang [6] characterized this transition by defining the critical torques acting on the bolt – specifically, the under-head friction torque, the thread friction torque, and the pitch torque – which together determine the self-loosening. The relationship among these torques can be expressed as:

$$T_{bcr} = F \times \mu_b \times r_{be} \quad (6)$$

$$T_{tcr} = \frac{r_{te} \times \mu_t \times F \times \cos\beta \times \sqrt{\sec^2\alpha + \tan^2\beta}}{1 - \mu_t \times \sin\beta \times \sqrt{\sec^2\alpha + \tan^2\beta}} \quad (7)$$

$$T_P = \frac{F \times P}{2\pi} \quad (8)$$

Where $T_p$, $T_{bcr}$ and $T_{tcr}$ are pitch torque, torque of critical bearing friction and critical thread friction respectively. F is the clamp load, μb and μt are the bearing and thread friction coefficients, $\beta$, $\alpha$ and P are the lead helix angle, half of the thread profile angle and the thread pitch, respectively.

At the critical point $T_{bs}$ reaches up until $T_{bcr}$. During this equilibrium, the bolt start to turn on the loosening direction with a net torque. Which can be expressed as:

$$T_{Net} = T_{ts} - T_{tcr} + T_p \quad (9)$$

Where $T_{Net}$ is the net torque affecting the bolt to rotate in the loosening direction. This torque causes an angular acceleration on the bolt:

$$\alpha = \frac{T_{Net}}{I_2} \quad (10)$$

Where $\alpha$ is the angular acceleration and I2 is the axial moment of inertia. This acceleration will later be used for the calculation of the bolt's loosening time.

In order to determine how much the bolt rotates, it is necessary to calculate its angular velocity. The kinetic energy equation was used to obtain this angular velocity. Until the bolt reaches the critical torque value, it is subjected to torsion. During this stage, torsional strain energy accumulates within the bolt, and once the applied torque exceeds the critical limit, this stored energy is suddenly released as kinetic energy, causing the bolt to rotate.

$$E_{Torsion} = T_0 \times \theta_0 \quad (11)$$

$$\theta_0 = \frac{T_0 \times L}{G \times J} \quad (12)$$

Where $\theta_0$ is the angle of twist, L, G and J are the effective bolt length, the shear modulus and the polar moment of inertia, respectively. $T_0$ represents the residual torque remaining on the bolt, which was calculated from the torque–clamping force tests. It was obtained by multiplying the residual clamping load on the bolt by the experimentally determined T/F ratio.



$$T_0 = F \times \left(\frac{T}{F}\right)_{Exp} \quad (13)$$

Where F is the clamping load. T/F value was determined experimentally by applying torque in the loosening direction and may vary depending on the bolt type.

When the torsional strain energy reaches the critical torque value, it is converted into kinetic energy. This released energy causes the bolt to undergo rotational motion.

$$E_{Kinetic} = \frac{1}{2} \times I_2 \times \omega^2 \quad (14)$$

Considering the law of energy conservation, the accumulated torsional strain energy can be assumed to be equal to the kinetic energy of the bolt. Based on this equilibrium, the angular velocity of loosening can be determined.

$$E_{Torsion} = E_{Kinetic} \quad (15)$$

$$T_0 \times \theta_0 = \frac{1}{2} \times I_2 \times \omega^2 \quad (16)$$

$$\omega = \sqrt{\frac{2 \times T_0 \times \theta_0}{I_2}} \quad (17)$$

Using formulas 10 and 17, the time elapsed during the bolt loosening process can be calculated.

$$t_L = \frac{\omega}{\alpha} \quad (18)$$

Where $t_L$ is the loosening time.
The following formulas were used to calculate the rotational angle of the bolt. The total loosening period was divided into ten equal intervals, and the rotation angle was calculated for each segment.

$$\Delta t_l = \frac{t_l}{10} \quad (19)$$

$$\omega_i = \omega_{i-1} + \alpha_i \times \Delta t_l \quad (20)$$

$$\theta_i = \theta_{i-1} + \omega_i \times \Delta t_l \quad (21)$$

$$\Delta\theta = \sum_{i=1}^{10} \theta_i \quad (22)$$

Each time the bolt reaches the critical torque value, it rotates by an angle of $\Delta\theta$. The rotation of the screw in the loosening direction causes a decrease in the clamping force, leading to vibration-driven self-loosening. The decrease in clamping force per degree of rotation was experimentally determined through testing. The experiments were carried out using the ST-Wrench, which measures the torque–angle relationship, and the vibration test device, which records the variation of clamp load with torque. In these tests, the assembly rigidity is the same as the assembly rigidity in vibration tests. In the procedure, the bolts were first tightened to the desired clamping load and then unscrewed to determine the reduction in clamp load per degree of rotation. By combining the results from both devices, the clamp load-angle relation was obtained. A total of six different parameter combinations were tested, consisting of two different clamp lengths and three different clamping loads. Three repetitions were performed for each combination, resulting in a total of 18 tests. The resulting clamping load–angle relation of the tests is shown in Figure 3.

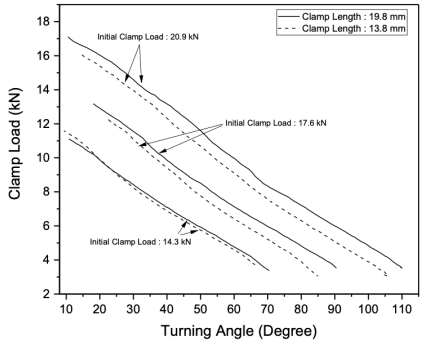


**Figure 3.** Clamping Load–Angle Relation of the Loosening Tests

Clamp load decrease per 1 degree of rotation is calculated with this formula:

$$\Delta F = \frac{\Delta\theta}{\phi^*} \tag{23}$$

Where $\phi^*$ is the slope of the angle–clamp load graph in Figure 3, and $\Delta F$ is the clamp load drop per 1 degree of rotation.

### *2.3. Experimental Analysis*

Experimental tests were conducted using the Vibration Master J160 Junker test device shown in Figure 4. M8 DIN 933 bolts and DIN 934 nuts were used. The coatings of the bolts and nuts were chosen as KL100 with a VH301 top coat. The friction coefficient range was measured between 0.09 and 0.14.



**Figure 4.** Vibration Master J160 Junker Test Device

As shown in Table 1, eight different test variations were defined with two variables of three parameters: transverse displacement, clamping length, and clamping force. Transverse displacement values of 0.3 mm and 0.4 mm, clamping lengths of 13.8 mm and 19.8 mm, and clamping forces of 14.3 kN and 17.6 kN were selected. A total of 24 tests were performed, consisting of three repetitions for each of the eight parameter combinations.

**Table 1.** Variations Used for Junker Vibration Test

| Test Variations [Var.] | Transverse Displacement [mm] | Clamp Load [kN] | Clamp Length [mm] |
|---|---|---|---|
| 1 | 0.3 | 17.6 | 19.8 |
| 2 | 0.3 | 17.6 | 13.8 |
| 3 | 0.3 | 14.3 | 19.8 |
| 4 | 0.3 | 14.3 | 13.8 |
| 5 | 0.4 | 17.6 | 19.8 |
| 6 | 0.4 | 17.6 | 13.8 |
| 7 | 0.4 | 14.3 | 19.8 |
| 8 | 0.4 | 14.3 | 13.8 |

## 3. Results

The analytical model developed in this study was validated through Junker vibration tests conducted under various clamping forces and displacement amplitudes. M8 × 1.25 DIN 933 bolts and DIN 934 nuts with KL100 / VH301 GZ coatings were used.

Figures 5 and 6 represent the comparison between experimental and analytically calculated results for clamping force reduction during transverse vibration at displacement amplitudes of 0.3 mm and 0.4 mm, respectively. In both cases, the analytical predictions successfully replicate the general trend of the experimental data, showing a rapid initial drop in clamp load followed by a more gradual decline toward stabilization.

For the 0.3 mm transverse-displacement condition (Figure 5a and 5b), the analytical model shows close agreement with the experimental curves for all parameter variations, with the maximum difference between predicted and mea-

sured loosening-rate values (kN/cycle) remaining within about ±10 %. In Figure 5a, which presents Variations 1 and 2, both analytical and experimental curves follow nearly parallel trends throughout the vibration cycles. Variation 1, corresponding to the higher clamping load (17.6 kN) and longer clamping length (19.8 mm), shows the smallest deviation, confirming that the model accurately represents the slower loosening rate caused by increased joint stiffness and preload. Variation 2, with a shorter clamping length (13.8 mm) but the same preload, exhibits a slightly faster clamp-load reduction, which is also well captured by the model. Figure 5b includes Variations 3 and 4 under the lower preload (14.3 kN) condition, where both experimental and analytical results indicate a more rapid loss of clamping force. Variation 3 loosens more slowly than Variation 4, again showing that higher stiffness improves vibration resistance.

For the 0.4 mm transverse-displacement condition (Figure 6a and 6b), both analytical and experimental results show a more pronounced decrease in clamping force with increasing vibration cycles, confirming that greater displacement amplitude intensifies slip at the contact interfaces. In Figure 6a, which includes Variation 5 and Variation 6, the analytical and experimental trends exhibit similar overall shapes, though the analytical model slightly overestimates the remaining clamp load after about 150 cycles. Variation 5, characterized by higher preload (17.6 kN) and longer clamp length (19.8 mm), maintains the slowest loosening rate, whereas Variation 6, with a shorter clamp length (13.8 mm), demonstrates a faster decay in clamp force. In Figure 6b, corresponding to Variation 7 and Variation 8 with lower preload (14.3 kN), both sets of results show a steeper reduction in clamping force, consistent with higher energy release and greater slip per cycle. While the analytical predictions follow the general trend, they slightly over-predict the remaining clamping load at later cycles. This difference can be explained by neglected nonlinear effects such as dynamic friction changes and small surface slips between contact areas, which are not fully represented in the one-dimensional analytical model.

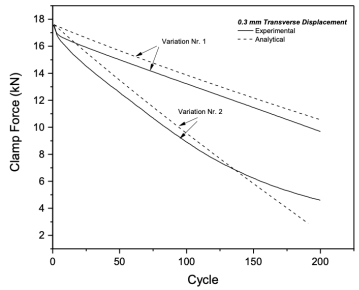


(a)

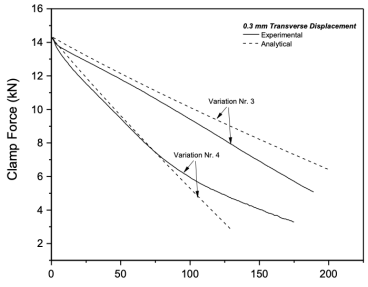


(b)

**Figure 5.** Experimental and Analytical Test Results for 0.3 mm Displacement for variation numbers (a) 1- 2 and (b) 3-4



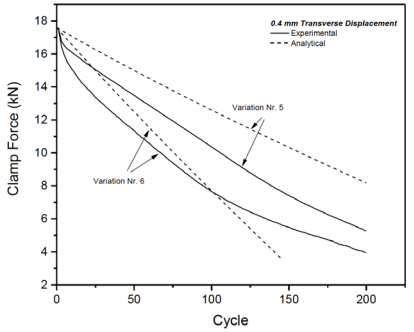


(a)

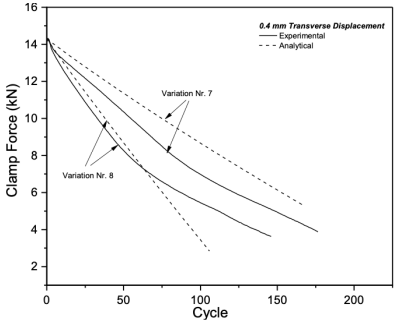


(b)

**Figure 6:** Experimental and Analytical Test Results for 0.4 mm Displacement for variation numbers (a) 5- 6 and (b) 7-8

Figure 7 presents the comparison between the calculated and experimentally measured loosening rates for all variations of the studied parameters. The results show a reasonable correlation between the analytical model and the experimental data, with most data points clustered around the unity line (Calc. LR / Exp. LR = 1), indicating well-correlated predictive accuracy. The deviations range from 1.2 % to 52.2 %, with an average deviation of 19.7 %.

The model demonstrates particularly good agreement for low and medium loosening rates (0.03–0.07 kN/cycle), where the ratio remains close to unity, validating the reliability of the energy-equilibrium formulation in this regime. Slight over-predictions are observed at higher loosening rates (> 0.07 kN/cycle), which are primarily associated with high-displacement (0.4 mm) and low clamping load (14.3 kN) conditions. This deviation can be attributed to the nonlinear slip behaviour and dynamic friction variation that are not fully captured in the simplified 1-D analytical formulation.

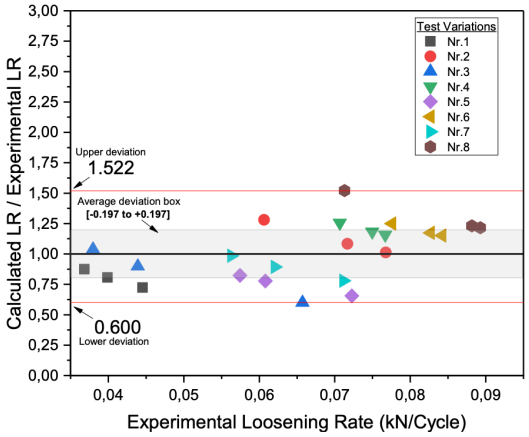


**Figure 7:** Accuracy of the Calculated Loosening Rate with respect to the Experimental Loosening Rate

## 4. Discussion and Conclusion

The presented results indicate that the adopted analytical model can accurately predict the loosening behaviour of bolted joints under transverse vibration. The comparison between the analytical calculations and the experimental Junker test results demonstrated reasonable agreement for different clamping forces, clamping lengths, and displacement amplitudes. The average deviation was approximately 19.7%, which is reasonable for preliminary design and analysis purposes.

The developed model reflects the influence of key parameters such as preload, clamp length, and displacement amplitude. Higher preloads and longer clamping lengths were shown to reduce loosening, while larger vibration amplitudes increased the loosening rate. These trends are consistent with the physical mechanisms described in previous studies [5–8], confirming the reliability of the one-dimensional, energy-based approach.

The energy equilibrium method introduced in this study provides a practical means to estimate the bolt's rotation and loosening rate. The model assumes that when the critical torque is exceeded, all the stored torsional strain energy is instantly converted into kinetic energy. This assumption represents a fully elastic process, neglecting the portion of energy dissipated as heat through friction. Therefore, the observed deviations between the analytical and experimental results can partially be explained by this simplification.
Furthermore, the model uses a constant friction coefficient (within 0.09–0.14), while in reality, the friction coefficient may dynamically vary during vibration due to surface wear and micro-pitting. The absence of a dynamic friction model may contribute to the discrepancy between experimental and analytical outcomes, particularly at higher vibration amplitudes.

As expected, larger deviations were observed at higher loosening rates, which are associated with stronger dynamic effects, nonlinear contact behaviour, and possible limitations in the assumed energy conversion and friction conditions. Despite these effects, the general correlation between analytical predictions and experimental data remained reasonable across all test conditions.
The implementation of the model in an MS Excel–based calculator makes it accessible for engineers and technicians, even without advanced software or programming knowledge. The tool allows quick evaluation of loosening behaviour under different conditions, reducing the need for costly and time-consuming physical tests.

In conclusion, the proposed analytical model, supported by experimental validation, provides a simple yet effective method to predict the loosening rate of bolts under vibration. It offers a balance between accuracy and practicality, making it suitable for design and early testing stages in industrial applications. Future work will focus on applying the model to different bolt types and geometries, and on improving its accuracy by incorporating nonlinear friction effects. Overall, this study contributes to the development of safer, more reliable, and cost-effective bolted joint designs for automotive and other vibration-sensitive applications.

## 5. Acknowledge

The authors would like to thank Norm Fasteners for providing the laboratory facilities and technical support necessary to carry out the experimental studies.

## References

1 N. G. Pai & D. P. Hess (2002). Three-dimensional finite element analysis of threaded fastener loosening due to dynamic shear load. Engineering Failure Analysis, vol. 9, no. 4, pp. 383–402.

2 G. Junker (1969). New criteria for self-loosening of fasteners under vibration. SAE Technical Paper 690055.

3 N. G. Pai & D. P. Hess (2002). Experimental study of loosening of threaded fasteners due to dynamic shear loads. Journal of Sound and Vibration, vol. 253, no. 3, pp. 585–602.

4 G. Dinger & C. Friedrich (2011). Avoiding self-loosening failure of bolted joints with numerical assessment of local contact state. Engineering Failure Analysis, vol. 18, no. 8, pp. 2188–2200.

5 U. İnce & M. Güden (2021). An experimental and comparative study of the self-loosening of bolted joints under cyclic transverse loading. Sakarya University Journal of Science, vol. 25, no. 2, pp. 499–513.

6 S. A. Nassar & M. Housari (2007). Effect of thread and bearing friction coefficients on vibration-induced loosening of bolted joints. Proceedings of the ASME International Mechanical Engineering Congress and Exposition (IMECE), Seattle, WA, USA, pp. 1–10.

7 S. A. Nassar & X. Yang (2009). Mathematical modeling of vibration-induced loosening of bolted joints. Journal of Sound and Vibration, vol. 326, no. 3–5, pp. 713–729.

8 Y. Sun, H. Zhang, & J. Zhang (2020). Quantitative evaluation of bolt self-loosening under transverse vibration. Proceedings of the Institution of Mechanical Engineers, Part C: Journal of Mechanical Engineering Science, vol. 234, no. 24, pp. 4929–4942.

# COATING MATERIALS FOR ENHANCING PERFORMANCE OF COLD WORK STEEL TOOLS

*Cemile KAYIŞ*
*Ege Anıl DİLER*
*Hatice SANDALLI*
*Fuat Can AĞARER*

Academic Researhes in Engineering Sciences

# COATING MATERIALS FOR ENHANCING PERFORMANCE OF COLD WORK STEEL TOOLS

**Cemile Kayış[1] & Ege Anıl Diler[2] & Hatice Sandallı[3] & Fuat Can Ağarer[4]**

[1]Res. Asst., Eskisehir Technical University, Department of Mechanical Engineering, Eskişehir, Turkey, ORCID: 0000-0002-4401-2412
[2]Assoc. Prof. Dr., Ege University, Department of Mechanical Engineering, Izmir, Turkey, ORCID: 0000-0002-1667-5737
[3]MSc. Norm Fasteners Co., Izmir, Turkey, ORCID: 0000-0002-5550-8480
[4]B.Eng., Norm Fasteners Co., Izmir, Turkey, ORCID: 0000-0001-7219-7592

## 1. Introduction

In cold forming operations, tooling is subjected to significant loads, particularly at high deformation rates, leading to tool damage over time and eventual failure. This tool degradation not only necessitates tool replacement but also causes production halts, machine recalibration for new tools, and the scrapping of some produced parts (Dubar et al., 2005). The lifespan of tools fundamentally dictates manufacturing efficiency. A machine capable of producing 155 units per minute might only deliver 137 due to persistent tool failures (Raja and Sornakumar, 2014). This discrepancy highlights more than just lost output; it points to a critical cost centre. With specialized tools like forming punches making up a considerable part of the cost for each component, investing in their longevity becomes paramount for both maximizing throughput and controlling unit costs.

For the cold forming punches, punch life is determined by the initiation and progression of three primary mechanisms: plastic deformation, wear, and fracture. Consequently, the punch material must exhibit a combination of high strength, superior wear resistance, high hardness, a low coefficient of friction, and excellent toughness (Almeida et al., 2017). Forming punches are typically manufactured from high-speed tool steels, which provide the necessary high toughness to withstand impact loads. However, to further enhance their strength and hardness, these tools often undergo various surface treatments. While heat treatments are sometimes preferred, ceramic coatings applied to the tool steels are more commonly employed (Ashvita et al., 2024; Wand et al., 2025).

Ceramic materials impart high hardness and strength to the punch, while the steel substrate ensures that the punch retains its tough behaviour. Over time, numerous coating materials have been explored and developed to optimally achieve these desired properties.

Coating technology has advanced significantly to meet evolving industrial demands, leading to increasingly complex structures. Historically, this development can be categorized into four distinct periods. The first period saw the widespread adoption of simple single-layer ceramic coatings, with TiN coatings serving as a prime example. Despite being positioned as early developments, these types of coatings remain prevalent in the industry today; indeed, the present study aims to enhance the lifespan of punches currently utilizing TiN coatings. The second period of development commenced with the chemical modification of single-layer films. TiAlN coatings exemplify this stage, where modifications successfully led to improvements in various properties. For instance, the example provided demonstrates significant advancements for processes conducted at high temperatures. The third and fourth periods in coating material technology are, in a sense, intertwined. The third stage involved the development of multi-layered coatings, achieved by sequentially depositing layers of different materials. This approach not only leverages the properties of the two distinct materials used in the layers but also benefits from the resulting layer interfaces, which play a crucial role in enhancing structural properties. The fourth development period, representing what can be considered state-of-the-art coatings today, encompasses multi-layered coatings fabricated at the nanoscale. In some structures, nanocomposite coatings are also observed, where nanocrystalline particles are dispersed within a three-dimensional amorphous matrix. For multi-layered coatings, the TiN/CrN system serves as an illustrative example.

Therefore, the subsequent sections of this chapter investigate the essential contribution of ceramic coatings to improving the performance of cold work steel tools, such as AISI M2, in various manufacturing environments.

## 2. Ceramic Coatings

This section will introduce the various types of ceramic coatings commonly applied to cold work tool steels, detailing their deposition methods and the particular advantages they offer in a multitude of manufacturing applications.

### *2.1. TiN Coating*

Titanium stands out for its exceptional ability to adhere to steel substrates. Nitrogen, conversely, is well-known as a frequently utilized element in surface hardening processes. The combination of these two elements forms a ceramic coating with remarkably high hardness and sufficient adhesion to steel substrates. Consequently, TiN coatings remain among the oldest (Hilton et al. 1987; Hug et al., 1997) and one of the most widely used coating materials for high-speed tool steels, such as AISI M2 steel, today (Cerıtbınmez et al., 2025).

TiN coatings are applied to steel substrates using a wide array of deposition techniques, such as physical vapour deposition (PVD) and chemical vapour deposition (CVD). In a study by M. Dubar et al. (2005), the coating thickness, hardness, and coefficient of friction were reported for AISI M2 steel tools that had been TiN coated using both PVD and CVD methods. It was observed that the coefficient of friction was higher on surfaces coated via PVD. This was attributed to the thinner coating thickness achieved with the PVD method, which meant that residual surface scratch marks from manufacturing stages were not fully concealed. Conversely, with the CVD method, these marks were covered, and the coated surface appeared to be uniformly covered with small spherical particles.

Figure 1 presents SEM images of as-coated PVD and CVD TiN surfaces.

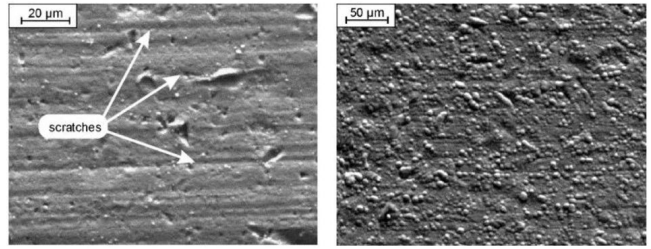


**Figure 1.** Surface aspect of TiN coating produced via (a) PVD and (b) CVD (Dubar et al., 2005)

The inability to achieve stabilization in the coefficient of friction after a certain number of manufactured parts stems from localized micro-welding. This welding occurs both between the workpiece and the tool, and between the tool surface and the coating surface. In PVD coatings, this welding progresses more rapidly due to the presence of scratches very close to the surface. Conversely, in CVD coatings, the main material adheres to the spherical particles of the coating at a later stage. Consequently, CVD coatings delay the friction distribution compared to PVD coatings. However, hardness values for both methods can be comparable (Dubar et al., 2005).

Nevertheless, other studies present differing observations. For example, a study by Hilton et al. (1987) found that TiN coatings produced via PVD exhibited higher hardness than PACVD coatings of equivalent thickness. Additionally, the grain size of PACVD-produced TiN coatings was determined to be 2500 Å, whereas the grain size from the sputtering method was measured at 500 Å. This disparity is likely attributable to differences in grain sizes resulting from the distinct production methods. These findings collectively indicate that the microstructure and, consequently, properties such as hardness, of TiN coatings can vary significantly depending on the specific production method employed.
When comparing TiN, Diamond-Like Carbon (DLC), and CrCN coatings applied to AISI M2 steel forming tools using the PVD method, TiN demonstrates a significant advantage. As illustrated in Figure 2, TiN emerges as a more favourable choice when considering both cost-effectiveness and service life compared to the other two coating types (Yousefi et al., 2021).

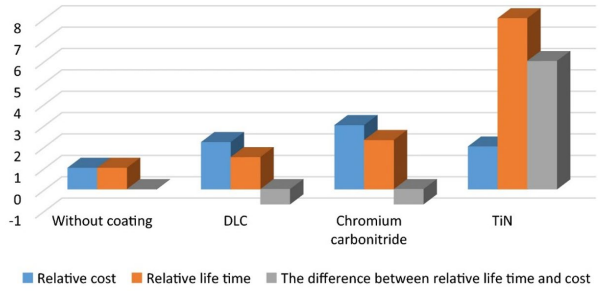


**Figure 2.** Relative criteria for DLC, CrCN, and TiN coatings (Yousefi et al., 2021)

It's feasible to considerably boost the hardness, wear resistance, and elastic modulus of TiN coatings, which are applied to AISI M2 high-speed steel using the PVD method, through the application of post-coating processes like Deep Cryogenic Treatment (DCT). These subsequent treatments enable a significant enhancement of the mechanical properties of the coating (Chiadikobi et al., 2024). It results from fundamental changes happening within the microstructure of the material. One key effect, especially in materials where it is present, is the nearly complete transformation of retained austenite to martensite. While TiN itself is not a steel, the substrate or interface layers might contain phases influenced by cryogenic temperatures. A more fully martensitic structure is inherently harder and more brittle, contributing to improved hardness and wear resistance. Cryogenic temperatures promote the precipitation of extremely fine, uniformly dispersed carbides or nitrides. Even in a coating like TiN, which is already a nitride, subtle atomic rearrangements and the formation of secondary, very fine phases can occur. These tiny precipitates act as obstacles to dislocation movement, significantly hardening the material and boosting its resistance to plastic deformation, which directly translates to better wear performance. DCT can help in redistributing and relieving some of the residual stresses within the coating. While PVD coatings often have beneficial compressive stresses, localized tensile stresses or non-uniform stress distributions can be detrimental. A more uniform and optimized stress state can lead to a more stable and mechanically robust coating. The extreme cold can subtly refine the atomic structure and improve the bonding between atoms. This can lead to a more compact and ordered lattice, which in turn increases the material's resistance to elastic deformation (higher elastic modulus) and makes it tougher against wear.

While more advanced methods and coating materials now exist for enhancing the wear resistance of AISI M2 high-speed tool steels beyond conventional PVD .

TiN, this combination retains its practical significance. The enduring appeal of PVD-applied TiN stems from its cost-effectiveness and the ability to significantly improve its tribological performance and elastic modulus through post-coating



treatments like Deep Cryogenic Treatment (DCT). This makes TiN a continuously viable and often preferred coating option for various industrial applications.

As a result, despite the emergence of newer advanced coatings, TiN remains a widely utilized and practical choice for enhancing the performance of highspeed tool steels due to its inherent hardness, sufficient adhesion, costeffectiveness, and the notable improvements in tribological properties achievable through post-coating treatments like DCT.

### *2.2. DLC Coating*

Another coating employed for AISI M2 steel tools is Diamond-Like Carbon (DLC). DLC coatings are amorphous films formed by arranging carbon atoms in a diamond-like structure. Primarily produced via PACVD or CVD from hydrocarbon gas sources, their classification depends on how closely their carbon arrangement resembles diamond and their hydrogen content. Hardness increases with a higher proportion of $sp^3$ hybridization and lower hydrogen content (Zerrin, 2014). DLC films develop significant internal stresses from their internal network structures, which accumulate as film thickness increases. This makes adhesion to the substrate challenging; DLC films over a particular thickness often delaminate. Poor adhesion can also stem from delayed DLC nucleation due to carbon diffusion into the steel. To counter this and enhance wear resistance by creating a hardness gradient, an interlayer is used as a mechanical buffer, improving DLC substrate adhesion.

Figure 3 shows the DLC coating deposited to AISI M2 steel. To promote adhesion to the surface of the M2 subtsrate, a Cr layer is used between the DLC coating and the steel substrate (Figure 3). As depicted in Figure 4, among the various coatings, DLC, TiN, TiAlN, and TiCN-deposited on a steel substrate, the lowest coefficient of friction is observed when utilizing the DLC coating (Banerji et al., 2014).

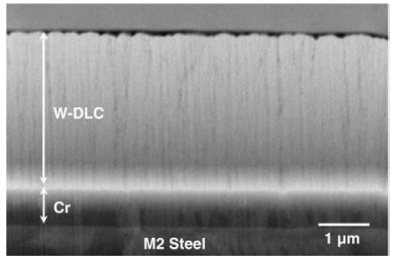


**Figure 3.** SEM image revealing the sequential deposition of a Cr interlayer and a subsequent W-DLC layer on an M2 steel substrate (Banerji et al., 2014)

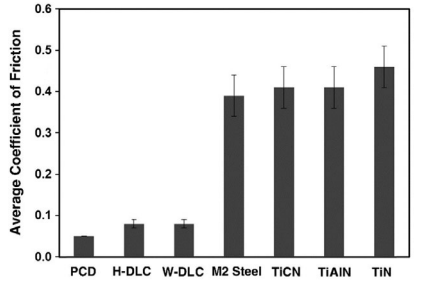


**Figure 4.** Comparison of coefficient of friction of M2 steel and DLC, TiN, TiAlN, and TiCN coatings (Banerji et al., 2014)

A lower coefficient of friction directly translates to less abrasive and adhesive wear between contacting surfaces. This significantly reduces material loss and surface degradation on both the coated component and any counter-surface it interacts with. Consequently, the service life of tools and components is substantially extended, leading to decreased replacement costs and reduced downtime. Less friction means less energy is dissipated as heat during relative motion. By minimizing friction, DLC coatings help to keep operating temperatures lower, thereby preserving the mechanical properties of the underlying substrate and coating, especially under high-load or high-speed conditions. In dry or minimally lubricated environments, metal-on-metal contact can lead to material transfer, a phenomenon known as galling, and eventually seizure, where components weld together. The extremely low friction and nonstick properties of DLC coatings effectively prevent these issues, ensuring smooth and reliable operation even under challenging conditions. Smoother, lower-friction interfaces contribute to a reduction in noise and vibration during operation. This can lead to quieter machinery and a higher quality of manufactured products, particularly in forming and moulding applications where surface finish is critical.

To enhance the performance of DLC coatings, the surfaces of M2 steel substrates are subjected to a nitriding treatment to establish superior adhesion between the coating and the substrate. As shown in Figure 5, the application of a nitride interlayer effectively creates a hardness gradient on the steel substrate. This gradient significantly improves the adhesion of the harder top DLC layer (Moreno-Bárcenas et al., 2019).

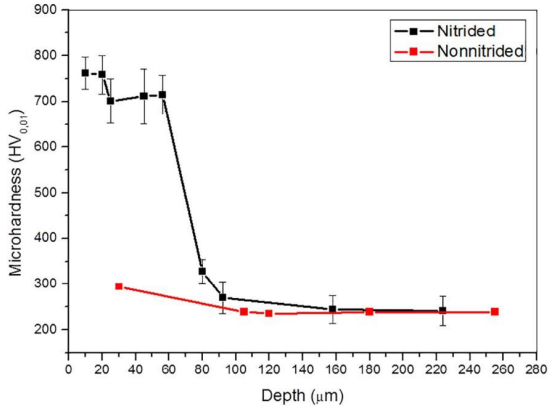


**Figure 5.** Microhardness of nitrided and non-nitrided M2 steel substrates (MorenoBárcenas et al., 2019)

Figures 6(a) and (b) present critical loads from scratch tests for DLC coatings, without and with a nitride interlayer respectively, deposited at various electrical powers. For all deposition powers, DLC coatings with an interlayer consistently withstand greater loads than those without. The presence of an interlayer substantially enhances the adhesion of the coating to the substrate.



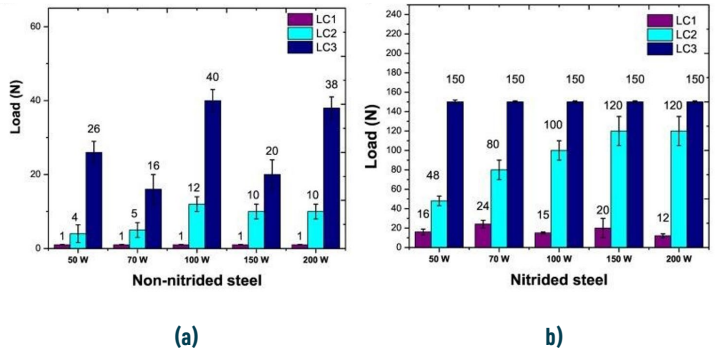


**Figure 6.** Load of the DLC coatings on the (a) non-nitrided and (b) nitrided M2 steel (LC: the maximum load-bearing capacity (the coating begins to peel from the substrate)), (LC1: the load causing cohesive failure, LC2: the load causing adhesive failure) (Moreno-Bárcenas et al., 2019)

Wang et al. (2021) investigated the adhesion capabilities of DLC coatings on M2 steel substrates, using titanium as an interlayer and comparing it against other parameters. They focused on the interface between the M2 steel (Fe layer) and the Ti interlayer, as well as the interface between the Ti interlayer and the DLC (C layer). For comparison, they also included a coating sample without an interlayer, directly examining the Fe and C layer interface. As anticipated, a higher energy requirement to separate two layers indicates stronger adhesion between them. The required energy for separation was ordered as follows: Ti/C > Fe/Ti > Fe/C. This suggests that the adhesion between the iron and carbon layers is the weakest. Furthermore, interfacial energy serves as a reliable index for assessing the adhesion ability of layers. Structures with a positive interfacial energy value between two layers are unstable, indicating a tendency to separate. Conversely, as the interfacial energy decreases, the stability and adhesion capabilities of the layers increase. Accordingly, the Fe/C structure exhibits the lowest adhesion, while the Ti/C structure possesses the highest.

Consequently, DLC coatings offer exceptional tribological benefits for AISI M2 steel tools, particularly their remarkably low friction coefficient, with their critical challenge of adhesion effectively addressed and optimized through the strategic use of interlayers such as chromium, titanium, or nitride.

### *2.3. CrAlN Coating*

The CrN structure is primarily distinguished by its corrosion resistance, largely due to the presence of chromium. Its superior wear and hardness properties are also key reasons for its widespread use as a tool coating material (Navinšek et al. 2017).

CrAlN coatings generally offer better tribological performance than CrN due to the addition of aluminium, which fundamentally changes the structure and behaviour of the coating. Aluminium promotes a more compact, nanocrystalline structure in CrAlN. This makes the coating harder and more resistant to cracks, as well as less porous, improving wear and corrosion resistance. Aluminium atoms substitute for chromium, creating lattice distortions that block dislocation movement. This significantly boosts the hardness of the coating, directly improving wear resistance (Lin et al, 2024). At elevated temperatures, aluminium forms a stable, self-lubricating aluminium oxide layer on the surface. This protective film enhances oxidation resistance, reduces friction, and maintains the integrity of the coating under heat, unlike the less robust oxides formed by CrN. The better oxidation resistance helps CrAlN retain its hardness and strength at higher temperatures, making it suitable for more demanding, high-heat applications (Polcar and Cavaleiro, 2011).

When CrN and CrAlN coatings are applied to AISI M2 steel using the PVD method, different processing parameters yield coatings with varied properties (Brizuela et al., 2005). As aluminium is added to the coating, its adhesion to the steel substrate tends to decrease. However, CrAlN coatings exhibit a lower coefficient of friction than CrN coatings.

The properties of the CrAlN structure vary with its aluminium content. Figure 7 illustrates the wear rates and coefficients of friction for CrAlN coatings with differing aluminium concentrations at various temperatures. Higher aluminium content generally leads to an increase in the friction coefficient. For instance, the coating with the highest aluminium concentration (CrAlN-3) consistently exhibits the highest friction values across all testing temperatures. This is primarily attributed to the increased formation of aluminium oxides ($Al_2O_3$) on the surface, which are inherently more abrasive and contribute to higher friction. Conversely, a greater aluminium presence significantly improves the wear resistance, resulting in lower wear rates. The same high-aluminium CrAlN-3 specimen, despite its higher friction, showed virtually no measurable wear at temperatures below 650°C. This enhanced durability is linked to the increased hardness imparted by the higher aluminium content, along with the protective nature of the aluminium oxides formed, which help the coating resist material loss even under demanding conditions (Sánchez-López et al., 2014).

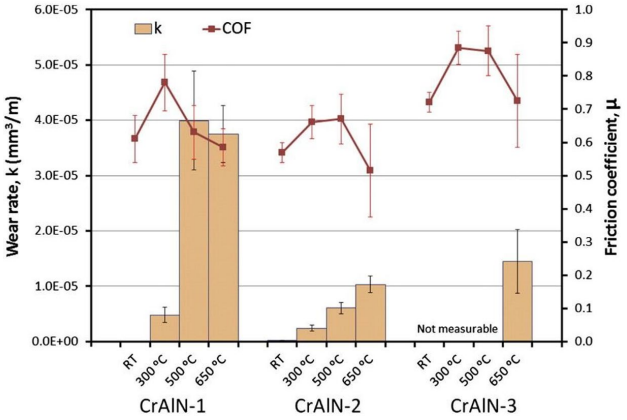


**Figure 7.** Tribological properties of CrAlN coatings (CrAlN-1: Al/(Cr+Al)=0.19, CrAlN-2: Al/(Cr+Al)=0.50, and CrAlN-3: Al/(Cr+Al)=0.68) (Sánchez-López et al., 2014)

When coating M2 high-speed steels with CrAlN via PVD, the plasma nitriding process applied to the M2 substrate, along with its specific parameters, significantly influences the overall performance of the coating. For instance, increasing the anode current during the nitriding treatment leads to a thicker nitrided layer. Consequently, as shown in Figure 8, both the application of plasma nitriding and an increased anode current enhance hardness, which in turn reduces the wear rate. The enhanced wear resistance and increased hardness observed in the CrAlN coatings are primarily attributed to the duplex treatment, specifically the plasma nitriding pretreatment at higher ion current densities. This process effectively creates a harder and thicker nitrided interlayer on the steel substrate. This interlayer, in turn, provides superior load-carrying capacity and significantly improves the adhesion of the subsequent CrAlN coating, collectively leading to the observed advancements in mechanical properties (Zhang et al., 2022).



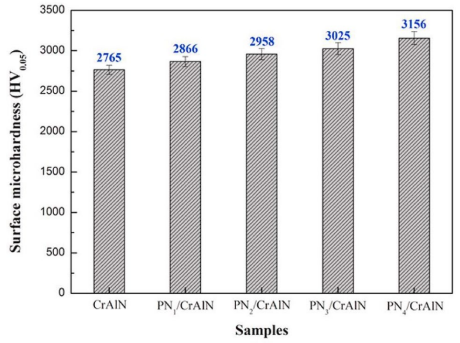


**Figure 8.** Effect of plasma nitriding and process parameter (anode current) on (a) hardness and (b) wear resistance of CrAlN coated-AISI M2 steel (Zhang et al., 2022)

Ultimately, CrAlN coatings present a highly effective solution for enhancing tool performance, with their superior tribological properties at elevated temperatures and improved wear resistance on steel substrates being finely tunable through precise control of aluminium content and judicious application of duplex treatments like plasma nitriding.

### *2.4. TiN/TiAlN Coating*

Multilayer coatings are increasingly popular due to their extended lifespan and superior wear resistance. Building on this, researches have explored the properties of TiN/(TiAlN) coatings, which combine the traditional, wellperforming TiN layer with an Al-modified TiAlN layer to enhance oxidation resistance. Figure 9 shows the $Ti_{0.45}Al_{0.55}N$ monolithic coating and $Ti_{0.45}Al_{0.55}N/Ti_{0.45}Al_{0.55}$ multilayer coating. For the $Ti_{0.45}Al_{0.55}N/Ti_{0.45}Al_{0.55}$ multilayer coating, the layer thicknesses shown in Figure 9(c) are lower than those presented in Figure 9(b). As seen in these figures, the monolithic coating clearly exhibits a columnar structure, whereas the $Ti_{0.45}Al_{0.55}N$ layers within the multilayers are characterized by a dense morphology, lacking distinct columnar grains (Shugurov and Kazachenok, 2018).

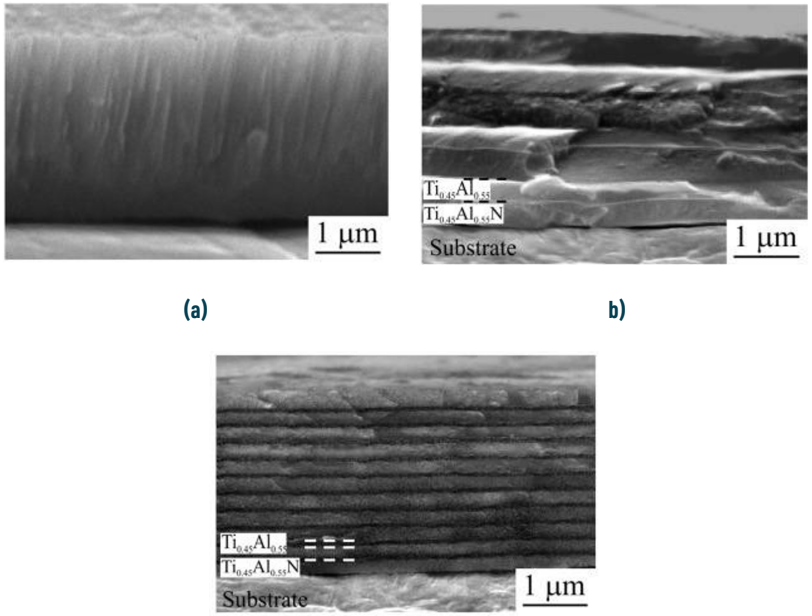


**Figure 9.** Cross-sectional SEM images of (a) monolithic $Ti_{0.45}Al_{0.55}N$ coating and (b) and (c) $Ti_{0.45}Al_{0.55}N/Ti_{0.45}Al_{0.55}$ multilayers coatings (Shugurov and Kazachenok, 2018)

For AISI M2 steel, investigations typically compare the characteristics of single-layer TiN coatings, single-layer TiAlN coatings, and multilayer TiN/(TiAlN) coatings. It is generally observed that adding aluminium to singlelayer coatings increases hardness. However, a notable reduction in the critical load from scratch tests is also observed for aluminium-containing coatings. This is attributed to the tendency of aluminium to reduce adhesion to the steel substrate. Exceeding a certain aluminium concentration in the coating significantly compromises adhesion strength. While PACVD can be used for deposition, PVD is more commonly employed for these coatings to maintain desired concentration limits. Notably, wear volume values are significantly lower for multilayer coatings compared to single-layer counterparts. This superior performance is believed to stem from the higher combined hardness and adhesion strength of the multilayer structure. Figure 10 illustrates the distinct damage behaviours of single-layer and multilayer coatings. Single-layer coatings typically show debris from wear around the scratch area (Figure 10(a)), whereas such debris is absent in multilayer coatings (Figure 10(b)). Furthermore, crosssectional analysis of the scratch path reveals that single-layer coatings exhibit circumferential spalling and widespread crack propagation (Figure 10(c)). In contrast, multilayer coatings show only a few localized cracks in the same direction, indicating less severe and more contained damage. This improved damage tolerance in multilayer coatings is primarily due to the disruption of stress propagation at the numerous interfaces, preventing continuous crack paths (Dong-Kak et al., 2003).



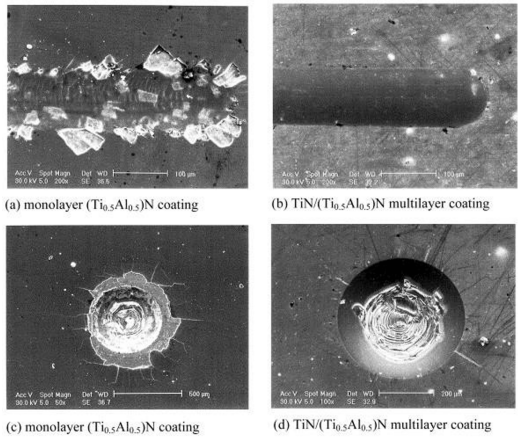


**Figure 10.** SEM images of the (a) monolayer $(Ti_{0.5}Al_{0.5})N$ and (b) multilayer $TiN/(Ti_{0.5}Al_{0.5})N$ coatings subjected to scratch tests and (a) monolayer $(Ti_{0.5}Al_{0.5})N$ and (b) multilayer $TiN/(Ti_{0.5}Al_{0.5})N$ coatings subjected to indentation tests (Dong-Kak et al., 2003).

In summary, TiN/TiAlN multilayer coatings significantly enhance the wear resistance and extend the lifespan of AISI M2 steel tools by combining the beneficial properties of TiN with the oxidation resistance of TiAlN, while their dense structure and numerous interfaces effectively mitigate crack propagation and improve overall adhesion compared to monolithic coatings.

### *2.5. TiN/CrN Coating*

TiN and CrN coatings are among the most frequently utilized PVD coatings. However, conventional single-layer coatings often fall short of current demands. Consequently, superlattice coatings, featuring multiple layers at the nanometer scale, have emerged. These multilayer coatings typically exhibit increased hardness compared to their single-layer counterparts. This enhancement is variously attributed to the Hall-Petch effect, differences in shear moduli, or internal stresses. Hardening is generally considered the primary driver for improved wear resistance. Yet, some researchers argue that an increased ratio of hardness to elastic modulus is responsible for this improvement. Intriguingly, certain studies (Steyer et al., 2008) have demonstrated that multilayer coatings can possess superior wear resistance even when compared to single-layer coatings that are inherently harder.

Figure 11 presents a graph illustrating the cumulative energy dissipated as a function of worn volume for these three distinct coatings, and indicates the superior wear resistance of the TiN/CrN multilayer coating compared to its monolithic TiN and CrN counterparts. This significant improvement is evident from its ability to withstand considerably higher cumulative dissipated energy before failure, directly supporting the conclusion that multilayer architectures effectively mitigate wear mechanisms by impeding crack propagation at their numerous interfaces (Mendibide et al., 2006).

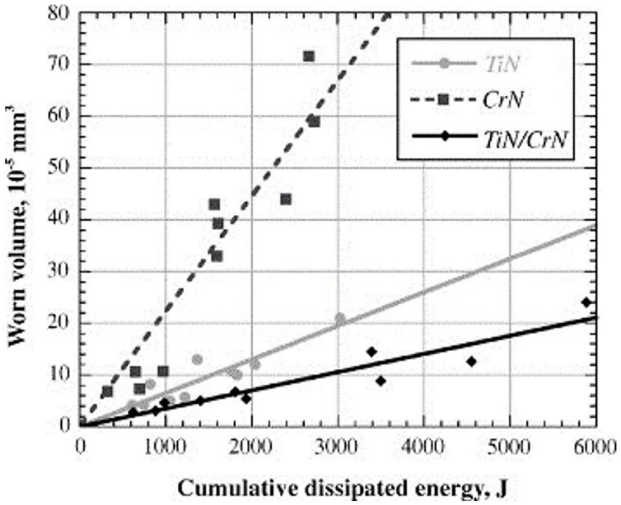


**Figure 11.** Relationship between worn volume and cumulative dissipated energy for the distinct coatings (Mendibide et al., 2006)

To elucidate how wear resistance is enhanced in TiN/CrN coatings, examining Figure 12 proves beneficial. Figure 12(a) illustrates the damage mechanism initiated in a TiN coating after a certain number of impact loads. Cracks initially form perpendicular to the surface but then change direction near the interface with the substrate, leading to spalling and detachment of the coating. Figure 12(b) further depicts the delamination experienced by the TiN coating as a result of this damage. However, as observed in Figure 12(c), in the TiN/CrN multilayer coating, cracks forming parallel to the interfaces are quite extensive but do not coalesce or propagate through the structure, thus preventing detachment. Additionally, these interface-parallel cracks in multilayer coatings are located at a greater distance from the substrate compared to those in single-layer coatings.



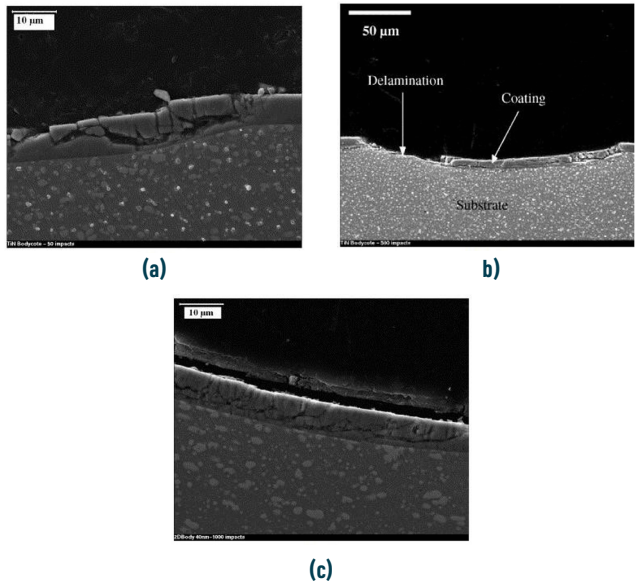


**Figure 12.** SEM images of cross-sections of (a) and (b) single-layer TiN and (c) multilayer TiN/CrN coatings after impact test (Mendibide et al., 2006)

PVD processes inherently induce significant compressive stresses within the coating structure. In single-layer coatings, the maximum compressive stress is concentrated near the coating-substrate interface. This stress generates strain in both parallel and perpendicular directions relative to the interface. The strain in the perpendicular direction, in particular, results in tensile stress along that axis (Figure 14(a)). Consequently, crack propagation tends to occur perpendicular to this tensile stress, in a plane parallel to the substrate-coating interface (Figure 14(b)). During tribological loading, crack initiation can begin at low compressive stress levels, with crack progression continuing until the stress becomes too high for further propagation. At this point, the crack begins to advance along the interface under the influence of tensile stress (Figure 14(c)). When these cracks coalesce, they lead to material detachment, resulting in the characteristic peeling failure (Figure 14(d)).

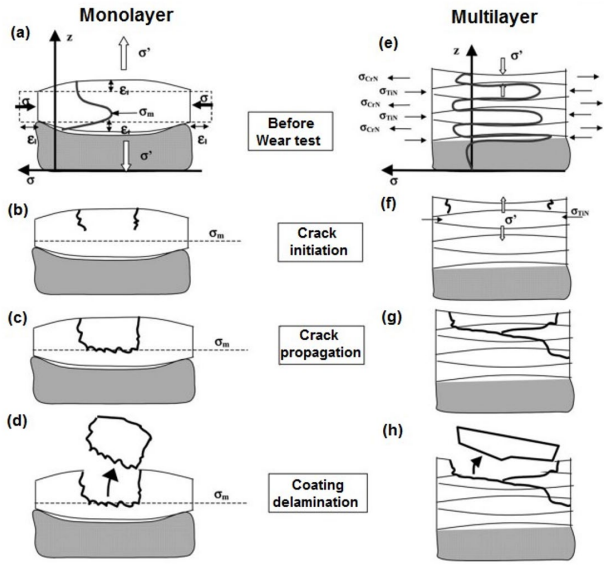


**Figure 14.** Wear model of monolayer coating ((a), (b), (c), (d)) and multilayer coatings ((e), (f), (g), (h)) (Mendibide et al., 2004)

For multilayered TiN/CrN coatings, while the entire coating remains under an overall compressive stress, individual layers experience different types of localized stresses. Given that TiN and CrN layers grow epitaxially, and TiN has a larger lattice parameter than CrN, each TiN/CrN interface results in the TiN layer being under compressive stress and the CrN layer under tensile stress (Figure 14(e)). This assumption effectively explains the differing crack propagation mechanisms observed in multilayer coatings. The TiN layers, which are under compressive stress parallel to the interface, also experience tensile stress perpendicular to the interface due to the same reasons observed in singlelayer coatings (Figure 14(f)). Conversely, the CrN layers are under tensile stress parallel to the interface, causing them to experience compressive stress perpendicular to the interface. Since cracks generally propagate perpendicular to the tensile stress axis, they tend to extend horizontally (parallel to the interface) within the TiN layers and vertically (perpendicular to the interface) within the CrN layers (Figure 14(g)). This results in crack deflections as they traverse between layers. Such deflections effectively lengthen the crack path, increasing resistance to wear, and consequently making peeling failure nearly impossible in these multilayer structures (Figure 14(h)).

As a result, TiN/CrN multilayer coatings significantly enhance wear resistance and extend service life by strategically deflecting crack propagation at their numerous interfaces, thereby preventing the catastrophic delamination common in conventional single-layer designs.

## 3. Conclusion

The persistent challenge of tool degradation in cold forming operations, manifesting as plastic deformation, wear, and fracture, highlights the critical need for advanced surface engineering solutions. As this chapter has demonstrated, enhancing the lifespan of cold forming tool steels is paramount for improving manufacturing efficiency, reducing costs,



and maintaining product quality. The exploration herein has covered a spectrum of coating materials and strategies, from foundational single-layer coatings to sophisticated nanostructured multilayers, each contributing uniquely to the overall performance envelope.

The examination commenced with TiN coatings, a long-standing choice in PVD applications for AISI M2 steels due to their excellent adhesion and hardness. While studies have revealed variations in their tribological behaviour depending on deposition method, with PVD sometimes presenting challenges related to surface topography and micro-welding, the fundamental efficacy of TiN remains undeniable. Crucially, the practical relevance of TiN coatings can be significantly extended through post-coating treatments. Deep Cryogenic Treatment (DCT), for instance, has been shown to induce beneficial microstructural transformations, such as the conversion of retained austenite and the precipitation of fine strengthening phases, alongside stress redistribution. These changes collectively elevate the hardness, wear resistance, and elastic modulus of the coating, affirming the continued viability of TiN as a costeffective solution in numerous industrial contexts, even when more advanced materials are available.

Diamond-Like Carbon (DLC) coatings offer a compelling alternative, particularly due to their remarkably low coefficient of friction. This attribute directly translates into substantial advantages: reduced wear, lower energy consumption, decreased heat generation, and effective prevention of galling and seizure. However, the inherent internal stresses of DLC films necessitate strategic approaches to ensure robust adhesion. The critical role of interlayers, such as chromium, and pre-treatment methods like plasma nitriding of the M2 steel substrate, in establishing a strong interfacial bond and promoting a beneficial hardness gradient was emphasized. These measures are crucial for unlocking the full potential of DLC in demanding forming applications.

Further exploration of surface solutions led to CrAlN coatings, which consistently outperform conventional CrN. The introduction of aluminium significantly refines the microstructure, promoting a denser, nanocrystalline arrangement and inducing solid solution hardening. A standout feature of CrAlN is its enhanced high-temperature performance, where it forms a stable, selflubricating aluminium oxide layer that markedly improves oxidation resistance and maintains low friction under thermal loads. This superior thermal stability positions CrAlN as an excellent candidate for applications experiencing significant heat generation.

By alternating layers of distinct materials, multilayer coatings, such as TiN/TiAlN and TiN/CrN, introduce a high density of interfaces that effectively impede crack propagation, a phenomenon akin to the Hall-Petch effect. This leads to remarkable improvements in fracture toughness and wear resistance, often surpassing those of single-layer counterparts, even at comparable total thicknesses. The detailed analysis of crack deflection mechanisms in TiN/CrN multilayers, governed by localized stress distributions at the epitaxial interfaces, provided clear evidence of their enhanced damage tolerance and near immunity to catastrophic peeling failure.

In conclusion, the selection of an optimal coating for cold work tool steels is a multifaceted decision. While foundational coatings like TiN remain relevant, especially when enhanced by targeted post-treatments, the continuous advancements in materials science offer increasingly sophisticated solutions. DLC coatings provide unparalleled friction reduction, CrAlN excels in hightemperature and abrasive environments, and multilayer TiN/TiAlN and TiN/CrN coatings, designs present a robust strategy for combining synergistic properties and managing crack propagation. The data consistently emphasizes that a deep understanding of the wear mechanisms, the specific demands of the forming process, and the interplay between coating properties and substrate pre-treatment is paramount. As manufacturing continues to push boundaries, the ongoing innovation in surface engineering of cold work steel tools will remain central to achieving higher productivity, extended tool life, and superior product quality.

## References


Almeida, E. A. S., Costa, C. E., Milan, J. C. G., Krelling, A. P. and Galiotto, A. (2017). Investigation of borided layerscontribution on the wear resistance and adhesion of TiN coatings. Revista Matéria, 22(1), 1–11. https://doi.org/10.1590/S1517-707620170001.0119.

Ashvita, A. J., Patnaik, L., Maity, S. R. and Kumar, S. (2024). Comparative study on surface modification of heat-treated hot work tool steel using plasma nitriding and thin film deposition technique. Materials Today: Proceedings. In press. https://doi.org/10.1016/j.matpr.2024.05.119.

Banerji, A., Bhowmick, S. and Alpas, A. T. (2014). High temperature tribological behavior of W containing diamond-like carbon (DLC) coating against titanium alloys. Surface and Coatings Technology, 241, 93–104. https://doi.org/10.1016/j.surfcoat.2013.10.075.

Brizuela, M., Garcia-Luis, A., Braceras, I., Oñate, J. I., Sánchez-López, J. C., Martínez-Martínez, D., López-Cartes, C. and Fernández, A. (2005). Magnetron sputtering of Cr(Al)N coatings: Mechanical and tribological study. Surface and Coatings Technology, 200(1–4), 192–197. https://doi.org/10.1016/j.surfcoat.2005.02.105.

Cerıtbınmez, F., Çakir, F. H. and Parım, B. (2025). Enhancing wear resistance of TiNcoated 1.3343 high-speed steel punches through deep cryogenic treatment and tempering. Journal of Central South University, 32, 350–362. https://doi.org/10.1007/s11771-025-5893-7.

Chiadikobi, C. I., Thornton, R., Statharas, D. and Weston, D. P. (2024). The effects of deep cryogenic treatment on PVD-TiN coated AISI M2 high speed steel. Surface and Coatings Technology, 493(2), 131248. https://doi.org/10.1016/j.surfcoat.2024.131248.

Dong-Kak, L., Seung-Hoon, L. and Jung-Joong, l. (2003). The structure and mechanical properties of multilayer TiNy(-Ti Al 0.5 0.5)N coatings deposited by plasma enhanced chemical vapor deposition. Surface and Coatings Technology, 169–170, 433–437. https://doi.org/10.1016/S02578972(03)00184-1.

Dubar, M., Dubois, A. and Dubari L. (2005). Wear analysis of tools in cold forging: PVD versus CVD TiN coatings. Wear, 259(7–12), 1109–1116. https://doi.org/10.1016/j.wear.2005.01.006.

Hilton, M. R., Vandentop, G. J., Salmeron, M. and Somorjai, G. A. (1987). TiN coatings on M2 steel produced by plasma-assisted chemical vapor deposition, Thin Solid Films, 154(1–2), 377–386. https://doi.org/10.1016/0040-6090(87)90380-4.

Huq, M. Z. and Celis, J. P. (1997). Reproducibility of friction and wear results in ballon-disc unidirectional sliding tests of TiN-alumina pairings. Wear, 212(2), 151–159. https://doi.org/10.1016/S0043-1648(97)00167-1

Lin, R., Sun, S., You, B., Dong, T., Sui, Y. and Wei, S. (2024). Evaluation of wear resistance of CrN, CrAlN, and TiAlN coatings deposited by multi-arc ion plating on spinning die of Cr12MoV. Materials Research Express, 11(9), 096402. https://doi.org/10.1088/2053-1591/ad7350.

Mendibide, C., Fontaine, J., Steyer, P. and Esnouf, C. (2004). Dry sliding wear model of nanometer scale multilayered TiN/CrN PVD hard coatings. Tribology Letters 17, 779–789. https://doi.org/10.1007/s11249-004-8086-9.

Mendibide, C., Steyer, P., Fontaine, J. and P. Goudeau. (2006). Improvement of the tribological behaviour of PVD nanostratified TiN/CrN coatings - An explanation. Surface and Coatings Technology, 201(7), 4119–4124. https://doi.org/10.1016/j.surfcoat.2006.08.013.

Moreno-Bárcenas, A., Alvarado-Orozco, J. M. Carmona, J. M. G., MondragonRodriguez, G. C., Gonzalez-Hernandez, J. and Garcia-Garcia, A. (2019). Synergistic effect of plasma nitriding and bias voltage on the adhesion of diamond-like carbon coatings on M2 steel by PECVD. Surface and Coatings Technology, 374, 327–337. https://doi.org/10.1016/j.surfcoat.2019.06.014.

Navinšek, B., Panjan, P. and Milošev, I. (1997). Industrial applications of CrN (PVD) coatings, deposited at high and low temperatures. Surface and Coatings Technology, 97(1–3), 182–191. https://doi.org/10.1016/S02578972(97)00393-9.

Ormanova, M., Kotlarski, G., Dechev, D., Ivanov, N., Stoyanov, B. and Valkov, S. (2023). Duplex surface modification of M2 high-speed steel. Coatings, 14, 798. https://doi.org/10.3390/coatings14070798.

Polcar, T. and Cavaleiro, A. (2011). High temperature properties of CrAlN, CrAlSiN and AlCrSiN coatings – Structure and oxidation. Materials Chemistry and Physics, 129(1–2), 195–201. https://doi.org/10.1016/j.matchemphys.2011.03.078.
Raja, V. and Sornakumar, T. (2014). Punch life improvement in cold forging of nut.

International Journal of Engineering Research & Technology (IJERT), 3(11), 838–842. https://www.ijert.org/punch-life-improvement-in-coldforging-of-nut.

Sánchez-López, J. C., Contreras, A., Domínguez-Meister, S., García-Luis, A. and Brizuela, M. (2014). Tribological behaviour at high temperature of hard CrAlN coatings doped with Y or Zr. Thin Solid Films, 550, 413–420. https://doi.org/10.1016/j.tsf.2013.10.041.

Shugurov, A. R. and Kazachenok, M. S. (2018). Mechanical properties and tribological behavior of magnetron sputtered TiAlN/TiAl multilayer coatings. Surface and Coatings Technology, 353, 254–262. https://doi.org/10.1016/j.surfcoat.2018.09.001.

Steyer, P., Mege, A., Pech, D., Mendibide, C., Fontaine, J., Pierson, J. -F., Esnouf, C. and Goudeau, P. (2008). Influence of the nanostructuration of PVD hard TiN-based films on the durability of coated steel. Surface and Coatings Technology, 202(11), 2268–2277. https://doi.org/10.1016/j.surfcoat.2007.08.073.

Wang, K., Zhou, H., Zhang, K., Liu, X., Feng, X., Zhang, Y., Chen, G. and Zheng, Y. (2021). Effects of Ti interlayer on adhesion property of DLC films: A first principle study, Diamond and Related Materials, 111, 108188. https://doi.org/10.1016/j.diamond.2020.108188.

Wang, X.X., Wang, Y.H., Ling, Z.C.,. Yuan Z.P., Shi, J.J., Qin, J., Sun, H.W., Pan, K.M., Geng, Z.M., Ma, H.L., Yand Z.J., Liu, S., Wu, Y.M. and Peng, Y. (2025). Strategies for superhard tool coating materials: focus on preparation methods and properties. Journal of Iron and Steel Research International. In press. https://doi.org/10.1007/s42243-025-01448-x.

Yousefi, M., Baghshahi, S. and Kerahroodi, M. S. A. (2021). Effect of titanium nitride, diamond-like carbon and chromium carbonitride coatings on the life time of an AISI M2 Steel punch forming tool. Journal of Bio- and TriboCorrosion, 7, 50. https://doi.org/10.1007/s40735-021-00483-x.

Zerrin T. (2014). Elmas benzeri karbon ince filmlerin hazırlanması ve karakterizasyonu / Preparation and characterization of diamond-like carbon thin films. Hacettepe Üniversitesi, Fen Bilimleri Enstitüsü, Fizik Mühendisliği Ana Bilim Dalı, Ankara.

Zhang, X., Tian, X., Gong, C., Liu, X., Li, J., Zhu, J. and Lin, H. (2022). Effect of plasma nitriding ion current density on tribological properties of composite CrAlN coatings. Ceramics International, 48(3), 3954-3962. https://doi.org/10.1016/j.ceramint.2021.10.182.

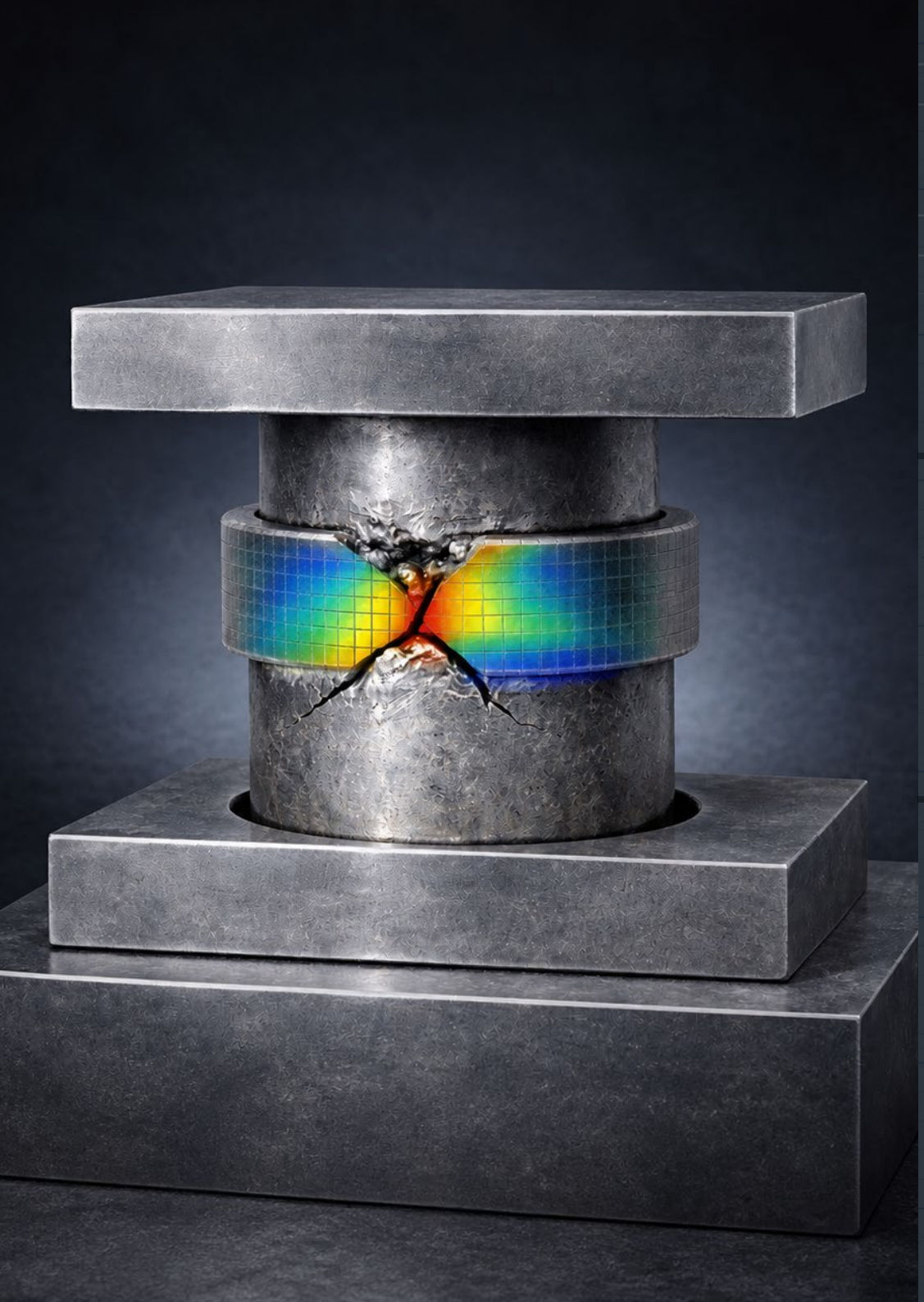

# DETERMINATION OF CRITICAL DAMAGE LIMIT IN MEDIUM-RATE CARBON STEELS BY EXPERIMENTAL AND NUMERICAL METHODS

*Burak Berk ARINCI*
*Hüdayim BAŞAK*
*Hatice SANDALLI YILDIZ*

Multiscale Science and Engineering

# DETERMINATION OF CRITICAL DAMAGE LIMIT IN MEDIUM-RATE CARBON STEELS BY EXPERIMENTAL AND NUMERICAL METHODS

**Burak Berk ARINCI[1], Hüdayim BAŞAK[2], Hatice SANDALLI YILDIZ[1]**

Received: 25 February 2025 / Revised: 2 April 2025 / Accepted: 7 April 2025


## Abstract

Indirect gains and verification obtained by using analysis programs in the manufacturing industry are becoming more critical in terms of competition and finance day by day, together with changing economic policies. Since medium-carbon steels exhibit more ductile behavior than high-carbon steels, obtaining crack-damage formation with a standard compression test is more challenging. In this study, the critical damage limit of C45E steel is examined in the cold forging process, and the essential determination of damage limit with numerical methods and verification with experimental methods are discussed. Compression tests are performed with the determined center flange test geometry to observe the damage behavior better, and load-displacement graphs of C45E steel are obtained. The load-displacement curve of the material is used to determine the friction coefficient of the experimental environment. Numerical analyses are performed with different Coulomb coefficient values , and the load-displacement graphs are compared. By examining the load-displacement graphs of the numerical and experimental studies, the friction coefficient value of the experimental environment was determined, and the Cockroft Latham critical damage value was determined as 0,42 for C45E steel with a low sensitivity element number. The numerical analysis examined the effect of the element number on the damage value. The compression test analysis was repeated by increasing the element number, and the critical damage limit of C45E steel was determined as 0,47.

**Keywords:** Critical damage, Steel, Cold forging, Cockroft Latham

## 1. Introduction

Developing technologies and the competition brought by the economy cause mandatory development in engineering. Companies need to be able to detect problems encountered in production in advance. It is aimed to prevent issues that can be detected in advance by taking precautions in the design phase.

In the cold forging industry, the limit of foreseeability is the cracks and/or fractures formed on the material. Determining the critical damage coefficient of the steel to be shaped allows for the necessary precautions to be taken before the forging process and design studies to reduce the damage limit on the product. In the cold-forming process, forging-related damages in the steel material are difficult to prevent. This problem leads to time loss and high costs.

As the carbon content decreases, it becomes difficult to determine the critical damage limit of steels with traditional methods. This is because the material's malleability increases with the decrease in carbon content, making it challenging to observe crack or fracture behaviors. Compression testing is essential to determine the critical damage limit of C45E steel with a medium carbon content to prevent damage problems encountered in the cold-forming process. Some damage models have been used to determine the critical damage limit of materials. In numerical analyses performed using these damage models, the critical damage limit value determined by experimental methods is used. Thus, the crack behavior that may occur in the material can be determined before starting the production process. Still, if the critical damage limit of the material does not exist, such a risk cannot be determined in the numerical analysis. One of the most common of these models is the Cockroft-Latham damage model. This model is preferred because it focuses on the maximum principle stress that usually increases when crack formations are observed in the cold forging process.

Studies on critical damage limits are separated in terms of damage criterion, material, and process used in the literature. Studies on non-steel materials have mainly been conducted on aluminum, magnesium, and copper alloys. In studies on ductile fracture with steel materials, medium and high-carbon steels were preferred.

Predicting and analyzing ductile fractures in steel production processes is very important. Ductile fracture is a phenomenon that occurs as a result of the coalescence of microstructural damages during the plastic deformation phase of the material. Studies on the prediction of this phenomenon are generally examined under three main headings. The first of these is micro-based damage mechanics based on the nucleation of voids and their growth and coalescence when subjected to stress, and the first studies on these criteria were included in the literature as the McClintock criterion [1] and the Rice and Tracey criterion [2]. When subjected to stress and damage formation, these criteria are based on the growth and coalescence of cylindrical and spherical voids within the material. Although micro-based damage mechanics models have various advantages, determining material parameters is not practical. These models prioritize hydrostatic stress by considering the voids within the material while neglecting shear stresses. The second group of studies on ductile fracture has been addressed as experimental or semi-experimental approaches. In this group of studies, a scalar function is defined, and it is predicted that ductile fracture will occur when a unitless coefficient exceeds a specific critical limit due to the function depending on the stresses. Being dependent on a scalar function allows it to be easily added to numerical studies. In the second group, a scalar function commonly includes the stress tensor and practical plastic strain components. The Cockroft Latham [3] damage model proposes a function depending on the maximum principal stress and effective plastic strain. The third model, continuum fracture mechanics, formulates irreversible microstructural weakening in the light of a mathematical structure representing an internal variable coupled with deformation. The basis of the approach was laid by Kachanov [4] and Rabotnov [5]. The concept of effective stress was presented for metal fractures due to creep. Lemaitre [6] is a frequently used continuum damage mechanics model. Continuum damage mechanics have been developed to include anisotropy, thermal effects, and finite deformation [7].

In this study, the critical damage limit of C45E steel is examined in the cold forging process, and the essential determination of damage limit with numerical methods and verification with experimental methods are discussed. Compression tests are performed with the determined center flange test geometry to observe the damage behavior better, and load-displacement graphs of C45E steel are obtained. The load-displacement curve of the material is used to determine the friction coefficient of the experimental environment. Numerical analyses are performed with different Coulomb coefficient values , and the load-displacement graphs are compared.

## 2. Material and Method

The experiments in this study were carried out with the Galdabini Quasar 200 testing machine with a maximum tensile and compressive force of 200 KN (Fig. 1). This device includes jaws that allow fixtures and molds of various geometries to be easily adapted to the device.


**Fig. 1** Galdabini Quasar 200 test machine

In the traditional compression test, C45E (0.46% C) steel material with medium carbon content was preferred to achieve relatively more straightforward damage behavior than steels with low carbon content. Experimental compression tests were performed with Ø10 mm C45E material from VoestAlpine company, which was given a material composition certificate in Table 1. "SA*" means sample analysis and "DR*" means data report. Material flow curves were created using the component ratios in the material composition certificate. The shaping curves of the material characteristic formed according to different strain rates under load at 25°C temperature were transferred to the Simufact program.

**Table 1.** C45E steel chemical composition

| SA* | C | Si | Mn | P | S | Cr | Ni | Cu | Al | Ti | Mo | V | W |
|---|---|---|---|---|---|---|---|---|---|---|---|---|---|
| DR* | 0,4613 | 0,0669 | 0,6572 | 0,012 | 0,0234 | 0,0236 | 0,0148 | 0,0147 | 0,036 | 0,0004 | 0,0042 | 0,0007 | 0 |
| SA* | Sn | B | N | Nb | O | As | Sb | Zr | Pb | Co | Ca | Ta | H[ppm] |
| DR* | 0,0002 | 0 | 0,0037 | 0 | 0,002 | 0,0029 | 0,0001 | 0 | 0,0001 | 0,0025 | 0,0016 | 0 | 0 |

In the determination of the geometry of the sample to be used in the compression test by processing it from Ø10 mm C45E steel material on a CNC lathe, it was observed that the most commonly used geometries in the literature review were straight cylindrical, angled cylindrical and flanged cylindrical samples. Since it is difficult to estimate the location of the crack that will occur on the geometry in the compression test in straight cylindrical or angled samples, compression tests were carried out with the central flanged cylindrical sample whose geometry is given in Fig. 2. In the compression test, the damage coefficient that will increase in the regions below and above the flanges in the specific central flanged sample makes it easier to observe the crack as it occurs.

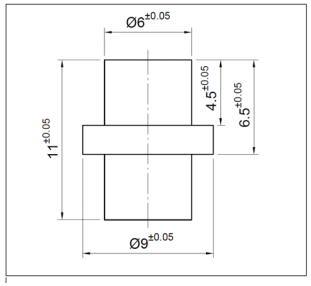


**Fig. 2** Specimen geometry used in compression test



The surface roughness values measured radially from the flange on the sample not subjected to compression test and the samples numbered 10, 11, and 12 subjected to compression test with the Mitutoyo SJ-400 surface roughness device are given in Table 2.

**Table 2.** Surface roughness values taken from samples

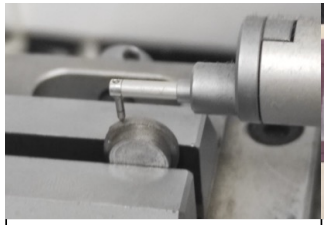

| Specimen Status | Ra (µm) | Rz(µm) |
|---|---|---|
| Not compressed | 0,65 | 4,2 |
| Compressed specimen 10 | 1,32 | 8,5 |
| Compressed specimen 11 | 1,03 | 6,6 |
| Compressed specimen 12 | 1,55 | 7,7 |

## 3. Damage Model Selection

In fracture mechanics, an accumulated plastic work limit is considered. Since it is known that different stress states (Eq.1 and Eq.2) affect the damage to the material, some equations have been proposed to determine the limits of isotropic materials under multiaxial loads.

$$\sigma_{VM} = \sqrt{\frac{(\sigma_1-\sigma_2)^2+(\sigma_2-\sigma_3)^2+(\sigma_3-\sigma_1)^2}{2}} \quad 1)$$

$$\sigma_H = \frac{\sigma_1+\sigma_2+\sigma_3}{3} \quad 2)$$

The Freudenthal damage model in Eq. 3 suggests a function that depends on the equivalent stress and effective strain. Since it uses only the von Mises stress, its predictions remain superficial compared to other damage models. $\sigma_{eq}$ represents the von Mises stress, $\bar{\varepsilon}$ represents the effective strain, $\bar{\varepsilon_f}$ represents the effective strain at the moment when ductile fracture occurs.

$$\int_0^{\bar{\varepsilon_f}} \sigma_{eq} d\bar{\varepsilon} = C_1(Freudenhtal) \quad 3)$$

The Cockroft Latham [3] damage model in Eq.4 suggests a function depending on the tensile stress and effective strain. This model, which is widely used, is preferred because of its simplicity, accurate results in the relevant process, and fast approach. $\sigma_{max}$ represent maximum principle stress. The Cockroft-Latham damage model is based on a scalar function and is generally used in mass form.

$$\int_0^{\bar{\varepsilon}_f} \frac{\sigma_{max}}{\sigma_{eq}} d\bar{\varepsilon} = C_2(Cockroft\ Latham) \quad 4)$$

The McClintock damage model [1] in Eq. 5 is the first model based on void growth. It assumes that there are round or elliptical voids in the material and that these voids grow and merge under load. The symbol n is the strain hardening coefficient in the Ludwig-Holomon stress-strain relationship. $\sigma_a$ ve $\sigma_b$ are the principal stresses in the direction of the largest and smallest gap deformation.

$$\int_0^{\bar{\varepsilon}_f} \left[\frac{\sqrt{3}}{2(1-n)} \sinh\left(\frac{\sqrt{3}(1-n)}{2} \frac{\sigma_a+\sigma_b}{\sigma_{eq}}\right) + \frac{3}{4}\frac{\sigma_a-\sigma_b}{\sigma_{eq}}\right] d\bar{\varepsilon} = C_3(Mcclinctock) \quad 5)$$

The Rice and Tracey damage model [2] given in Eq.6 developed a model based on void growth like the McClintock damage model. In this model, the propagation speed of microcracks and voids formed in the material varies depending on the ratio of hydrostatic stress to von Mises stress. Here, $\alpha$ represents the material constant, and $\sigma_H$ represents hydrostatic stress. It is claimed to be successful in metal-cutting processes.

$$\int_0^{\bar{\varepsilon}_f} \exp\left(\frac{\alpha\sigma_H}{\sigma_{eq}}\right) d\bar{\varepsilon} = C_4(Rice\ and\ Tracey) \quad 6)$$

The Oyane damage model [8] given in Eq. 7 was developed by considering the hydrostatic stress. It has been suggested that it is more successful in its predictions due to the effect of the material constant in hot-forming processes.

$$\int_0^{\bar{\varepsilon}_f} \left(\alpha + \frac{\sigma_H}{\sigma_{eq}}\right) d\bar{\varepsilon} = C_5(Oyane) \quad 7)$$

The Brozzo damage model [9] given in Eq. 8 was modified from the Cockroft-Latham damage model to include hydrostatic stress.

$$\int_0^{\bar{\varepsilon}_f} \frac{2\sigma_{max}}{3(\sigma_{max}-\sigma_h)} d\bar{\varepsilon} = C_6(Brozzo) \quad 8)$$

The Ayada damage model [10] given in Eq. 9, unlike Oyane, has studied the critical damage limit with hydrostatic stress and von Mises stress without considering the material constant.

$$\int_0^{\bar{\varepsilon}_f} \left(\frac{\sigma_H}{\sigma_{eq}}\right) d\bar{\varepsilon} = C_7(Ayada) \quad 9)$$

The Zhan damage model [11] given in Eq. 10, slightly different from other damage models, proposed a model based on the difference between the maximum principal and hydrostatic stress.

$$\int_0^{\bar{\varepsilon}_f} (\sigma_{max} - \sigma_H) d\bar{\varepsilon} = C_8(Zhan) \quad 10)$$

These damage models used to determine the critical damage limit aim to obtain a unitless critical damage coefficient based on stress or stresses. It is essential to use a vital damage model suitable for the process to be studied and to obtain the closest estimate to the result to be realized in numerical analyses. In cold forming processes where forms such as square, cylindrical, and hexagonal are shaped, damage occurs on the material at the point where the maximum principal stresses formed on the sample reach the critical damage limit of the material. In the study conducted by J. Landre et al. [12], Cockroft-Latham damage model is deemed more successful in cold forging because it focuses on the accumulation of plastic deformation due to tensile stresses, which are the primary cause of damage in cold forging processes. The model's simplicity allows for quick and reliable predictions, especially in conditions where high compressive stresses prevail, as it disregards the effects of hydrostatic pressure, unlike other more complex models. This makes it a practical and efficient tool for predicting crack initiation, with proven accuracy in both experimental and numerical studies. In the model that connects the maximum principal stress and von Mises stress to a scalar function, such as the Cockroft-Latham damage model, the simple and easy application of the model to numerical analyses makes the use of this model quite widespread. For these reasons, numerical analyses were performed on the Cockroft Latham damage model in the study.



## 4. Compression Experiment

In the compression test with 13 C45E samples, a crack was encountered after a displacement output of 6.9 mm in the flanged sample placed between two jaws, with a pressing speed of 5 mm/min. Since the measurement tolerances of the samples processed with the machining method may affect the displacement-crack behavior, it was assumed that the crack initiation would occur in the sample between 6.85 and 6.95 mm displacement (Table 3).

**Table 3.** Displacement-crack status chart of compression-tested samples

| Specimen Number | Displacement (mm) | Crack Status | Specimen | Specimen Number | Displacement (mm) | Crack Status | Specimen |
|---|---|---|---|---|---|---|---|
| 1 | 5 | No Cracks |  | 7 | 6,50 | No Cracks |  |
| 2 | 6 | No Cracks |  | 8 | 6,70 | No Cracks |  |
| 3 | 6,3 | No Cracks |  | 9 | 6,80 | No Cracks |  |
| 4 | 6,33 | No Cracks |  | 10 | 6,9 | Cracked |  |
| 5 | 6,37 | No Cracks |  | 11 | 6,9 | Cracked |  |
| 6 | 6,50 | No Cracks |  | 12 | 7 | Cracked |  |
| | | | | 13 | 7 | Cracked |  |

The Coulomb friction coefficient of the test environment will be determined based on the curves obtained from the compression test graphs. The numerical analysis results repeated with different friction coefficient values in the Simufact program will be compared with the compression test load-displacement graphs from which the crack was obtained, and the friction coefficient value with the closest curve to the compression test graphs will be accepted as the friction coefficient of the test environment (Fig. 3). It was decided to determine the friction coefficient by selecting the graph

of sample number 10, which was the first sample to obtain a crack at the lowest displacement from the four different load-displacement graphs from which the crack was received, as a guide.

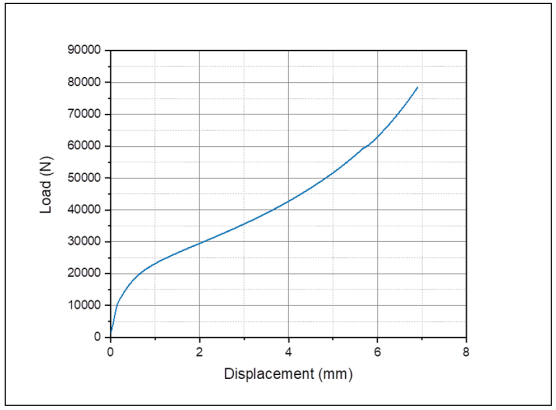


**Fig. 3** Load-displacement graph of sample number 10 in a compression test

## 5. Numerical Study

After repeating the experimental compression test performed with C45E material numerically, the aim is to determine the critical damage limit of the material according to the Cockroft Latham damage model. The FE model is developed in Simufact Forming software using the cold forming application module. An axisymmetric model, consisting of a workpiece, an upper plate, and a fixed lower plate, is developed. The workpiece is selected as elasto-plastic, while the plates are selected as rigid bodies. The workpiece geometry is meshed using quadrilateral elements with a 0.05 mm element size which is shown at Table 4. A constant Coulomb friction coefficient of 0.01 is defined for all contacting surfaces. A hydraulic press with a constant speed of 5 mm/sec is defined, and the upper plate is attached to this press. The workpiece material is C45E steel. The material is assumed to be isotropic both elastically and plastically. The hardening behavior of the material is assumed to follow Ludwick's power law. To determine the friction coefficient, multiple analyses were performed using low-density mesh, and then the simulation was repeated by increasing the finite element mesh density with the friction coefficient model having the closest curve. This is to minimize the time lost while the simulation is running. With the friction coefficient to be determined, the mesh number of the finite elements belonging to the geometry in the numerical analysis will be increased from 3028 to 15 537. Additional element density will be added to the base surfaces in the geometry, and the analysis will be repeated. Improving the mesh quality increases the sensitivity of the damage coefficient value obtained from the results and the estimation of the area where the damage occurs.

**Table 4.** Finite element analysis parameters

| Element Size | Element Count | Element Type | Ambient Temperature (C°) | Specimen Temperature(C°) | Work Piece | Jaws |
|---|---|---|---|---|---|---|
| 0,1 | 3028 | Quads(10) | 25 | 25 | Elastoplastic | Rigid |
| 0,05 | 15 537 | Quads(10) | 25 | 25 | Elastoplastic | Rigid |



In the analyses repeated with Coulomb friction coefficients of 0.01, 0.05, 0.08, 0.09, 0.1, 0.15, 0.2, and 0.3, it was observed that as the friction coefficient increased, the effective plastic strain on the geometry also increased (shifting from blue to red). It is observed that with the increase in friction, there is a tendency towards the geometry called barreling on the bottom and top surfaces, and with the decrease, the geometry tends towards the inverted hat form. As effective plastic strain increases, the level of plastic deformation in the material rises. Since the Cockroft-Latham criterion is calculated based on effective plastic strain, the probability of reaching the damage threshold also increases.

**Table 5.** Effective plastic strain results of numerical compression tests performed with different friction coefficients at 6.9 mm displacement value

| Coefficient of friction (Coulomb) | Result (@6.9 mm) | Coefficient of friction (Coulomb) | Result (@6.9 mm) |
|---|---|---|---|
| 0,01 | 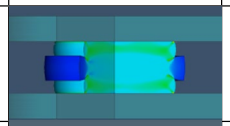 | 0,1 | 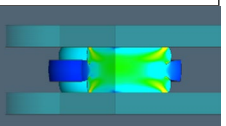 |
| 0,05 | 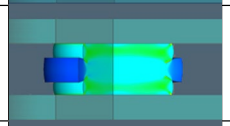 | 0,15 | 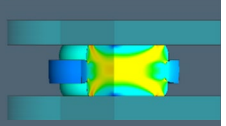 |
| 0,08 | 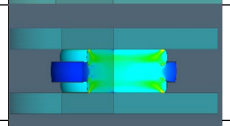 | 0,20 | 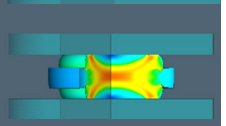 |
| 0,09 | 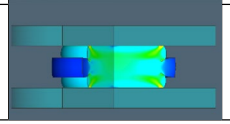 | 0,30 | 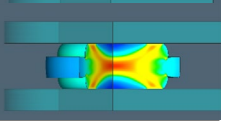 |

After comparing the experimental and numerical results by generating separate force-displacement graphs of the analyses made with different friction coefficients mentioned above in Fig. 4, the closest numerical analysis friction coefficient model to the load-displacement graph of the flanged sample with the crack was determined as 0.01 Coulomb. This value will be used as the friction coefficient parameter of the setup in the simulation, where we will evaluate the critical damage limit. The error margin between the experimental curve given in Fig. 4 and the load-displacement curves of the analysis with 0.01 Coulomb coefficient was calculated as 5.71%. The displacement value of 6.90 mm was divided into 0.50 mm intervals. The force difference at the same displacement value of the experimental and analysis curves was calculated as a percentage, and the result was obtained.

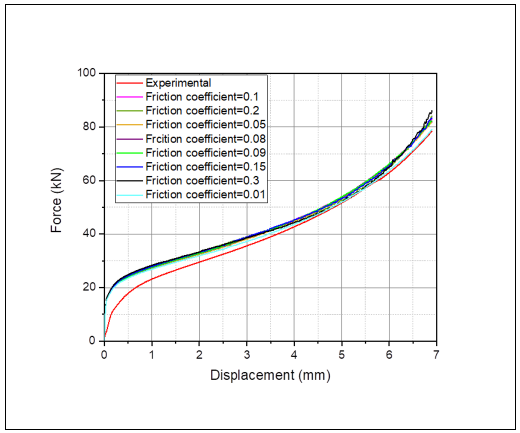


**Fig. 4.** Comparison of force-displacement results of experimental and numerical compression tests with different friction coefficient values

Increasing the number of elements generally improves the accuracy of the results since the model captures stress/strain distributions more precisely but extremely small elements can introduce rounding errors and numerical instabilities, reducing solution reliability. In the repeated analysis with improved parameters quality, the critical damage coefficient was determined as 0.47 according to the Cockroft Latham damage parameter with a friction coefficient of 0.01 at a 6.9 mm displacement value (Fig. 5). The damage coefficient value 0.47 represents the maximum damage limit at which C45E steel can be formed without damage. While the damage coefficient was 0.42 in the analysis performed with low-density mesh, the damage coefficient was 0.47 in the repeated analysis with improved mesh quality. As mesh density increases, the solution stabilizes and stops changing significantly. At this point, the solution is considered converged. The effect of mesh quality on the result is given in Figure 5.

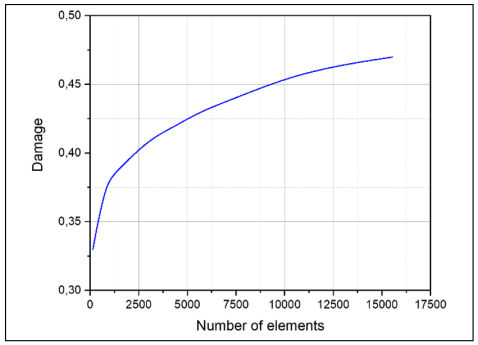


**Fig. 5** Effect of mesh qualities on damage coefficient



In the Simufact program, analyses were performed at a displacement value of 6.9 mm using different Coulomb friction values to determine the friction coefficient of the experimental setup used for compression tests. The load-displacement curves obtained from these analyses were compared with the load-displacement curve of the experiment in which crack formation was observed in the Galdabini device. As a result, the analysis that gave the closest load-displacement curve to the experimental graph was taken as a reference to determine the friction coefficient. By repeating the numerical analysis with the determined 0.01 Coulomb friction force value and the 6.9 mm displacement value, a Cockroft Latham damage value of 0.47 was obtained at the value where the crack was obtained. The determined 0.47 critical damage limit value indicates that the damage that may begin due to the stresses formed on the material will occur when the Cockroft Latham damage value of 0.47 is reached.

## 6. Results and Discussion

As a result of the compression test performed at room temperature, a crack was detected on the sample at a displacement value of 6.90 mm. In the numerical analyses, a Cockroft Latham critical damage limit of 0.42 was determined at a displacement value of 6.9 mm in the geometry with 3028 elements. In contrast, a Cockroft Latham critical damage limit value of 0.47 was obtained in the geometry with 15 537 elements. This value indicates the maximum value that the C45E material can be subjected to plastic deformation without suffering damage at the macro level with the experimental and numerical analysis parameters.

The difference between the experimental load displacement and numerical curves was examined by taking the average force values at each 0.50 mm displacement interval. Reviewing the 6.9 mm displacement value where the crack occurred, the deviation rate between the two curves was 5.71%. As the displacement amount increased, tool marks and flaking caused by principal stresses were observed on the material; the width of the crack formed with increasing displacement increased from 0.3 mm to 1.24 mm and its length from 0.68 mm to 1.77 mm.

When the study results are compared with the existing studies in the literature, important conclusions have been made about the accuracy of the methods used and the effectiveness of the damage model. In the study conducted by J. Landre et al. [12] the damage effects of different geometries were investigated in the tests performed with AISI1040 (%0.40C) steel alloy and in the study conducted by Sampaio et al. [13] with AA6082 aluminum, and as in this study, damage behaviors that could not be obtained with conventional test methods and geometries were observed with the sample geometry explicitly determined for the C45E material, which was not previously encountered in the literature (Fig. 6).

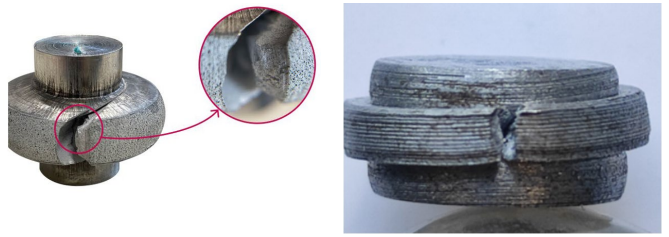

**(a)** **b)**

**Fig. 6** Images of cracks obtained with center flange geometries (a) AA6082 [13] (b) C45E

*Image (a) adapted from [Rui F.V. Sampaio et al.,2023, On the utilization of radial extrusion to characterize fracture forming limits. Part II: testing and modelling, Materials Research Proceedings]. Used with permission.*

As in the studies of authors such as Özgür Koçak [14] ,Rui F.V. Sampaio et al. [13], Tibor Kvackaj et al. [15] the crack formed in the flange region of the center-flanged sample in the compression test conducted in this study occurred at an angle perpendicular to the flange plane (Fig. 7).

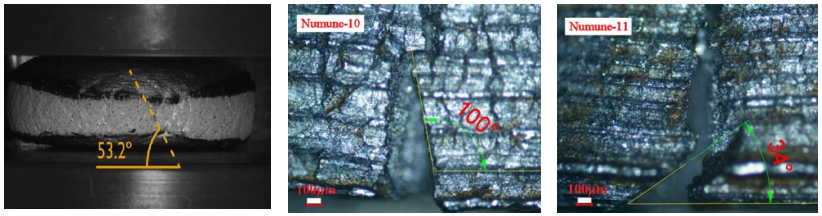


(a) b)

**Fig. 7** Cracks occurring at an angle perpendicular to the flange plane (a) the Crack angle formed on the flange, Sampaio et al.[13] (b) Crack angles of samples numbered 10 and 11 at 50x zoom
*Image (a) adapted from [Rui F.V. Sampaio et al.,2023, On the utilization of radial extrusion to characterize fracture forming limits. Part II: testing and modelling, Materials Research Proceedings]. Used with permission.*

Stebunov, S. et al.(2018) [16] emphasized in their study comparing different damage models that the Cockroft-Latham model gives the most accurate results, especially in ductile materials. Similarly, this study's results obtained with the Cockroft-Latham model were consistent with the experimental data (Fig. 8).

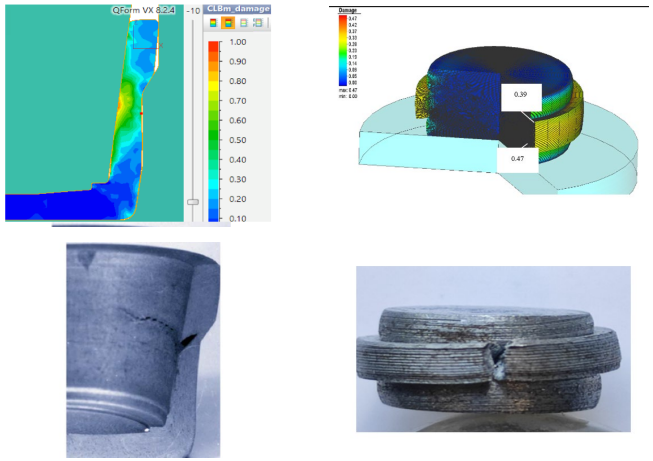


(a) b)

**Fig. 8** Damage intensity and crack images in CL damage model (a) 1040 [16] (b) C45E
*Image (a) adapted from [Stebunov, S. et al, 2018, Prediction of fracture in cold forging with modified Cockcroft-Latham criterion. Procedia Manufacturing]. Used with permission.*



## 7. Conclusion

In future studies, it is recommended that each component be studied to calculate the friction coefficient of the components of the experimental setup containing more than one component. In order to correctly determine the friction coefficient of each component, multiple repetitions should be made in the analysis environment and matched with the experimental graphs. However, this will require a large number of analyses and long analysis times. In the analyses to be performed, modeling the experimental setup components as elastic instead of rigid will also take into account the deformations that these parts are exposed to in the elastic region during the experiment. In this way, the obtained load-displacement graphs will provide analysis outputs closer to the experimental results with a deviation lower than the 5.71% deviation rate calculated in this study. During the experiment, the machine adaptation will be made so that the machine elements such as jaws, bearings, bushings, etc. in the test device, which can flex under load, do not affect the load-displacement graph obtained as a result of the experiments, and this will increase the sensitivity of the results in the analysis environment by reducing the difference between the load-displacement graphs taken as reference in determining the friction coefficient of the experimental environment.

In future studies, instead of the material model created with the material chemical composition certificate in the numerical environment, transferring the flow curves obtained from experiments with different strain rates and temperature values to the simulation will reduce the error margin originating from the material model. Creating the material model by performing these experiments will increase the sensitivity of the analyses in the determination phase of the friction coefficient and of the compression test environment and the analyses performed after the compression test.

## Interest Statement

On behalf of all authors, the corresponding author states that there is no conflict of interest.

## References

1 McClintock, F.A.: A Criterion of Ductile Fracture by Growth of Holes. J. Appl. Mech., 35, 363-371 (1968) https://doi.org/10.1115/1.3601204

2 Rice, J. R., Tracey, D. M.: On the Ductile Enlargement of Voids in Triaxial Stress Fields. J. Mech. Phys. Solids, 17, 201-17 (1969)
https://doi.org/10.1016/0022-5096(69)90033-7

3 Cockroft, M. G., Latham, DJ.: Ductility and the Workability of Metals. J. I. Met., 96, 33-39 (1968)

4 Kachanov, L. M.: Time of the rupture process under creep conditions. Izv Akad. Nauk. SSR, 8, 26-31 (1958)

5 Rabotnov, Y., Hetenyi, M., Vincenti, W.: Applied Mechanics. Proceedings of the 12th International Congress of App. Mech., 342-320 (1968)

6 Lemaitre, J.: Evaluation of dissipation and damage in metals. Proceedings of I.C.M.1., 1 (1971)

7 Akyüz, U., Tekkaya, A. E., Soyarslan, C., Groche, P., Rathmann, T.: Plastisite için Hasar Kavramının Modellenmesi. Misag Julich 04 Projesi, Tübitak, Ankara (2007)

8 Oyane, M., Sato, T., Okimoto, K., Shima, S.: Criteria for Ductile Fracture and Their Applications. J. Mech. Work. Technol., 4, 65-81 (1980)
https://doi.org/10.1016/0378-3804(80)90006-6

9 Brozzo, P., Deluca, B., Rendina, R.: A New Method for the Prediction of Formability in Metal Sheet, Sheet Metal Forming and Formability. Proceedings of the 7th Biennial Conference of the International Deep Drawing Research Group (1972)

10 Ayada, M., Higashino, T., Mori, K.: Central bursting in extrusion of inhomogeneous materials. Proceedings of the first ICTP, 1, 553-558 (1984)

11 Zhan, M., Gu, C., Jiang, Z., Hu, L., Yang, H.: Application of ductile fracture criteria in spin-forming and tube-bending processes. Computational Materials Science, 47(2), 353-365 (2009)
https://doi.org/10.1016/j.commatsci.2009.08.011

12 Landre, J., Pertence, A., Cetlin, P. R., Rodrigues, J. M. C., Martins, P. A. F.: On the utilisation of ductile fracture criteria in cold forging. Finite Elements in Analysis and Design, 39, 175-186 (2003)
https://doi.org/10.1016/S0168-874X(02)00065-3

13 Sampaio, R. F. V., Pragana, J. P. M., Bragança, I. M. F., Silva, C. M. A., Nielsen, C. V., Martins, P. A. F.: On the utilisation of radial extrusion to characterize fracture forming limits, Part II: testing and modelling. Materials Research Proceedings, 25, 237-244 (2023)
https://doi.org/10.21741/9781644902417-30

14 Koçak, Ö.: Analysis of the Formability of Metals (Master's Thesis). Natural and Applied Sciences, METU, Ankara (2003)

15 Kvačkaj, T., Tiža, J., Bacsó, J., Kováčová, A., Kočiško, R., Pernis, R., Fedorčáková, M., Purcz, P.: Cockroft-Latham ductile fracture criteria for non ferrous materials. Materials Science Forum, 782, 373-378 (2014)
https://doi.org/10.4028/www.scientific.net/MSF.782.373

16 Stebunov, S., Vlasov, A., & Biba, N. Prediction of fracture in cold forging with modified Cockcroft-Latham criterion. Procedia Manufacturing, 15, 519–526 (2018)
https://doi.org/10.1016/j.promfg.2018.07.264

# FINITE ELEMENT MODELS FOR CLINCHING, PUSH-OUT AND TORQUE-OUT TESTS OF SELF-CLINCHING NUTS

*Hatice SANDALLI YILDIZ*
*Binnur GÖREN KIRAL*
*Burak Berk ARINCI*
*Ege ŞAHİN*

Materials Testing

# FINITE ELEMENT MODELS FOR CLINCHING, PUSH-OUT AND TORQUE-OUT TESTS OF SELF-CLINCHING NUTS

**Hatice SANDALLI YILDIZ, Binnur GOREN KIRAL, Burak Berk ARINCI, Ege SAHIN**

***Corresponding author: Binnur Gören Kiral,** Dokuz Eylul Universitesi, Izmir, 35210, Türkiye, E-mail: binnur.goren@deu.edu.tr. https://orcid.org/ 0000-0001-7760-9306
**Hatice Sandalli Yildiz,** The Graduate School of Natural and Applied Sciences, Department of Mechanical Engineering, Dokuz Eylul University, Buca, Izmir, 35390, Türkiye; and Norm Fasteners Co., Izmir, 35620, Türkiye
**Burak Berk Arinci and Ege Şahin,** Norm Fasteners Co., Izmir, 35620, Türkiye

## Abstract

Self-clinching nuts are increasingly used in automotive industry for fastening bolts to metal sheets which are too thin to be threaded directly. To ensure safe and reliable use, this type of nuts must meet defined mechanical performance criteria, such as push-out and torque-out resistance. Finite element analysis (FEA) plays a crucial role in observing the deformation of the sheet metal during the clinching process and in assessing whether the nuts meet the expected performance standards. This study focused on the development of finite element models for clinching, push-out and torque-out tests for self-clinching nuts. The accuracy of the developed models was evaluated by comparing their results with corresponding experimental data. The findings of the study revealed that mesh quality significantly affect the accuracy of the simulation results. Additionally, it was observed that the compliance of the testing machine plays an important role in the discrepancy between experimental and simulation outcomes during the clinching process.

**Keywords:** Fasteners; finite element analysis; self-clinching nuts; torque-out resistance; push-out resistance

## 1. Introduction

A traditional clinch nut is permanently assembled into a portion of metal sheet, forming a mechanically interlocked joint that makes the nut a permanent part of the sheet. The nut is assembled by deforming the sheet metal, rather than welding the nut. It, therefore, offers stronger and more durable joints. This type of nut is commonly used in automotive industry for fastening bolts to metal sheets that are too thin to be threaded directly [1-3]. Typical applications include body-in-white assembly, interior trim and instrument panels, seating systems, and more.

Installation of the typical clinch nut can be described as follows: first, the nut is positioned into a preformed hole in the sheet, and when an external axial force is applied to the nut, the bulge formed on the flange causes the sheet material to displace, flowing into the undercut area of the nut. The force continues until the top of the flange is fully seated on the sheet. At this stage, the displaced metal fills the undercut and the nut become integral part of the sheet metal [4,5].

After clinching, the nut must satisfy two critical mechanical performance criteria: torque-out resistance and push-out resistance. Torque-out resistance ensures that the nut does not rotate relative to the sheet when a bolt is inserted and tightened, while push-out resistance prevents the nut from being pulled out of the sheet under external axial loading [6].

Balon et al. [7] researched the joint strengths of M10 and M12 nuts after clinching process. For this study, 200 and 250 kN forces were used to clinching of M10 and M12 nuts, respectively. The sheet material was selected as DP-500 ultra-high strength steel and the nut material was selected as 35B2 special alloy. Results of the research showed that the self-clinching process strengthens the used parts in the joining area and reduced the impact of temperature.

Gardstram [8] conducted a finite element study to simulate a pierce nut installation process using Deform-2D and Abaqus-Explicit. Three different models were developed for various purposes: a 2D model, a 3D-180 model, and a 3D-360. DP600 with a thickness of 1.5 mm was selected as the sheet material. The study indicated that for the centered nut system, the 2D model was the most reliable and time-effective. However, the 2D model was insufficient for handling eccentric situations. Additionally, the research highlighted a discrepancy between experimental and simulation results, attributing to the selected fracture criteria for cutting step.
Daud [6] investigated the effects of various parameters such as hole geometry, sheet thickness, and material type on the performance of a self-clinching nut. Torque-out tests were conducted on the samples using a semi-automatic torsion machine, with five different levels tested for each parameter. Each test was carried out until the nut either rotated or experienced failure, and the associated torque values were measured. The Taguchi Method was then applied to evaluate the influence of each parameter and to determine the optimal parameter combination. The results of the study indicated that hole diameter is the most influential parameter within the selected parameters affecting the torque-out performance of the nut for the tested sheet materials.

Finite element analysis plays a crucial role in examining the contact conditions between components and assessing the strength of joints. Numerous studies in the literature have focused on the development of finite element models for various types of joints, including welded, adhesively bonded, bolted, and riveted connections etc. [9-15].

In addition to research articles in the literature, there are also many patents about clinch nuts [16-20]. However, there is a noticeable lack of studies that comprehensively examine finite element models of mechanical performance tests of clinch nuts. This research focused on the development of finite element models for clinching process of a nut onto a sheet material. In addition, finite element models were developed to simulate the push-out and torque-out behaviours of the clinched nut. The accuracy of the developed models was evaluated by comparing their results with corresponding experimental data.

## 2. Experimental and Numerical Studies

### *2.1. Experimental*

Initially, a specific clinch nut geometry was selected for the study. The nuts were produced with a horizontal six-station cold forging machine, followed by a tapping operation to form internal threads. After forming, the nuts were clinched into sheet metal, and their mechanical performance was evaluated through push-out and torque-out tests. The nuts were produced from 17MnB3 steel, which has a yield strength of 354 MPa and an elastic modulus of 210 GPa at room temperature. The sheet metal used was DC04 steel, with a yield strength of 230 MPa, an elastic modulus of 210 GPa, and a thickness of 2.90 mm. The geometry of the sheet metal employed during the clinching process is illustrated in Figure 1.

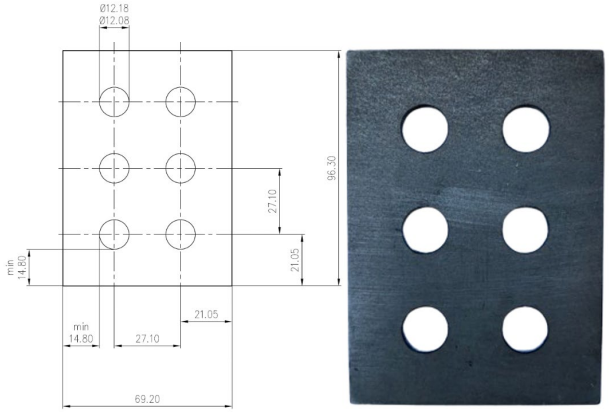


**Figure 1.** Sheet metal geometry used in experimental tests

The clinching and push-out tests were performed by using a universal tensile testing machine, while torque-out tests were performed with a digital torque-meter. During the clinching, the nut was placed into the preformed hole in the sheet and the force applied to the nut was gradually increased until the top of the nut was fully seated on the sheet. It was verified by taking a cross section whether the nut was fully seated on the sheet metal (Figure 2).

**Figure 2.** Cross-sectional view of the joint, showing the interlocking features between the clinch nut and the sheet metal after the clinching process

After the clinching process, push-out tests were conducted on a group of nuts clinched onto the sheet using the test setup shown in Figure 3. An external threaded part was inserted to nut and an axial compression force was applied to this component. Force-displacement curve was recorded throughout the test.



**Figure 3.** The set-up for push-out tests

Following the push-out tests, torque-out tests were carried out on a separate group of nuts. In these tests, bolts of property class 10.9 were inserted into the nuts, and torque was applied using an Atlas Copco STWrench (Figure 4) and it was checked whether the nut rotated at the minimum defined torque value. The bolts were selected based on the property class of the corresponding nuts.

**Figure 4.** The test set-up for torque out tests

### *2.2 Numerical Studies*

In this section, first, forming simulations were carried out in order to obtain nut geometry with actual corner losses and dimensions. Simufact Forming software is used for the finite element analysis. Forming simulations started with an axis-ymmetric model, consisting of a workpiece, stationary die and moving die components. Throughout the simulation, the workpiece was transferred sequentially between stations, from cutting to piercing, to accurately obtain the deformation hardening effects experienced by the nut. First four stations, including cutting, was modelled as 2D-axisymmetric, while the final three stations were modelled as 3D-180°. The workpiece was selected as elastoplastic, and the die components were selected as rigid. At the final forming station, the nut was meshed with hexahedral elements with an 0.16 mm

element size and 61,202 total element count. The material, 17MnB3, was assumed isotropic in both elastic and plastic behavior, with its hardening characterized by Ludwik's power law.

In the second part of numerical studies, finite element models for clinching, push-out and torque tests were developed. In clinching simulations, the nut geometry obtained from forming simulations was used as workpiece material thus, increasing the accuracy of the model. The friction coefficient of the nut coating, 0.13, was used as the friction coefficient. The sheet metal was modeled as elastoplastic, with DC04 steel as the material, whose chemical composition determined by spectro analysis is provided in Table 1. The nut was initially modeled as elastoplastic in the first analysis (Figure 5). It was then modeled as rigid, and the results of the two analyses were compared in terms of the differences between their load-displacement curves and solution times. Since the obtained load-displacement curves were nearly identical, the nut was ultimately modeled as rigid and threadless to reduce the solution time. In addition, to shorten the solution time, the sheet metal was not modeled with its full external dimensions. Instead, a reduced section representing the critical area of interest was defined. A rigid part surrounding the outer edges of the modeled sheet section was also created and glued to it. This approach aimed to accurately simulate the real test conditions while optimizing computational efficiency. The sheet metal was meshed using 88,372 hexahedral elements with a 0.2 mm element size, determined through a mesh sensitivity study. The test apparatus was drawn exactly in accordance with the dimensions used in the experiments and was used rigidly during the analysis. A 5 mm/min constant speed hydraulic press is defined for the clinching process. Since the tests on the test device were carried out with force control, the model created was designed to stop when the press force reached 120 kN (Figure 6).

**Table 1.** Chemical composition of the sheet metal (wt.%)

| C | Mn | P | S | Cr | Mo | Ni | Al | Cu | Ti | V | Sn |
|---|---|---|---|---|---|---|---|---|---|---|---|
| 0.058 | 0.195 | 0.013 | 0.011 | 0.053 | 0.005 | 0.045 | 0.067 | 0.090 | 0.002 | 0.001 | 0.001 |

For the push-out and torque tests, the deformed sheet metal from the clinching simulation was used as the workpiece material. Push-out simulations utilized a 3D model with a 180° segment, while torque tests employed a full 3D 360° model. In both cases, the nut was modeled as rigid. An axis of rotation was defined for the torque-out tests, where the nut was rotated at an angular velocity of 20 rpm (Figure 7).

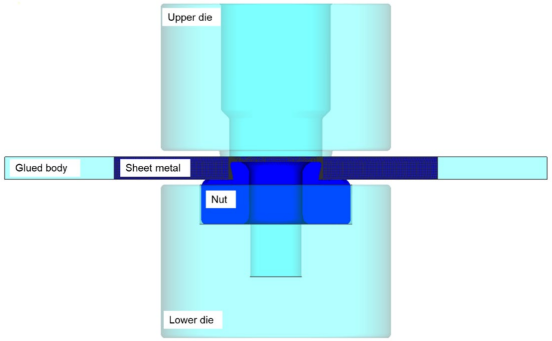


**Figure 5.** Scetch of the finite element model of the clinching process with elastoplastic nut and sheet metal



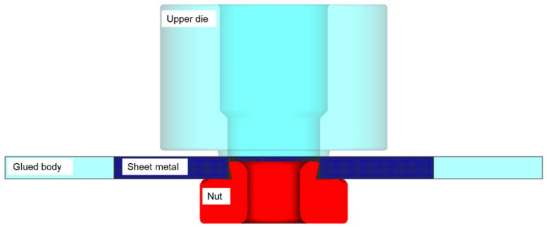


**Figure 6.** Scetch of the finite element model of the clinching process with rigid nut and sheet metal

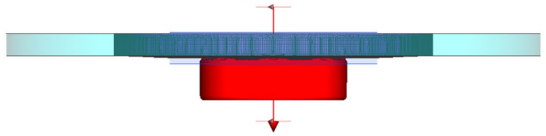

**Figure 7.** Scetech of the finite element model of the clinching process with rigid nut and sheet metal

## 3. Results and Discussion

Load-displacement curves of five samples from clinching tests are given in Figure 8. The tests were carried out with force-controlled mode and they were stopped when the press force reached 120 kN. According to results, all samples follow the similar paths during clinching and under 120 kN force, displacement required to obtain a full engagement between sheet metal and nut is between 1.86 to 1.90 mm. To facilitate comparison between experimental and numerical results, the average load-displacement curve of the tested samples was plotted and is presented in Figure 9.

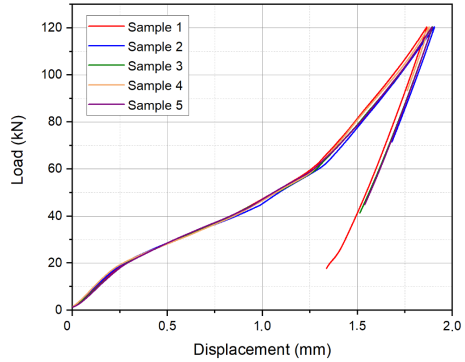


**Figure 8.** Load-displacement curves of experimental clinching tests

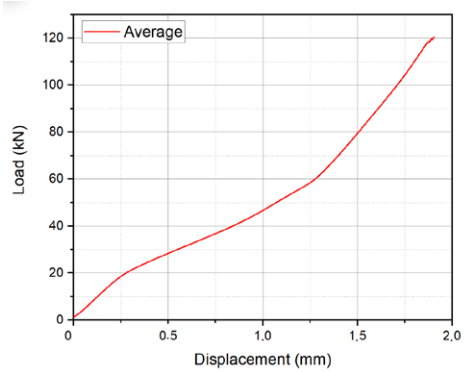


**Figure 9.** Average load-displacement curve for experimental clinching tests

In order to be compatible with the experimental studies, the clinching process was carried out with 120 kN in the finite element analysis. The sheet metal was initially meshed with hexahedral elements using an element size of 0.85 mm, resulting in a total of 3,842 elements. To investigate the effect of mesh density on the results, the element size was gradually reduced in steps down to 0.2 mm. The results appear to converge at an element size of 0.3 mm, corresponding to a total element count of 26,386, as shown in Figure 10.

To shorten the solution time, the nut was modeled as rigid and threadless. However, to evaluate the effect of this assumption, a separate finite element model was created in which the nut was modeled as elastoplastic. The load-displacement curves of the two models were then compared. The results showed that the curves (Figure 11) were almost identical, but the solution time of model with elastoplastic nut was four times higher. Therefore, the remaining analyses were performed using the rigid nut model.

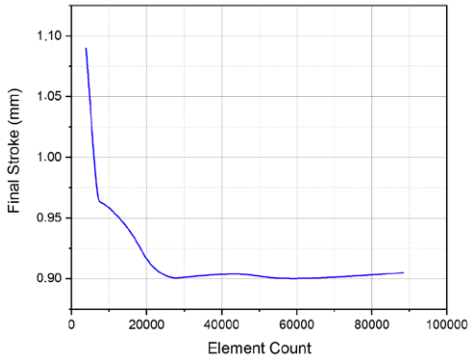


**Figure 10.** Effect of element count on the final stroke at 120 kN clinching force



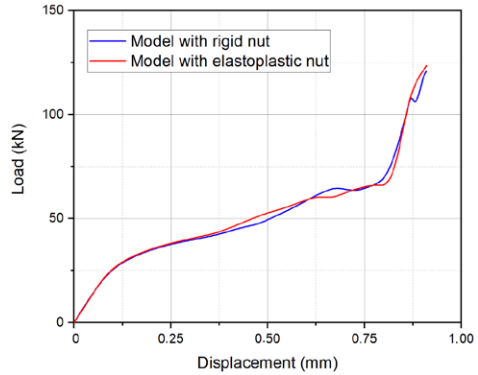


**Figure 11.** Effect of modeled nut on the results

Then, material flow was investigated, as presented in the Figure 12, the sheet metal was deformed and flowed into the undercut area. Increased contact between the nut and the sheet metal led to greater deformation. Furthermore, a change in the sheet metal temperature was also observed. The load-displacement curve was plotted for the simulation results. Figure 13 shows the average curve of experimental results and the curve obtained from the simulation. A significant discrepancy is observed between the curves. In order to obtain more accurate simulation results, the compliance of testing device during experimental tests was investigated.

The compliance of a test machine can be explained as the overall deformation that occurs in its components during testing. It's a measure of the flexibility of the machine or how much it deforms in response to an applied force. Compliance is typically an undesirable feature, because it can introduce errors or inaccuracies into the test results. In the case of a compression testing machine, compliance includes the deformation of the machine itself, when the force is applied to the test sample. This deformation is typically much smaller than the deformation of the sample itself, but it still needs to be accounted for more reliable results.

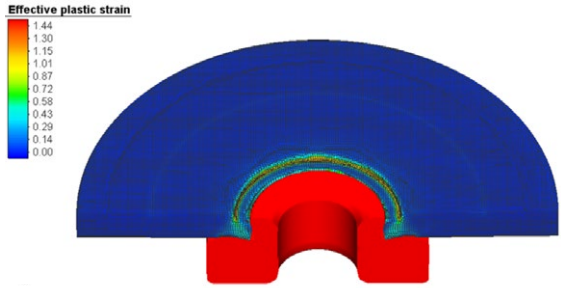


**(a)**

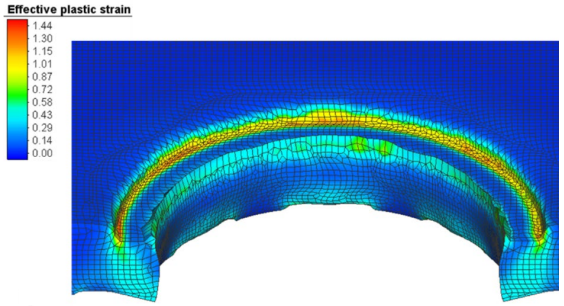


(b)

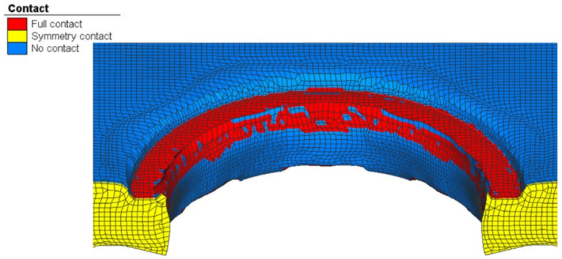


(c)

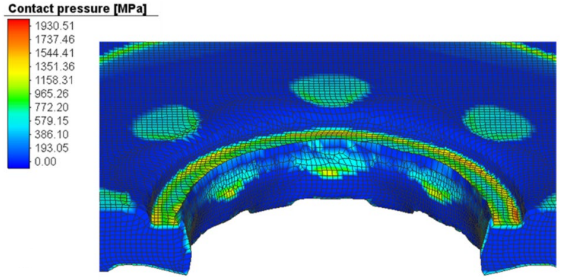


(d)

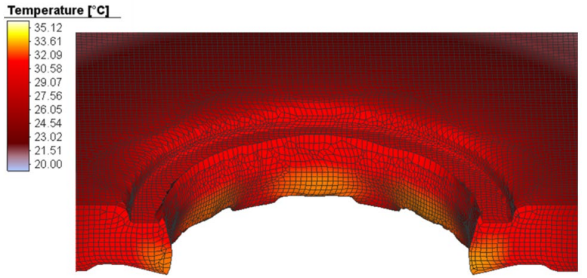


(e)

**Figure 12.** a) Nut and deformed sheet metal after clinching, b) effective plastic strain, c) contact, d) contact pressure, e) temperature on the sheet metal

According to literature, there are three methods to calculate compliance of machine which can be listed as: i) direct method, ii) elastic deformation of known material, iii) finite plastic strains. In the direct technique, a compression test is performed without any samples between the plates, and the load-displacement curve of this test is plotted. Then, curve fitting is applied, and an expression for the machine compliance in terms of the applied load is derived [21].

To find the compliance of the testing device, direct technique was applied and compression test was performed without any samples between plates. Force-displacement was plotted and linear curve fitting was applied (Figure 14). After obtaining slope of the curve, by using Equations (1)-(3) necessary calculations to obtain actual deformation of the samples were made. By subtracting the deformation of the machine components (compliance) from the total measured deformation, a corrected curve was obtained, which is referred to as the compliance curve in Figure 15. After applying compliance correction from the experimental curve, the slope changes, and the displacement values at given loads become similar to those from the simulation. The percentage error between experimental and simulation displacement results at 120 kN was calculated as %52, whereas the percentage error between compliance corrected and simulation results was reduced to %3.

$$\tan\alpha = K = \frac{F}{\delta_C} \quad (1)$$

$$\delta_C = \frac{F}{K} \quad (2)$$

$$\delta_S = \delta_R - \delta_C \quad (3)$$

with $d_c$, $d_R$ and $d_S$ : Deformation of the machine components (mm), total deformation (mm) and deformation of the sample (mm), respectively.

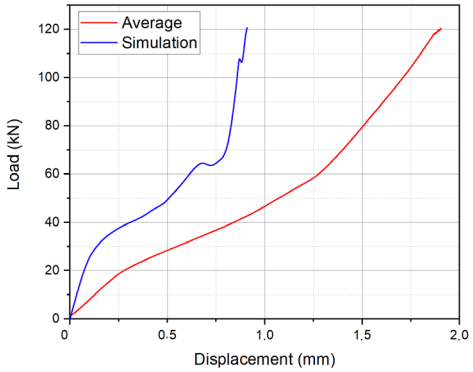


**Figure 13.** Load-displacement curves of simulation and average experimental results

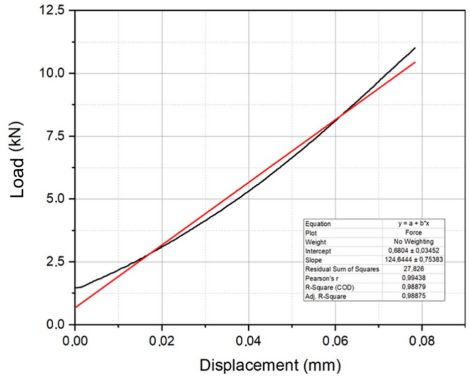


**Figure 14.** Compliance curve

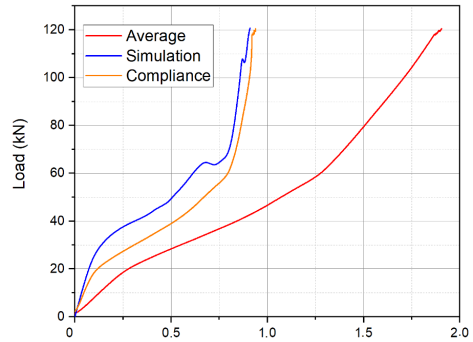


**Figure 15.** Load-displacement curves of simulation, average experimental and compliance corrected experimental results



After obtaining a reliable model for clinching, a finite element model for push-out test was developed. The deformed sheet metal from clinching simulations was used as workpiece material and other parameters were kept same as the clinching model. At push-out simulations, simulation was run until the nut separated from the sheet metal as presented in Figure 16. Obtained load-displacement curve from simulations is given in Figure 17. 5.92 kN of push-out force was required for the simulated model. According to the experimental results (Figure 18), the push-out value varies between 5.3-5.83 kN. There is a 1.7% error between the best experimental data and the simulation result, and approximately 6% difference with the average experimental data. This variation is due to fluctuations in the collar diameter of the nut, collar height and angle of the collar coming from cold forging process. The most ideal situation was created in the simulation model.

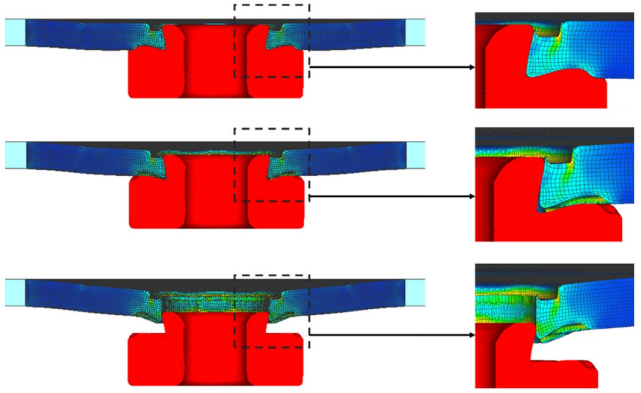

**Figure 16.** Separation of the nut from sheet metal during push-out simulations

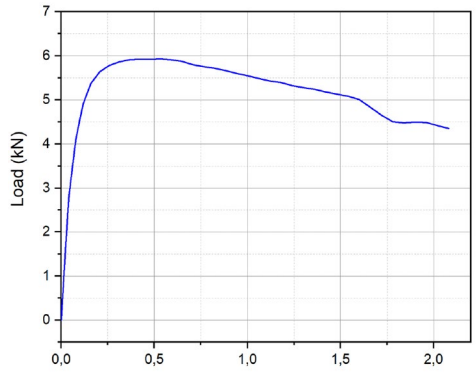


**Figure 17.** Load-displacement curve obtained from push-out simulation

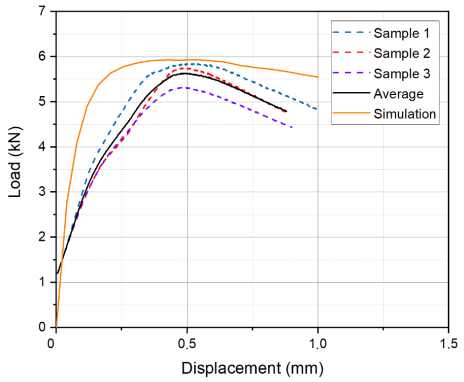


**Figure 18.** Load-displacement curves of experimental push-out tests

As a final step, a finite element model for torque-out tests was developed. The deformed sheet metal from the clinching simulation was expanded from 180° to 360° by using mirror symmetry and used as the workpiece material. An axis of rotation was defined for the torque-out tests, where the nut was rotated at an angular velocity of 20 rpm. Obtained torque-time curve from simulations is presented in Figure 19. According to the results, a torque of 102 N·m is required to rotate the nut relative to the sheet metal. In the experiments, bolts with a property class of 10.9 were inserted into the nuts, and torque was applied through the bolts; however, only 55 N·m torque could be applied before the bolts failed. Therefore, the simulation results could not be verified up to 102 N·m. Nevertheless, it was observed that higher torque values are required to rotate the nut relative to the sheet metal, and the simulation results confirm this behavior.

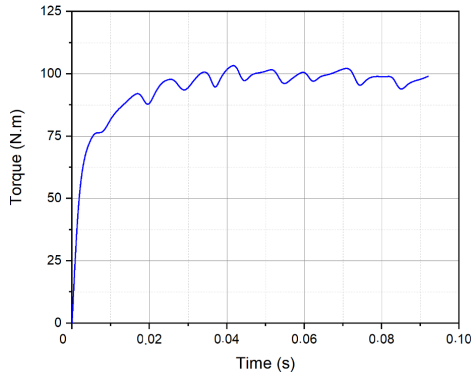


**Figure 19.** Torque-time curve obtained from torque-out simulation

## 4. Conclusion

The following results have been drawn from this work, which focused on the development of finite element models for clinching process, push-out and torque-out tests of self-clinching nuts:

- The mesh quality significantly affects the accuracy of the simulation results. The results appear to converge at an element size of 0.3 mm, corresponding to a total element count of 26,386. Below this size, displacement at 120 kN appears to deviate from experimental results.



- The compliance of the testing machine has a significant impact on the experimental results during the clinching process, where the sheet metal is compressed toward the nut and deformed. Deformation of the machine components introduces inaccuracies into the experimental results, leading to discrepancies between the experimental and simulation results.

- After obtaining compliance-corrected experimental curves, the developed finite element model for the clinching process was accurate enough to predict results within a 3% error. The reliability of the clinching model also affected the prediction capability of the finite element model for the push-out test, which predicts results with a 6% error. This error can be reduced if the production technique for the nuts is changed. Due to the nature of the cutting step in cold forging, fluctuations in nut dimensions occur during mass production, which affect the experimental results.

- In this study, the torque-out simulation results could not be fully verified up to 102 N·m since the bolts failed before reaching this torque in experiments. To validate the simulations, bolts with a higher property class can be used and the experiments repeated.

## Acknowledgment

The authors would like to acknowledge Norm Fasteners for their valuable support and for providing the necessary resources and experimental facilities that made this study possible.

## Research ethics

Not applicable.

## Informed consent

Not appllicable.

## Author contributions

The authors have accepted responsibility for the entire content of this manuscript and approved its submission.

## Use of Large Language Models, AI and Machine Learning Tools

None declared.

## Conflict of interest

The authors state no conflict of interest.

## Research funding

None declared.

## Data availability

Not applicable.

## References


1 Female Clinch Fastener with Cold-Formed Locking Flange and Associated Installation Method, by R. M. Fultz. (1993, August 23). Patent US5445483A [Online]. Available: https://worldwide.espacenet.com/patent/search/family/022333083/publication/US5445483A?q=US5445483A

2 The Self-Clinching Fastener Handbook HB-3, PennEngineering®, 2021.

3 Sherex Fastening Solutions. "Clinch Nuts." sherex.com. Accessed: June, 10, 2025. [Online]. Available: https://www.sherex.com/clinch-nuts/

4 J C Gupta & Sons. "Self-clinching Nuts". jcfasteners.com. Accessed: June, 10, 2025. [Online]. Available: https://www.jcfasteners.com/products/self-clinching/clinch-nuts/

5 R.F.V. Sampaio, J.P.M. Pragana, I.M.F. Bragança, C.M.A. Silva and P.A.F. Martins, "A self-clinching fastener for hidden lap joints," CIRP Journal of Manufacturing Science and Technology, vol.37, pp. 434-442, 2022, DOI: 10.1016/j.cirpj.2022.02.022

6 N. A. M. Daud, "Effect of Hole Size, Sheet Thickness and Material Type to the Performance of the Self-Clinching Fastener". Bachelor's dissertation, Manuf. Eng. with Manage., Universiti Sains Malaysia, Pulau Pinang, Malaysia,2019. [Online].

7 P. Balon and A. Swiatoniowski, "Stamping automotive parts with clinch nut process", AIP. Conf. Proc., vol. 1567, no.1, pp. 971-974, 2013, DOI: 10.1063/1.4850132

8 J. Gardstam, "Simulation of mechanical joining for automotive applications". Licentiate Thesis, Department of Mechanics, Royal Institute of Technology, Stockholm, Sweden, 2006.

9 M. Böhnke, F. Kappe, M. Bobbert and G. Meschut, "Influence of various procedures for the determination of flow curves on the predictive accuracy of numerical simulations for mechanical joining processes," Materials Testing, vol.63, no.6, pp. 493-500, 2021, DOI: 10.1515/mt-2020-0082

10 O. İyibilgin, E. Gepek, L. Bayram, E. Drampalos and A. Shoaib, "Pull-out strength of screws in long bones at different insertion angles: finite element analysis and experimental investigations," Materials Testing, vol.66, no.3, pp. 380-388, 2024, DOI: 10.1515/mt-2023-0239

11 X. Liang, R. Wang, G. Liu and W. Yan, "Fatigue analysis of TIG welded joints of dissimilar aluminum alloys," Materials Testing, vol.67, no.7, pp. 1127-1139, 2025, DOI: 10.1515/mt-2024-0476

12 M. A. Koksal and A. Yıldız, "Experimental testing and numerical simulations of 3D-printed PETG pins used for vehicle pedals," Materials Testing, vol.66, no.7, pp. 1084-1094, 2024, DOI: 10.1515/mt-2024-0007

13 İ. Y. Sülü, "Mechanical analysis of composite plates adhesively joined with different single-lap techniques under bending loading," Materials Testing, vol.65, no.12, pp. 1890-1905, 2023, DOI: 10.1515/mt-2023-0137

14 F. Lambiase and A. Di Ilio, "Optimization of the clinching tools by means of integrated FE modeling and artificial intelligence techniques," Procedia CIRP, vol.12, pp. 163-168, 2013, DOI: 10.1016/j.procir.2013.09.029

15 H.-S. Byun and G.-Y. Kim, "Optimization design of the clinch stud using the finite element analysis and the Taguchi method," Journal of the Korea Academia-Industrial Cooperation Society, vol.14, no.7, pp. 3135-3141, 2013, DOI: 10.5762/KAIS.2013.14.7.3135

16 Self-flanging nut and joint construction, by J. A. Jack. (1975, December 15). Patent US64089775A [Online]. Available: https://worldwide.espacenet.com/patent/search/family/024570126/publication/US4018257A?q=US64089775A

17 Nut with lug flare, by W. R. Pamer and D. P. Dennis. (2009, December 22). Patent US2009069202W [Online]. Available: https://worldwide.espacenet.com/patent/search/family/044155686/publication/US2012219377A1?q=US2009069202W

18 Clinch type fastener, by J. Milliser. (1985, June 17). Patent US74562385A [Online]. Available: https://worldwide.espacenet.com/patent/search/family/024997523/publication/US4637766A?q=US74562385A

19 Pierce nut and use thereof, by J. Gardstam. (2007, Nov. 08). Patent US2007258788A1 [Online]. Available: https://worldwide.espacenet.com/patent/search/family/038661307/publication/US2007258788A1?q=US2007258788A1

20 Heavy metal pierce nut, by J. M. Parker. (2007, Nov. 08). Patent WO2007/127334A2 [Online]. Available: https://worldwide.espacenet.com/patent/search/family/040149821/publication/WO2007127334A2?q=WO2007%2F127334A2

21 S. R. Kalidindi, A. Abusafieh and E. El-Danaf, "Accurate characterization of machine compliance for simple compression testing", Experimental Mechanics, vol. 37, pp. 210-215, 1997, DOI: 10.1007/BF02317861


## The authors of this contribution:


Hatice Sandallı Yıldız is a PhD candidate in Mechanical Engineering at the Department of Mechanics, Dokuz Eylul University. Additionally, she works as a Research and Development Specialist at Norm Fasteners. Her research interests include joining technologies, cold forging, finite element analysis, and composite materials.

Prof. Dr. Binnur Gören Kıral received her PhD in Mechanical Engineering at Dokuz Eylul University in 2004. She has been working as a Professor since 2016 in the Department of Mechanical Engineering at Dokuz Eylul University. Her main research fields are solid mechanics, finite element analysis, stability, and composite materials.

Burak Berk Arinci was born in Kyrenia in 1994. He graduated from Dokuz Eylul University, Mechanical Engineering in 2016. He began his career as a design engineer at several companies. In 2024, he completed his Master of Science in Gazi University, Industrial Design Engineering. Now, he is working at Norm Fasteners as a Tooling Design Specialist.

Ege Şahin was born in Izmir. He is a mechanical engineer graduated from Dokuz Eylul University. He has been working in Norm Fasteners as Engineering Executive for 7 years.

# CORROSION PERFORMANCE OF WC-CO DIE INSERTS BORIDED AT DIFFERENT TEMPERATURES FOR COLD FORMING

*Kübra ÖZTÜRK GÜLER*
*Bahadır UYULGAN*



8th ICONST EST 2025 - Engineering Science and Technology

## CORROSION PERFORMANCE OF WC-CO DIE INSERTS BORIDED AT DIFFERENT TEMPERATURES FOR COLD FORMING

**Kübra Öztürk Güler*[1,2,3] and Bahadır Uyulgan[1,2]**

[1]**Address:** Department of Metallurgical and Materials Engineering, Dokuz Eylul University, İzmir, Turkey
[2]**Address:** [2]The Graduate School of Natural and Applied Sciences, Department of Metallurgical and Materials Engineering, Dokuz Eylul 35390 Izmir, Turkey
[3]**Address:** R&D Center, Norm İzmir Cıvata San. ve Tic. A.Ş., AOSB, İzmir, Turkey

***Corresponding author:** kubra.ozturk@normfasteners.com

### Abstract

WC-Co cemented carbides are composite materials produced by binding hard WC particles within a metallic Co matrix via liquid phase sintering. Due to their excellent wear resistance and toughness, they are widely utilized in cold forming dies; however, the cobalt matrix exhibits low corrosion resistance in aggressive environments. enhance surface properties, boriding treatments are employed, forming a hard and chemically stable boride layer that improves both wear and corrosion resistance. Process parameters such as boriding temperature and duration significantly affect the structural integrity of this layer, thus effecting corrosion performance. In this study, WC-Co material containing 19% Co was subjected to pack boriding at 900 °C, 950 °C, and 1000 °C for 4 hours to evaluate the effect of boriding temperature on corrosion behavior. Corrosion resistance was assessed using potentiodynamic polarization tests in a 1 M 3.5% NaCl solution, and corrosion rates (mm/year) were determined via Tafel extrapolation. XRD analysis confirmed the formation of CoB, $Co_2B$, and $W_2CoB_2$ phases in the borided layers. The results demonstrated that boriding temperature critically impacts corrosion resistance by altering the microstructure and stability of the boride layer. The sample borided at 1000 °C exhibited the best corrosion resistance, with the lowest corrosion rate of $9.09 \times 10^{-2}$ mm/year, while the untreated sample showed the highest rate at $3.783 \times 10^{-1}$ mm/year. This significant improvement suggests that boriding at elevated temperatures facilitates the formation of a more compact and chemically.

**Keywords:** WC-Co, Boriding, Corrosion, Tafel extrapolation, Cold Forming

# FINITE ELEMENT ANALYSIS OF STRESS PIN APPLICATION IN A LOBULAR COLD FORGING DIE

*Tolga AYDIN*
*Ertuğrul ORMAN*
*Burak HIZLI*



5th International Conference on Design, Research and Development

## FINITE ELEMENT ANALYSIS OF STRESS PIN APPLICATION IN A LOBULAR COLD FORGING DIE

**Tolga Aydın[1*], Ertuğrul Orman[2] and Burak Hızlı[3]**

[1]Norm Fasteners R&D Center, Orcid ID: 0000-0002-4979-1486, tolga.aydin@normfasteners.com
[2]Norm Fasteners R&D Center, Orcid ID: 0000-0002-2441-4211, ertugrul.orman@normfasteners.com
[3]Norm Fasteners R&D Center, Orcid ID: 0000-0002-9623-0075, burak.hizli@normfasteners.com

***Correspondence:** tolga.aydin@normfasteners.com; Tel.: +90 232 376 76 10

### Abstract

This study aims to investigate the applicability of the stress pin approach, which generates localized compressive pre-stress within the die to reduce the maximum principal stresses observed in asymmetric cold-forged forms–particularly in applications where the geometry is formed by upsetting.

High maximum principal stresses often occur in the die of asymmetric cold-forged parts, significantly limiting die life. Global shrink fitting is widely used to enhance the compressive pre-stress; however, the achievable shrink-fit level is restricted by the yield strength of the case material and is typically insufficient for lobular geometries. In this context, the present study examines the adaptation of stress pins, which generate localized compressive pre-stress in targeted regions of the die. A bolt with a lobular shaft form featuring more than two lobes was selected as the reference product, and the methodology was developed based on the principles introduced by Killmann and Merklein [1]. Unlike global shrink-fitting, the stress-pin approach targets only the regions with high stress concentration. These critical zones are first identified through finite element analysis, after which pins are press-fitted into pockets positioned near the identified areas. The interference fit of the pins induces localized compressive stresses, which counteract the tensile principal stresses generated during forming.

The pin diameter, interference level, distance from the forming zone, pin angle and pin quantity were optimized through iterative die analyses conducted in Simufact Forming. Each design variation was evaluated in terms of the induced compressive pre-stress, the maximum principal stresses generated during forming, and the stress distribution around the pin after insertion. The results show that proper optimization of stress pins can enhance local pre-stress levels and reduce the maximum principal stresses in the die, indicating a positive contribution to die life.

**Keywords:** Bolt, Stress pin, Cold forming, Die.

### References

1. Killmann, M. and Merklein, M., "Analysis of stress pins for the local prestressing of cold forging tools," Production Engineering Research and Development, vol. 15, pp. 119–131, 2021, doi: 10.1007/s11740-020-01012-4.

# IMPROVING COLD FORGING OF 304HC STAINLESS STEEL THROUGH INDUCTION PREHEATING: A COMPARATIVE INDUSTRIAL STUDY

*Muhammed Kaan KILINÇ*
*Hatice SANDALLI YILDIZ*
*Necip Fazıl ARSLAN*



5th International Conference on Design, Research and Development

## IMPROVING COLD FORGING OF 304HC STAINLESS STEEL THROUGH INDUCTION PREHEATING: A COMPARATIVE INDUSTRIAL STUDY

**Muhammed Kaan KILINÇ[1], Hatice SANDALLI YILDIZ[2], Necip Fazıl ARSLAN[3]**

**[1]Norm Fasteners, Orcid ID: https://orcid.org/0009-0001-8056-5153: kaan.kilinc@normfasteners.com**
**[2]Norm Fasteners, Orcid ID: https://orcid.org/0000-0002-5550-8480: hatice.sandalli@normfasteners.com**
**[3]Norm Fasteners, Orcid ID: https://orcid.org/0000-0002-5020-2474: necip.arslan@normfasteners.com**
*** Correspondence: kaan.kilinc@normfasteners.com; Tel.: + 90 232 376 76 10**

***Corresponding author:** kaan.kilinc@normfasteners.com; Tel.: + 90 232 376 76 10

### Abstract

This study evaluates the effectiveness of infrared (IR) and induction preheating in the cold forging of 304HC grade stainless steel hexagonal nuts (DIN 934, sizes M8 and M10). The primary objective is to investigate the effects of preheating method and applied temperature on material formability, tool life, and surface quality. Preheating is particularly critical in cold forming of austenitic stainless steels, which exhibit high strain-hardening behavior and limited formability at room temperature.

The experiments were conducted on multi-station cold forging presses using Ø11.75 mm and Ø16 mm 304HC stainless steel wire rods for M8 and M10 nuts, respectively, under real industrial conditions. All process parameters, including die performance, forging loads, and part hardness, were monitored throughout.

In the IR-based trials, the material was intended to be heated to 250–350 °C, but due to radiative losses and continuous feeding, actual temperatures reached only ~135–150 °C and dropped to approximately 60 °C by the final forging station. This insufficient heating resulted in minimal change: forging loads, surface defects, and hardness levels remained similar to those observed under non-heated conditions. Tool wear and punch breakage also occurred at comparable rates, indicating limited impact on die longevity. Moreover, the IR system showed low thermal efficiency at industrial production speeds, leading to substantial energy loss.

In contrast, induction heating was applied in a stepwise manner, with the material preheated to 250, 300, and 350 °C in successive trials. The increased temperature progressively reduced the material's flow stress and delayed the onset of strain-induced martensitic transformation, thus preserving the austenitic phase and enhancing ductility. Induction heating also ensured more uniform thermal distribution, smoother material flow, and a marked reduction in forging loads and surface cracking. The increase in hardness observed in forged parts was attributed to both plastic deformation and partial martensitic transformation. Nuts forged under induction preheating showed significantly lower hardening: core Vickers hardness dropped to ~140 HV and surface hardness to ~250 HV, whereas unheated samples showed ~390 HV (core) and ~430 HV (surface). Tool life was also notably improved, with single die sets producing approximately 66,000 nuts at 300 °C and 67,000 at 350 °C – a 25–30% increase in productivity relative to IR or no preheating. In addition, induction heating proved far more energy-efficient by directly delivering heat into the material with minimal losses.

Overall, the study demonstrates that under the tested conditions, induction preheating is a more energy-efficient and stable solution for cold forging of stainless steels, offering enhanced process reliability, improved part quality, and extended tool life under high-volume production conditions. Furthermore, a finite element simulation using Simufact is planned to analyze die stress distribution, billet temperature gradients, and forging load profiles for both heating methods. These results will support further optimization of the preheating process. Additionally, future work will include microstructural analysis of the forged components to evaluate grain deformation, martensite formation, and the heat-affected zone behavior across different preheating conditions.

**Keywords:** cold forging, induction preheating, infrared preheating, stainless steel (304HC)


www.normfasteners.com